

EXHIBIT 1



UNITED STATES PATENT AND TRADEMARK OFFICE

UNITED STATES DEPARTMENT OF COMMERCE
United States Patent and Trademark Office
Address: COMMISSIONER FOR PATENTS
P.O. Box 1450
Alexandria, Virginia 22313-1450
www.uspto.gov

APPLICATION NO.	FILING DATE	FIRST NAMED INVENTOR	ATTORNEY DOCKET NO.	CONFIRMATION NO.
10/849,571	05/20/2004	Wcidong Zhu	266923-000007USPT	6579
70001	7590	03/09/2010	EXAMINER	
NIXON PEABODY, LLP			NGHIEM, MICHAEL P	
300 S. Riverside Plaza			ART UNIT	PAPER NUMBER
16th Floor				2863
CHICAGO, IL 60606				
MAIL DATE		DELIVERY MODE		
03/09/2010		PAPER		

Please find below and/or attached an Office communication concerning this application or proceeding.

The time period for reply, if any, is set in the attached communication.

Office Action Summary	Application No. 10/849,571	Applicant(s) ZHU ET AL.
	Examiner MICHAEL P. NGHIEM	Art Unit 2863

-- The MAILING DATE of this communication appears on the cover sheet with the correspondence address --
Period for Reply

A SHORTENED STATUTORY PERIOD FOR REPLY IS SET TO EXPIRE 3 MONTH(S) OR THIRTY (30) DAYS, WHICHEVER IS LONGER, FROM THE MAILING DATE OF THIS COMMUNICATION.

- Extensions of time may be available under the provisions of 37 CFR 1.136(a). In no event, however, may a reply be timely filed after SIX (6) MONTHS from the mailing date of this communication.
- If no period for reply is specified above, the maximum statutory period will apply and will expire SIX (6) MONTHS from the mailing date of this communication.
- Failure to reply within the set or extended period for reply will, by statute, cause the application to become ABANDONED (35 U.S.C. § 133).
- Any reply received by the Office later than three months after the mailing date of this communication, even if timely filed, may reduce any earned patent term adjustment. See 37 CFR 1.704(b).

Status

- 1) Responsive to communication(s) filed on 10 December 2009, 24&25 September 2009.
 2a) This action is FINAL. 2b) This action is non-final.
 3) Since this application is in condition for allowance except for formal matters, prosecution as to the merits is closed in accordance with the practice under *Ex parte Quayle*, 1935 C.D. 11, 453 O.G. 213.

Disposition of Claims

- 4) Claim(s) 15,16,47-54 and 56-61 is/are pending in the application.
 4a) Of the above claim(s) ____ is/are withdrawn from consideration.
 5) Claim(s) ____ is/are allowed.
 6) Claim(s) 15,16,47-54,56-58,60 and 61 is/are rejected.
 7) Claim(s) 59 is/are objected to.
 8) Claim(s) ____ are subject to restriction and/or election requirement.

Application Papers

- 9) The specification is objected to by the Examiner.
 10) The drawing(s) filed on 20 May 2004 is/are: a) accepted or b) objected to by the Examiner.
 Applicant may not request that any objection to the drawing(s) be held in abeyance. See 37 CFR 1.85(a).
 Replacement drawing sheet(s) including the correction is required if the drawing(s) is objected to. See 37 CFR 1.121(d).
 11) The oath or declaration is objected to by the Examiner. Note the attached Office Action or form PTO-152.

Priority under 35 U.S.C. § 119

- 12) Acknowledgment is made of a claim for foreign priority under 35 U.S.C. § 119(a)-(d) or (f).
 a) All b) Some * c) None of:
 1. Certified copies of the priority documents have been received.
 2. Certified copies of the priority documents have been received in Application No. _____.
 3. Copies of the certified copies of the priority documents have been received in this National Stage application from the International Bureau (PCT Rule 17.2(a)).

* See the attached detailed Office action for a list of the certified copies not received.

Attachment(s)

- 1) Notice of References Cited (PTO-892)
 2) Notice of Allowance or Patent Drawing Review (PTO-548)
 3) Information Disclosure Statement(s) (PTO/SB/08)
 Paper No(s)/Mail Date _____
- 4) Interview Summary (PTO-413)
 Paper No(s)/Mail Date _____
- 5) Notice of Informal Patent Application
 6) Other: _____

DETAILED ACTION

The Amendments filed on December 10, 2009 and September 24&25, 2009 have been considered.

Petition

The petition filed on December 10, 2009 has been granted.

The petition filed on September 29, 2009 has been dismissed on November 23, 2009.

Continued Examination Under 37 CFR 1.114

A request for continued examination under 37 CFR 1.114, including the fee set forth in 37 CFR 1.17(e), was filed in this application after final rejection. Since this application is eligible for continued examination under 37 CFR 1.114, and the fee set forth in 37 CFR 1.17(e) has been timely paid, the finality of the previous Office action has been withdrawn pursuant to 37 CFR 1.114. Applicant's submission filed on September 24, 2009 has been entered.

Withdrawal of Allowability

The indicated allowability of claims 48, 50-54, 56-58, and 61 is withdrawn in view of the newly discovered reference(s) to Zhu et al. (US 2008/0294354) and Stubbs (US 5,327,358). Rejections based on the newly cited reference(s) follow.

Drawings

The drawings filed on May 20, 2004 are not acceptable because:

- 1/ Black shading is not acceptable, 37 CFR 1.84(m): See e.g. Figs. 10, 12, 16, 22.
- 2/ Character of lines, numbers, and letters are not uniformly thick and well-defined, 37 CFR 1.84(l): See e.g. Figs. 26's, 27's, and 28-30.

Claim Objections

Claim 56 is objected to because of the following informalities: after "comprising" (line 4), "," should be -- : --; "the force" (lines 8-9) lacks antecedent basis. Appropriate correction is required.

Claim Rejections - 35 USC § 112

The following is a quotation of the second paragraph of 35 U.S.C. 112:

The specification shall conclude with one or more claims particularly pointing out and distinctly claiming the subject matter which the applicant regards as his invention.

Art Unit: 2863

Claims 47, 49, and 60 are rejected under 35 U.S.C. 112, second paragraph, as being indefinite for failing to particularly point out and distinctly claim the subject matter which applicant regards as the invention.

Claims 47, 49, and 60, why is that when the “number of the stiffness parameters being larger than a number of system equations”, “the system equations are severely underdetermined”? The system equations being severely underdetermined is not understood.

The following is a quotation of the first paragraph of 35 U.S.C. 112:

The specification shall contain a written description of the invention, and of the manner and process of making and using it, in such full, clear, concise, and exact terms as to enable any person skilled in the art to which it pertains, or with which it is most nearly connected, to make and use the same and shall set forth the best mode contemplated by the inventor of carrying out his invention.

Claims 47, 49, and 60 are rejected under 35 U.S.C. 112, first paragraph, as failing to comply with the written description requirement. The claim(s) contains subject matter which was not described in the specification in such a way as to reasonably convey to one skilled in the relevant art that the inventor(s), at the time the application was filed, had possession of the claimed invention. The “number of stiffness parameters is larger than a number of system equations such that the system equations are severely underdetermined” is not described in the original disclosure.

Double Patenting

The nonstatutory double patenting rejection is based on a judicially created doctrine grounded in public policy (a policy reflected in the statute) so as to prevent the unjustified or improper timewise extension of the "right to exclude" granted by a patent and to prevent possible harassment by multiple assignees. A nonstatutory obviousness-type double patenting rejection is appropriate where the conflicting claims are not identical, but at least one examined application claim is not patentably distinct from the reference claim(s) because the examined application claim is either anticipated by, or would have been obvious over, the reference claim(s). See, e.g., *In re Berg*, 140 F.3d 1428, 46 USPQ2d 1226 (Fed. Cir. 1998); *In re Goodman*, 11 F.3d 1046, 29 USPQ2d 2010 (Fed. Cir. 1993); *In re Longi*, 759 F.2d 887, 225 USPQ 645 (Fed. Cir. 1985); *In re Van Ornum*, 686 F.2d 937, 214 USPQ 761 (CCPA 1982); *In re Vogel*, 422 F.2d 438, 164 USPQ 619 (CCPA 1970); and *In re Thorington*, 418 F.2d 528, 163 USPQ 644 (CCPA 1969).

A timely filed terminal disclaimer in compliance with 37 CFR 1.321(c) or 1.321(d) may be used to overcome an actual or provisional rejection based on a nonstatutory double patenting ground provided the conflicting application or patent either is shown to be commonly owned with this application, or claims an invention made as a result of activities undertaken within the scope of a joint research agreement.

Effective January 1, 1994, a registered attorney or agent of record may sign a terminal disclaimer. A terminal disclaimer signed by the assignee must fully comply with 37 CFR 3.73(b).

Claims 15, 16, 48, 50-54, 56-59, and 61 are provisionally rejected on the ground of nonstatutory obviousness-type double patenting as being unpatentable over claims 1, 3, 6, 17-20, and 36-40 of copending Application No. 12/153,348 (Zhu et al.). Although the conflicting claims are not identical, they are not patentably distinct from each other because Zhu et al. ('348) claims:

Regarding claims 15 and 51-54, a system for determining damage information of a structure (claim 17), comprising:

a sensor arranged to measure vibrations of a structure (claim 17, lines 3-4)

a stiffness parameter unit for receiving said vibration information, determining natural frequency data of said structure, and determining the stiffness parameters of said structure using said natural frequency data (claim 17, lines 5-8); and

a damage information processor for receiving said stiffness parameters and outputting damage information comprising spatial damage information on said structure, said spatial damage information comprising a damage location along said lengthwise dimension of said structure (claims 18, 19).

Regarding 16, said damage information processor outputs extent of damage information (claim 20).

Regarding claims 48, 50, and 61, a system for determining stiffness parameters of a structure (claim 1), comprising:

a sensor arranged to measure vibrations of said structure and output vibration information (claim 1, lines 3-4); and

a stiffness parameter unit for receiving said vibration information, determining natural frequency data of said structure, and determining the stiffness parameters of said structure using said natural frequency data (claim 1, lines 5-8);

wherein said stiffness parameter unit comprises an iterative processing unit (claim 3) that determines said stiffness parameters using a second or higher order perturbation process (claim 6).

Regarding claim 56, a system (claim 36), comprising:

a structure (claim 36, line 2);

a random impact device for introducing vibrations in said structure (claim 36, lines 3-5), said random impact device comprising,
a random signal generating unit for generating first and second outputs (claim 37, lines 3-4);

a random impact actuator for receiving said first and second outputs (claim 37, lines 5-6); and

an impact applicator coupled to said random impact actuator (claim 37, lines 7-8), wherein said random impact actuator drives said impact applicator such that the force and arrival times of said impact applicator at said structure are random (claim 37, lines 9-11);

a sensor arranged to measure vibrations of said structure and output vibration information (claim 36, lines 6-7); and

a stiffness parameter unit for receiving said vibration information, determining natural frequency data of said structure, and determining the stiffness parameters of said structure using said natural frequency data (claim 36, lines 8-11).

Regarding claim 57, said random impact actuator drives said impact applicator in accordance with said first and second outputs (claim 38).

Regarding claim 58, the first and second outputs comprise independent random variables (claim 39).

Regarding claim 59, the first and second outputs determine the force and arrival times, respectively, of the impact applicator at said structure (claim 40).

However, regarding claim 15, Zhu et al. ('354) does not claim the structure having a lengthwise dimension much greater in magnitude than cross-sectional dimensions. However, it is obvious to determine damage of structures having a lengthwise dimension much greater in magnitude than cross-sectional dimensions, since these structures are prone to vibrating along the lengthwise direction.

This is a provisional obviousness-type double patenting rejection because the conflicting claims have not in fact been patented.

Claim Rejections - 35 USC § 102

The following is a quotation of the appropriate paragraphs of 35 U.S.C. 102 that form the basis for the rejections under this section made in this Office action:

A person shall be entitled to a patent unless —

(b) the invention was patented or described in a printed publication in this or a foreign country or in public use or on sale in this country, more than one year prior to the date of application for patent in the United States.

Claims 15, 16, 48, 50-54, and 61 are rejected under 35 U.S.C. 102(b) as being anticipated by Stubbs (US 5,327,358).

Regarding claims 15, 51, 52, and 54, Stubbs discloses a system for determining damage information of a structure (Abstract, lines 1-2), comprising:

a sensor (claim 1, line 4) arranged to measure vibrations of a structure (claim 1, lines 4-5) having a lengthwise dimension much greater in magnitude than cross-sectional dimensions thereof (e.g. power poles, column 1, line 16) and to output vibration information (measured first signal, claim 1, lines 4-5);

a stiffness parameter unit for receiving said vibration information (column 1, lines 56-58; column 25, lines 31-34; 104, Fig. 5), determining natural frequency data of said structure (column 5, lines 8-9; column 7, lines 17-21; Table 14), and determining the stiffness parameters of said structure using said natural frequency data (using equation 1, column 5, which expresses the relationship between natural frequencies and stiffness parameter); and

a damage information processor (10) for receiving said stiffness parameters and outputting damage information comprising spatial damage information on said structure (column 2, line 51 – column 3, line 5), said spatial damage information comprising a damage location along said lengthwise dimension of said structure (column 2, lines 36-39).

Art Unit: 2863

Regarding claims 16, 53, and 54, Stubbs discloses said damage information processor outputs extent of damage information (column 2, lines 49-50).

Regarding claims 48, 50, and 61, Stubbs discloses a system for determining stiffness parameters of a structure (104, Fig. 5), comprising:

a sensor (claim 1, line 4) arranged to measure vibrations of said structure (claim 1, lines 4-5) and output vibration information (measured first signal, claim 1, lines 4-5); and

a stiffness parameter unit for receiving said vibration information (column 1, lines 56-58; column 25, lines 31-34; 104, Fig. 5), determining natural frequency data of said structure (column 5, lines 8-9; column 7, lines 17-21; Table 14), and determining the stiffness parameters of said structure using said natural frequency data (using equation 1, column 5, which expresses the relationship between natural frequencies and stiffness parameter);

wherein said stiffness parameter unit comprises an iterative processing unit (iterations, column 35, lines 16-22; column 34, lines 36-37) that determines said stiffness parameters using a second or higher order perturbation process (column 33, lines 36-54; repeating calculation of stiffness, column 34, lines 33-37).

Claim Rejections - 35 USC § 103

The following is a quotation of 35 U.S.C. 103(a) which forms the basis for all obviousness rejections set forth in this Office action:

(a) A patent may not be obtained though the invention is not identically disclosed or described as set forth in section 102 of this title, if the differences between the subject matter sought to be patented and the prior art are such that the subject matter as a whole would have been obvious at the time the invention was made to a person having ordinary skill in the art to which said subject matter pertains. Patentability shall not be negated by the manner in which the invention was made.

Claims 56-58 are rejected under 35 U.S.C. 103(a) as being unpatentable over Stubbs.

Regarding claim 56, Stubbs discloses a system (Fig. 5), comprising:

a structure (structure, Abstract, line 1; specimen 42);

a random impact device (impact hammer, column 5, line 51) for introducing vibrations in said structure (column 5, lines 50-53),

an impact applicator (impact hammer has steel tip, Google search, page 1, paragraph 2) such that the force (40) and arrival times of said impact applicator at said structure (42) are random (column 5, lines 50-53);

such that the force (40) and arrival times of said impact applicator at said structure (42) are random (column 5, lines 50-53);

a sensor (claim 1, line 4) arranged to measure vibrations of said structure (claim 1, lines 4-5) and output vibration information (measured first signal, claim 1, lines 4-5); and

a stiffness parameter unit for receiving said vibration information (column 1, lines 56-58; column 25, lines 31-34; 104, Fig. 5), determining natural frequency data of said structure (column 5, lines 8-9; column 7, lines 17-21; Table 14), and determining the stiffness parameters of said structure using said natural frequency data (using equation 1, column 5, which expresses the relationship between natural frequencies and stiffness parameter).

However, Stubbs does not disclose the following claimed features:

- Regarding claim 56, said random impact device comprising a random signal generating unit for generating first and second outputs; a random impact actuator for receiving said first and second outputs; and an impact applicator coupled to said random impact actuator, wherein said random impact actuator drives said impact applicator.
- Regarding claim 57, said random impact actuator drives said impact applicator in accordance with said first and second outputs.
- Regarding claim 58, the first and second outputs comprise independent random variables.

Nevertheless, Stubbs discloses that the random impact device is a PCB board (PCB 086B01, column 5, line 51). It would be obvious to electrically actuate the PCB impact device with electric signals since the device is an electrical device.

Therefore, it would have been obvious to a person having ordinary skill in the art at the time the invention was made to provide the impact device of Stubbs with electrically actuation means for the purpose of generating a force for inciting vibrations on a structure. Control of the impact device would be improved if the device is electrically actuated.

Allowable Subject Matter

Claim 59 is objected to as being dependent upon a rejected base claim, but would be allowable if rewritten in independent form including all of the limitations of the base claim and any intervening claims.

Reasons For Allowance

The following is an examiner's statement of reasons for allowance:

The **combination** as claimed wherein a system comprising the first and second outputs determine the force and arrival times, respectively, of the impact applicator at said structure (claim 59) is not disclosed, suggested, or made obvious by the prior art of record.

Any comments considered necessary by applicant must be submitted no later than the payment of the issue fee and, to avoid processing delays, should preferably accompany the issue fee. Such submissions should be clearly labeled "Comments on Statement of Reasons for Allowance."

Response to Arguments

Applicant's arguments filed on December 10 and September 24&25, 2009 have been fully considered but they are not persuasive.

With respect to the 35 USC 112, 2nd paragraph, rejections of claims 47, 49, and 60, Applicants argue that "for a linear system having m equations and n unknowns, the system is "underdetermined" if n > m (and is "overdetermined" if m > n). Severely underdetermined system of linear equations include systems wherein n >> m (i.e., far more unknowns than equations, where n represents unknowns and m represents equations)".

Examiner's position is that the claims recite "the number of stiffness parameter being larger than a number of system equations". It is unclear whether the stiffness parameters are "unknown" parameters since the stiffness parameters are already determined by the stiffness parameter unit (see e.g. claim 47, lines 8-10).

With respect to the 35 USC 112, 1st paragraph, rejection, Applicants argue that "Applicant's specification discloses, *inter alia*, damage detection using changes of natural frequencies '[f]or structures such as beams and lightning masts in electric substations, using only the changes in the natural frequencies can relatively accurately

Art Unit: 2863

detect the location(s) and extent of damage, even though the system equations are severely underdetermined in each iteration' (¶¶ [0181]-[0182])(emphasis added) and discusses an example of an aluminum beam test specimen (see FIG. 12) with "severely underdetermined system equations (5 equations with 80 unknowns)." (¶ [0188])(emphasis added)".

Examiner's position is that paragraphs [0181], [0182], and [0188] do not disclose comparing the system equations with the stiff parameter. Instead, paragraph [0188], e.g., describes comparing the system equations with the "m" unknowns (paragraph [0188], lines 22-24).

Applicants further argue that "[t]he claim amendments in question were introduced in the Supplemental Amendment filed on December 29, 2008, and did particularly point out where the originally filed disclosure supported the amendments. Accordingly, the Examiner has failed to discharge his burden and has further failed to set forth any factual findings supporting the conclusory allegation of lack of written description. See, e.g., *Purdue Pharma L.P. v. Faulding Inc.*, 230 F.3d 1320, 1323 (Fed. Cir. 2000)(the written description "inquiry is a factual one and must be assessed on a case-by-case basis")".

Examiner's position is that Examiner responded to the Supplemental Amendment on April 24, 2009 with factual findings supporting the conclusory allegation of lack of written

Art Unit: 2863

description: "Examiner's position is that paragraphs [0130] and [0188] describe comparing the system equations with the "m" unknowns (see paragraphs 0130, lines 20-25; paragraph 0188, lines 22-24). However, paragraphs [0130] and [0188] do not disclose comparing the system equations with the stiff parameter (e.g., $G_i^{**}(0)$, paragraph 0130, line 27)" (see Office Action, filed on April 24, 2009, page 10, paragraph 2).

Applicant's remaining arguments have been considered but are moot in view of the new ground(s) of rejection.

Contact Information

Any inquiry concerning this communication or earlier communications from the examiner should be directed to Michael Nghiem whose telephone number is (571) 272-2277. The examiner can normally be reached on M-F.

If attempts to reach the examiner by telephone are unsuccessful, the examiner's supervisor, Drew Dunn can be reached on (571) 272-2312. The fax phone number for the organization where this application or proceeding is assigned is (571) 273-8300.

Art Unit: 2863

Information regarding the status of an application may be obtained from the Patent Application Information Retrieval (PAIR) system. Status information for published applications may be obtained from either Private PAIR or Public PAIR. Status information for unpublished applications is available through Private PAIR only. For more information about the PAIR system, see <http://pair-direct.uspto.gov>. Should you have questions on access to the Private PAIR system, contact the Electronic Business Center (EBC) at 866-217-9197 (toll-free).

/Michael P. Nghiem/

Primary Examiner, GAU 2863

March 1, 2010

EXHIBIT 2



US 20050072234A1

(19) United States

(12) Patent Application Publication

Zhu et al.

(10) Pub. No.: US 2005/0072234 A1

(43) Pub. Date: Apr. 7, 2005

(54) SYSTEM AND METHOD FOR DETECTING STRUCTURAL DAMAGE

Publication Classification

(76) Inventors: Weidong Zhu, Elkridge, MD (US); Guangyao Xu, Baltimore, MD (US); Nengan Zheng, Baltimore, MD (US); Benjamin Haynes Emory, Baltimore, MD (US); Chun Nam Wong, Lubbock, TX (US)

(51) Int. Cl.⁷ G01H 1/14; G01M 7/08

(52) U.S. Cl. 73/579, 73/12.01; 702/56

(57) ABSTRACT

A system and method for detecting structural damage is provided that utilizes a general order perturbation methodology involving multiple perturbation parameters. The perturbation methodology is used iteratively in conjunction with an optimization method to identify the stiffness parameters of structures using natural frequencies and/or mode shape information. The stiffness parameters are then used to determine the location and extent of damage in a structure. A novel stochastic model is developed to model the random impact series produced manually or to generate a random impact series in a random impact device. The random impact series method or the random impact device can be used to excite a structure and generate vibration information used to obtain the stiffness parameters of the structure. The method or the device can also just be used for modal testing purposes. The random impact device is a high energy, random, and high signal-to-noise ratio system.

Correspondence Address:
FLESCHNER & KIM, LLP
P.O. Box 221200
Chantilly, VA 20153-1200 (US)

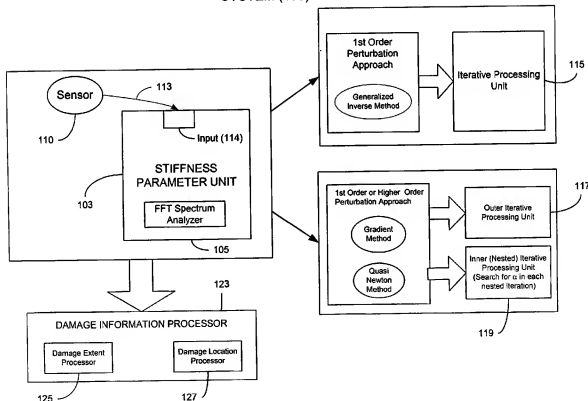
(21) Appl. No.: 10/849,571

(22) Filed: May 20, 2004

Related U.S. Application Data

(60) Provisional application No. 60/471,873, filed on May 20, 2003. Provisional application No. 60/512,656, filed on Oct. 20, 2003.

SYSTEM (100)



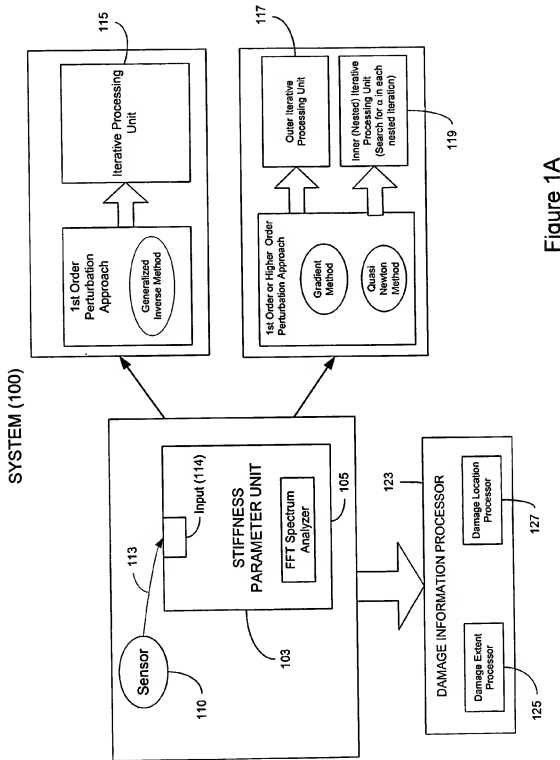


Figure 1A

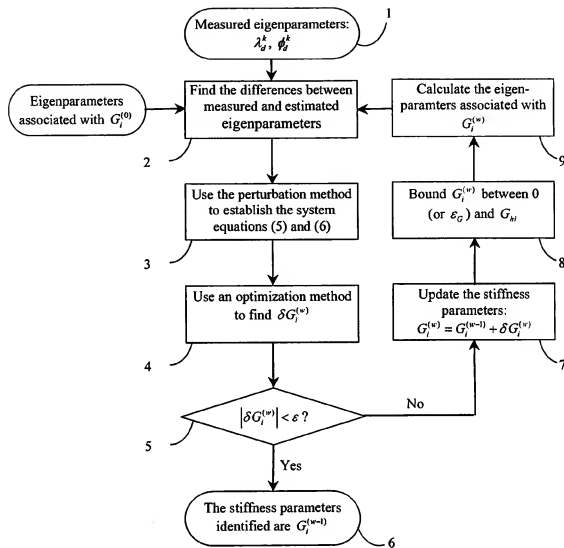


Figure 1B

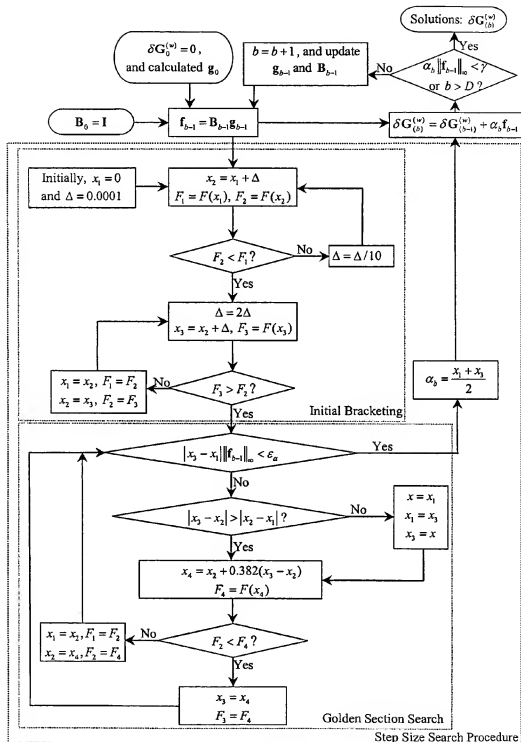


Figure 2

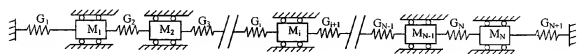


Figure 3

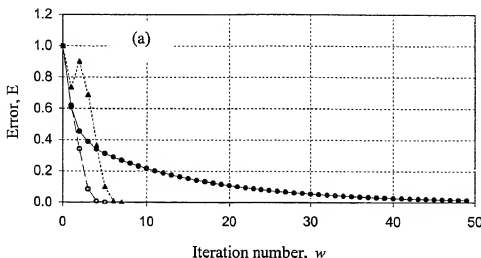


Fig. 4A

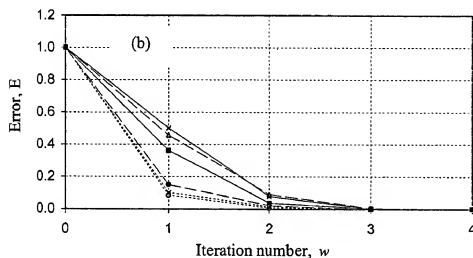


Fig. 4B

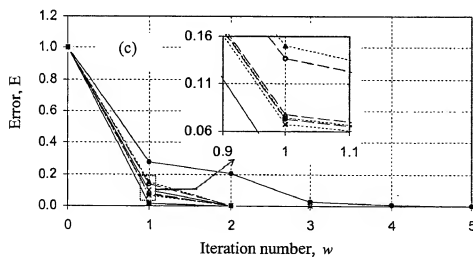
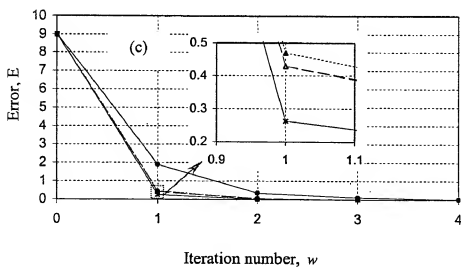
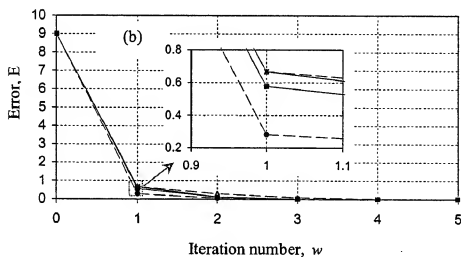
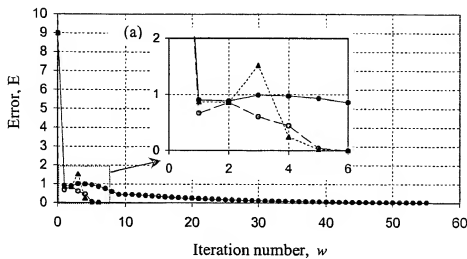


Fig. 4C



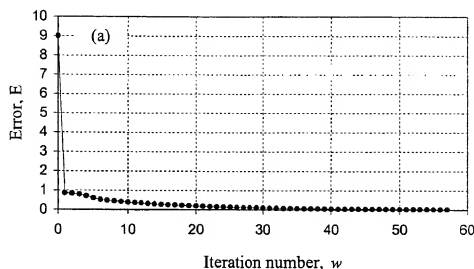


Fig. 6A

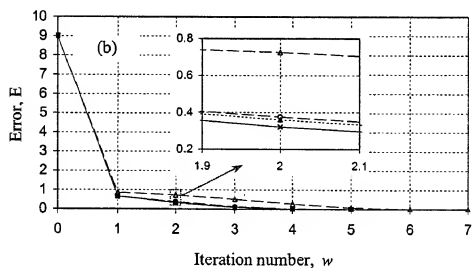


Fig. 6B

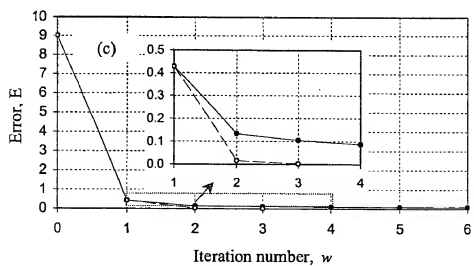


Fig. 6C

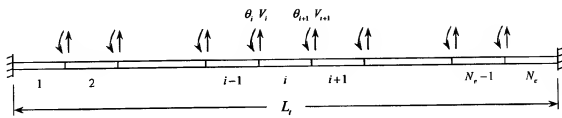


Figure 7

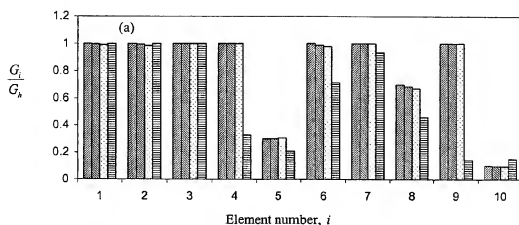


Fig. 8A

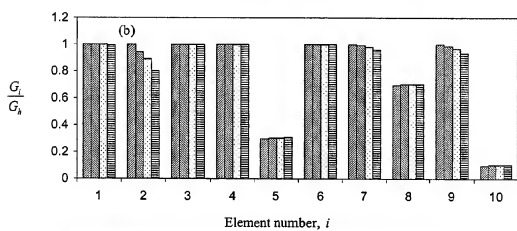


Fig. 8B

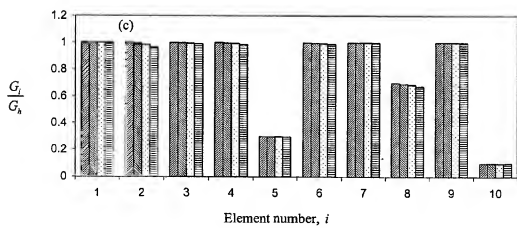
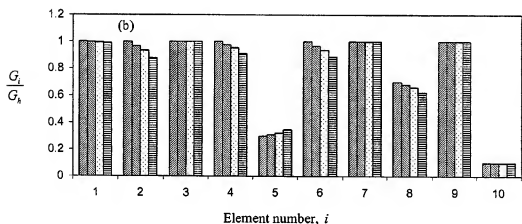
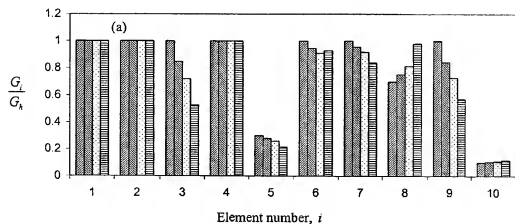


Fig. 8C



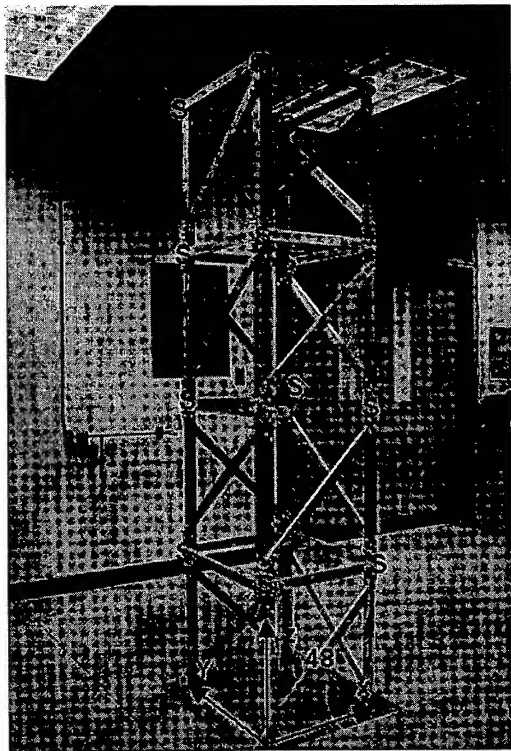


Figure 10

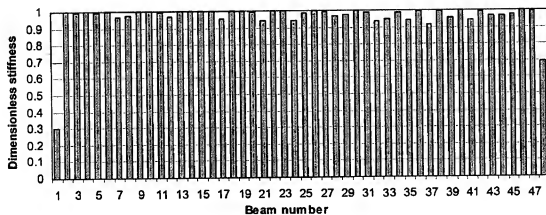


Figure 11

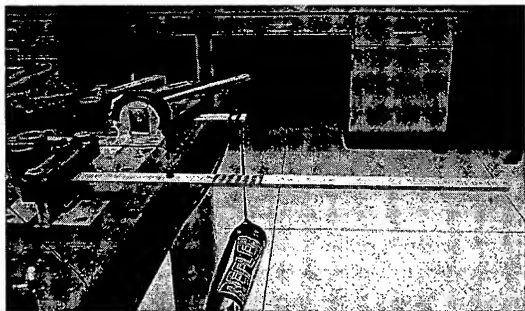


Figure 12

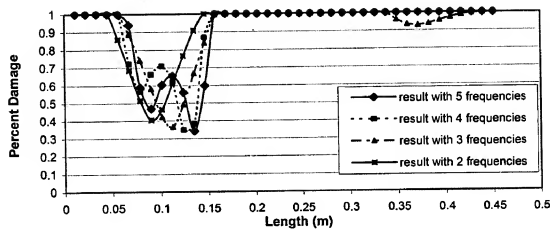


Figure 13

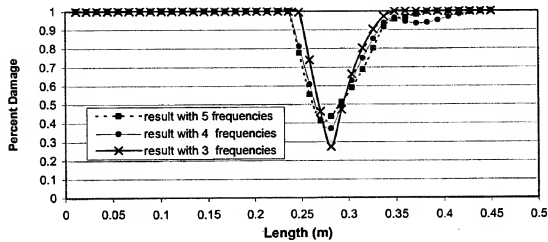


Figure 14

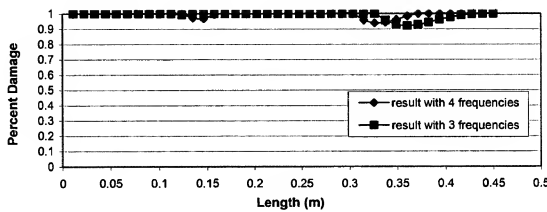


Figure 15

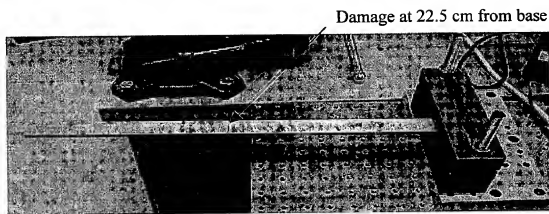


Figure 16

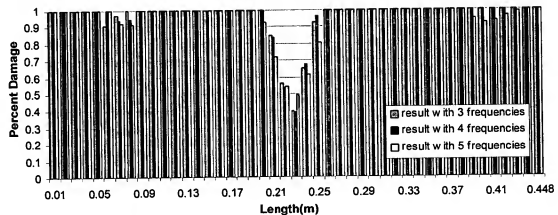


Figure 17

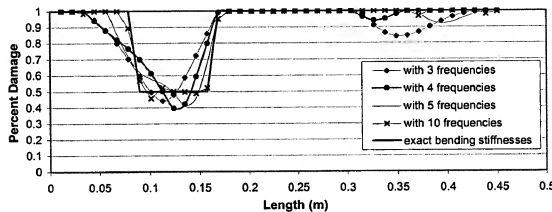


Figure 18

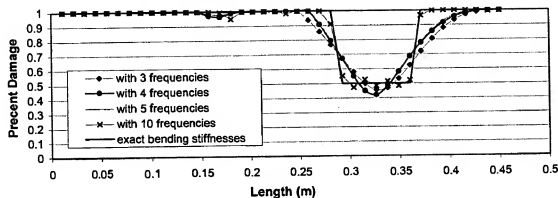


Figure 19

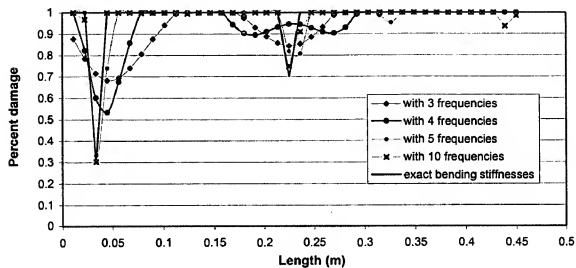


Figure 20

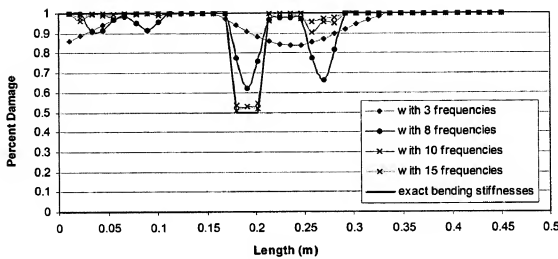


Figure 21

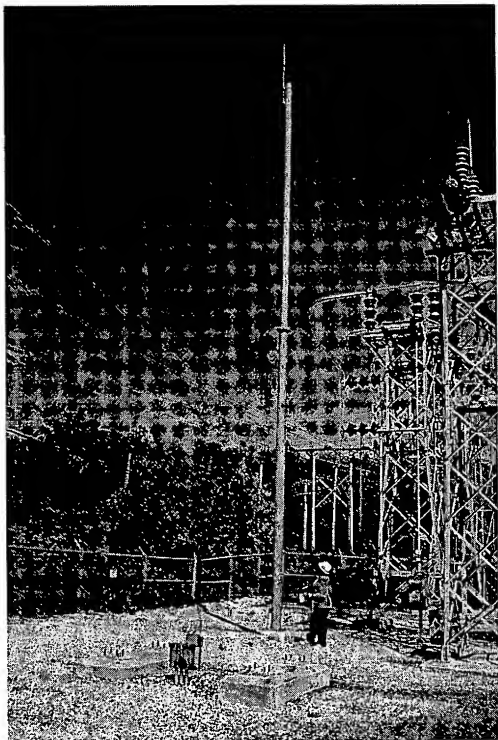


Figure 22

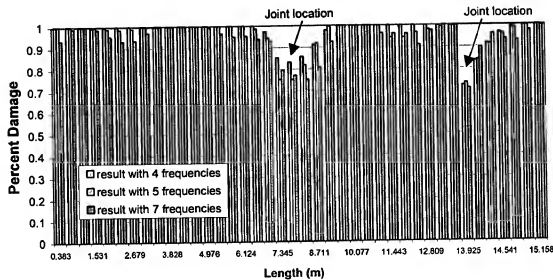


Figure 23

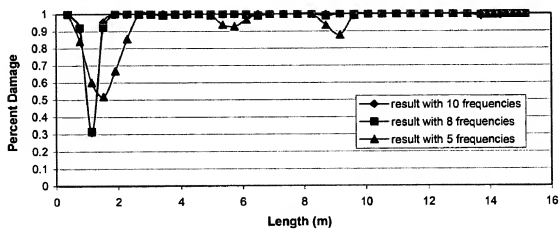


Figure 24

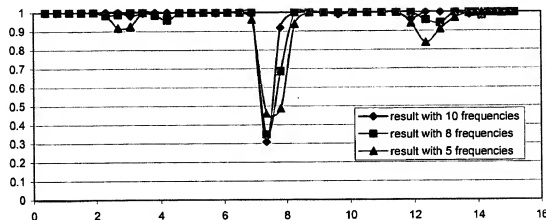


Figure 25

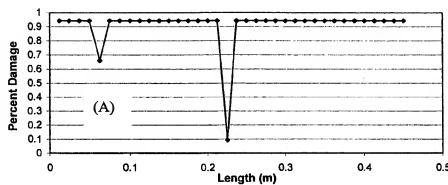


Fig. 26A

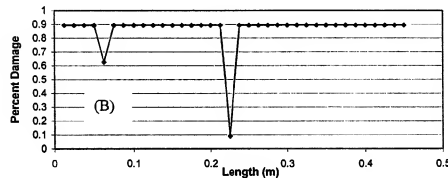


Fig. 26B

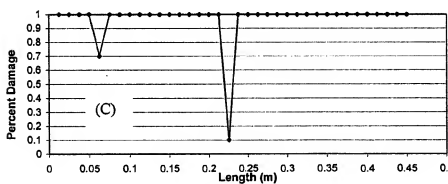


Fig. 26C

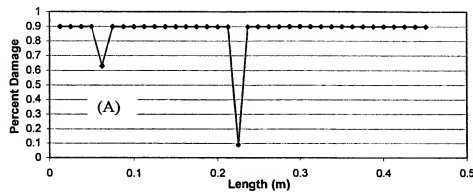


Fig. 27A

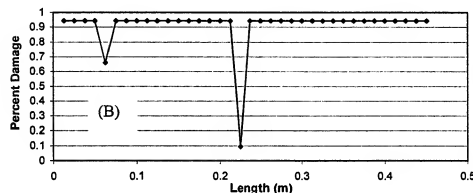


Fig. 27B

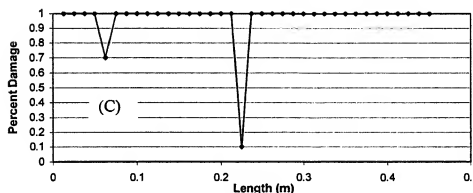


Fig. 27C

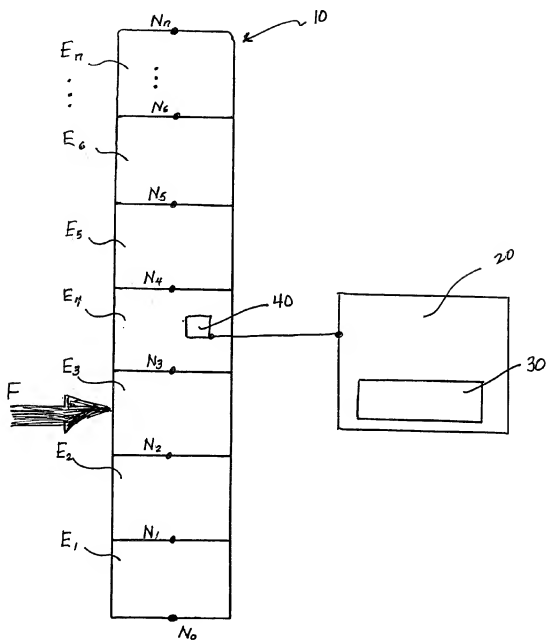


Figure 28

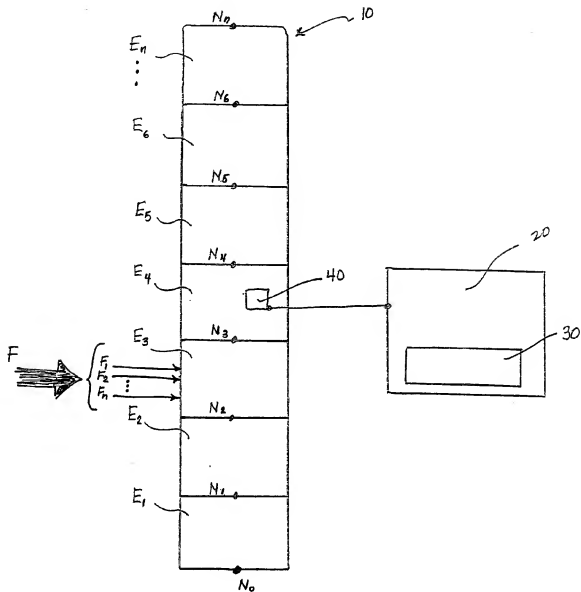


Figure 29

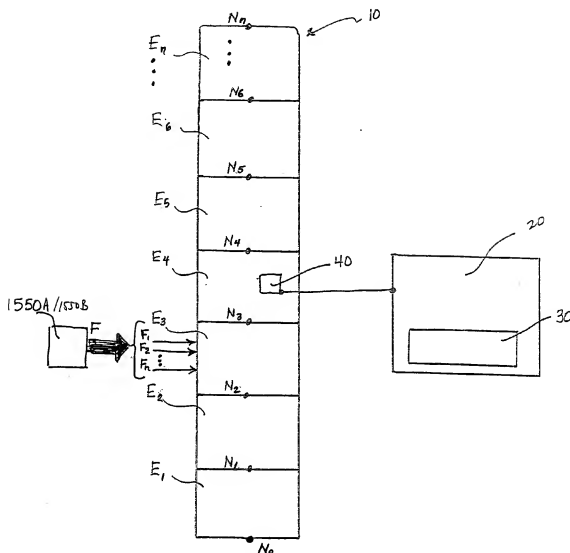


Figure 30

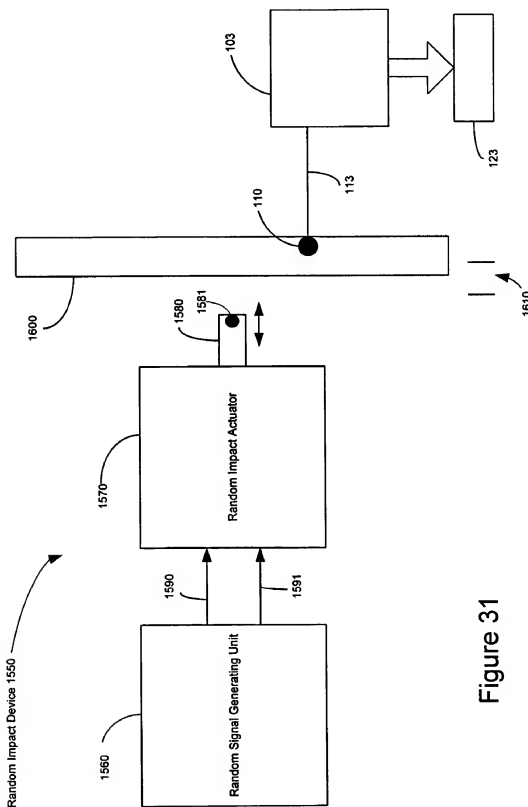


Figure 31

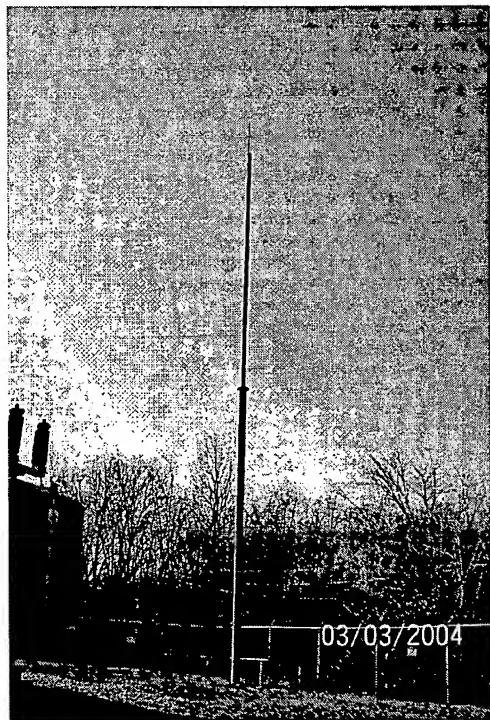


Figure 32

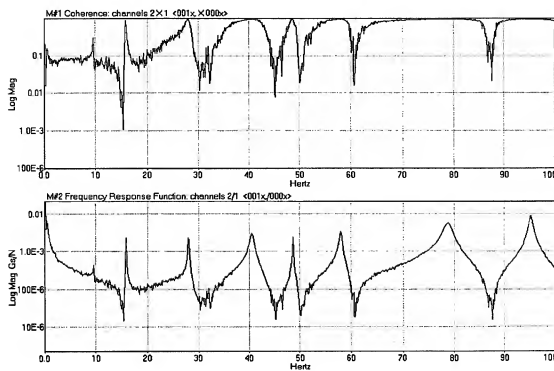


Figure 33A

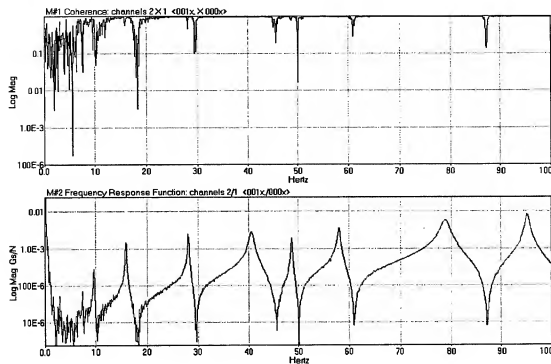


Figure 33B

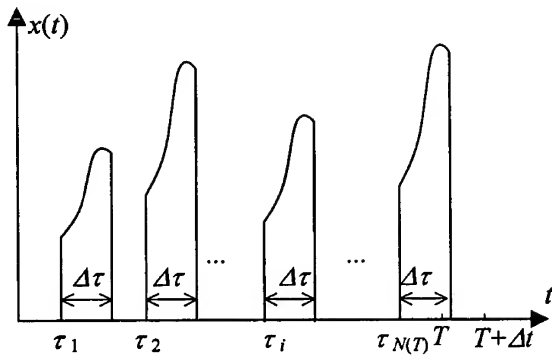


Figure 34

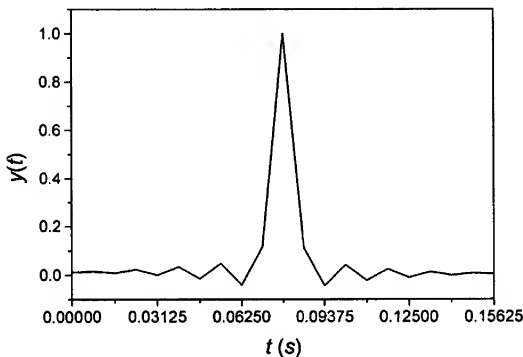


Figure 35

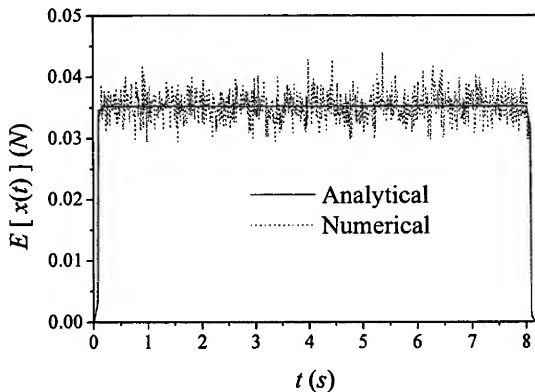


Figure 36

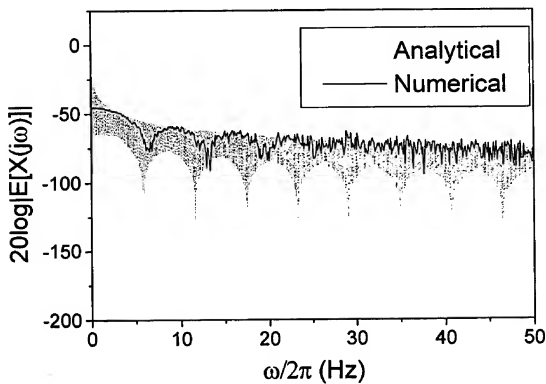


Figure 37

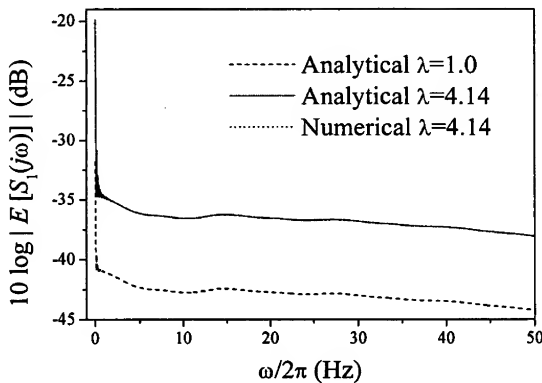


Figure 38

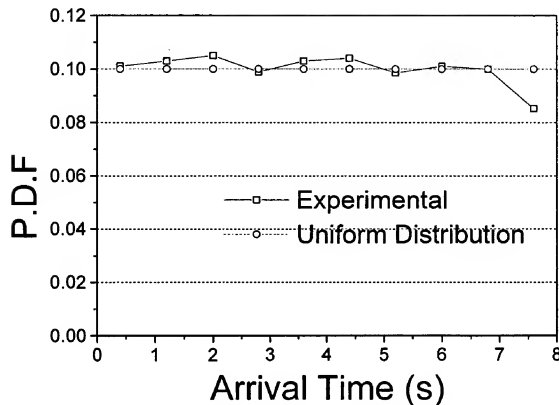


Figure 39

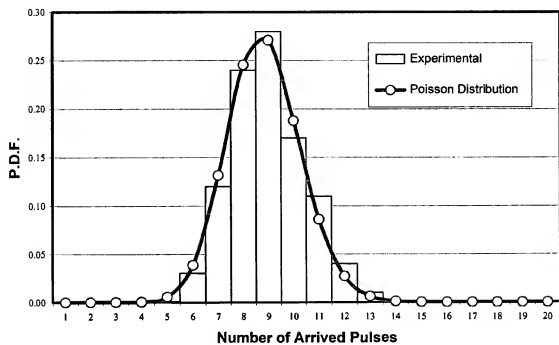


Figure 40

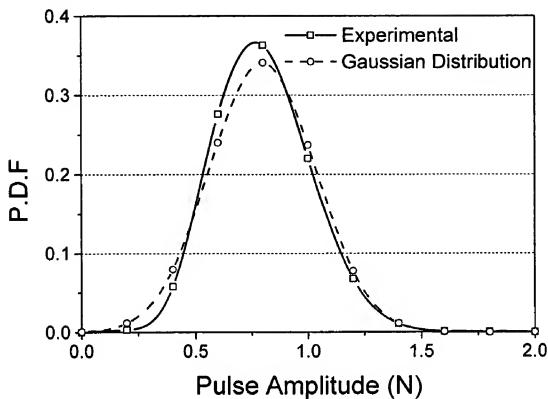


Figure 41

SYSTEM AND METHOD FOR DETECTING STRUCTURAL DAMAGE

[0001] This application claims priority to U.S. Provisional Patent Application Ser. No. 60/471,873 filed May 20, 2003 and U.S. Provisional Patent Application Ser. No. 60/512,656 filed Oct. 10, 2003, which are both incorporated herein by reference.

BACKGROUND OF THE INVENTION

[0002] 1. Field of the Invention

[0003] The invention relates to a method and apparatus for detecting structural damage, and, more specifically, to a method and apparatus for detecting structural damage using changes in natural frequencies and/or mode shapes.

[0004] 2. Background of the Related Art

[0005] Damage in a structure can be defined as a reduction in the structure's load bearing capability, which may result from a deterioration of the structure's components and connections. All load bearing structures continuously accumulate structural damage, and early detection, assessment and monitoring of this structural damage and appropriate removal from service is the key to avoiding catastrophic failures, which may otherwise result in extensive property damage and cost.

[0006] A number of conventional non-destructive test (NDT) methods are used to inspect load bearing structures. Visual inspection of structural members is often unquantifiable and unreliable, especially in instances where access to damaged areas may be impeded or damage may be concealed by paint, rust, or other coverings. Penetrant testing (PT) requires that an entire surface of the structure be covered with a dye solution, and then inspected. PT reveals only surface cracks and imperfections, and can require a large amount of potentially hazardous dye be applied and disposed of. Similarly, magnetic particle testing (MT) requires that an entire surface of the structure be treated, can be applied only to ferrous materials, and detects only relatively shallow cracks. Further, due to the current required to generate a strong enough magnetic field to detect cracks, MT is not practically applied to large structures. Likewise, eddy current testing (ET) uses changes in the flow of eddy currents to detect flaws, and only works on materials that are electrically conductive. Ultrasonic testing (UT) uses transmission of high frequency sound waves into a material to detect imperfections. Results generated by all of these methods can be skewed due to surface conditions, and cannot easily isolate damage at joints and boundaries of the structure. Unless a general vicinity of a damage location is known prior to inspection, none of these methods are easily or practically applied to large structures which are already in place and operating. On the other hand, resonant inspection methods are not capable of determining the extent or location of damage, and is used only on a component rather than a assembled structure. None of the above NDT methods are easily or practically applied to large structures requiring a high degree of structural integrity.

[0007] Because of these shortfalls in existing NDT methods when inspecting relatively large structures, structural damage detection using changes in vibration characteristics has received much attention in recent years. Vibration based health monitoring for rotating machinery is a relatively

mature technology, using a non-model based approach to provide a qualitative comparison of current data to historical data. However, this type of vibration based damage testing does not work for most structures. Rather, vibration based damage detection for structures is model based, comparing test data to analytical data from finite element models to detect the location(s) and extent of damage. Vibration based damage detection methods fall into three basic categories. The first of these is direct methods such as optimal matrix updating algorithms, which identify damage location and extent in a single iteration. Because of the single iteration, these methods are not accurate in detecting a large level of damage. The second category is iterative methods. The methodology has only been for updating modeling, which determines modified structural parameters iteratively by minimizing differences between model and test data. The third category includes control-based eigenstructure assignment methods, which have the similar limitation to that of the direct methods indicated above and are not accurate in detecting a large level of damage. None of these current vibration based methods have been incorporated into an iterative algorithm that can detect small to large levels of damage, and the vibration based approach for structures remains an immature technology area which is not readily available on a commercial basis.

SUMMARY OF THE INVENTION

[0008] An object of the invention is to solve at least the above problems and/or disadvantages and to provide at least the advantages described hereinafter.

[0009] Another object of the invention is to provide a system and method for detecting structural damage based on changes in natural frequencies and/or mode shapes.

[0010] An advantage of the system and method as embodied and broadly described herein is that it can be applied to a large operating structure with a large number (thousands or more) of degrees of freedom.

[0011] Another advantage of the system and method as embodied and broadly described herein is that it can accurately detect the location(s) and extent of small to large levels of damage and is especially useful for detecting a large level of damage with severe mismatch between the eigenparameters of the damaged and undamaged structures.

[0012] Another advantage of the system and method as embodied and broadly described herein is that it can work with a limited number of measured vibration modes.

[0013] Another advantage of the system and method as embodied and broadly described herein is that it can use measurement at only a small number of locations compared to the degrees of freedom of the system. A modified eigenvector expansion method is used to deal with the incomplete eigenvector measurement problem arising from experimental measurement of a lesser number of degrees of freedom than that of the appropriate analytical model.

[0014] Another advantage of the system and method as embodied and broadly described herein is that it can be applied to structures with slight nonlinearities such as opening and closing cracks. The random shaker test or the random impact series method can be used to average out slight nonlinearities and extract linearized natural frequencies and/or mode shapes of a structure.

[0015] Another advantage of the system and method as embodied and broadly described herein is that it can handle structures with closely spaced vibration modes, where mode switching can occur in the damage detection process.

[0016] Another advantage of the system and method as embodied and broadly described herein is that it can handle different levels of measurement noise with estimation errors within the noise levels.

[0017] Another advantage of the system and method as embodied and broadly described herein is that the damage detection method and the vibration testing methods such as the random impact series method enables damage detection and assessment to be automated, thus improving the reliability/integrity of results.

[0018] Another advantage of the system and method as embodied and broadly described herein is that damage detection and assessment may be automated in the field so that structural health can be monitored at central location and useful service life may be optimized.

[0019] Another advantage of the system and method as embodied and broadly described herein is that the random impact series method enables the modal parameters such as natural frequencies and/or mode shapes to be measured for a large structure or a structure in the field when there are noise effects such as those arising from the wind or other ambient excitation.

[0020] Additional advantages, objects, and features of the invention will be set forth in part in the description which follows and in part will become apparent to those having ordinary skill in the art upon examination of the following or may be learned from practice of the invention. The objects and advantages of the invention may be realized and attained as particularly pointed out in the appended claims.

BRIEF DESCRIPTION OF THE DRAWINGS

[0021] The invention will be described in detail with reference to the following drawings in which like reference numerals refer to like elements wherein:

[0022] FIG. 1A shows a system 100 for detection of structural damage according to one embodiment of the invention;

[0023] FIG. 1B is a flowchart of an inverse algorithm for identifying stiffness parameters of a damaged structure from a select set of measured eigenparameters, in accordance with an embodiment of the invention;

[0024] FIG. 2 is a flowchart of a quasi-Newton method for finding an optimal solution to the system equations shown in the flowchart of FIG. 1B, in accordance with an embodiment of the invention;

[0025] FIG. 3 is a schematic view of a serial mass-spring system;

[0026] FIGS. 4A-4C illustrate estimation errors in a series of iterations for a low order system with a small level of damage;

[0027] FIGS. 5A-5C illustrate estimation errors in a series of iterations for a low order system with a large level of damage;

[0028] FIGS. 6A-6C illustrate estimation errors in a series of iterations for a large order system with a large level of damage;

[0029] FIG. 7 illustrates a finite element model of a fixed-fixed beam;

[0030] FIGS. 8A-8C illustrate the estimated stiffness parameters with complete eigenvector measurements and different noise levels for a ten element beam with a large level of damage;

[0031] FIGS. 9A-9B illustrate stiffness parameters with reduced eigenvector measurements and different noise levels for a ten element beam with a large level of damage;

[0032] FIG. 10 illustrates a modular, four bay space frame;

[0033] FIG. 11 illustrates the estimated dimensionless stiffnesses for the damaged frame as shown in FIG. 11;

[0034] FIG. 12 illustrates a cantilever aluminum beam test specimen with uniform damage in approximately 5 elements;

[0035] FIG. 13 illustrates the experimental results for the estimated bending stiffnesses of all the elements of a cantilever aluminum beam test specimen with the actual damage between 10 cm and 15 cm from the cantilevered end using a 40-element finite element model;

[0036] FIG. 14 illustrates the experimental results for the estimated bending stiffnesses of all the elements of a cantilevered aluminum beam test specimen with the actual damage between 25 cm and 30 cm from the cantilevered end using a 40-element finite element model;

[0037] FIG. 15 illustrates the experimental results for the estimated bending stiffnesses of all the elements of an undamaged cantilever aluminum beam test specimen using a 40-element finite element model;

[0038] FIG. 16 illustrates a cantilever aluminum beam test specimen with a narrow cut;

[0039] FIG. 17 illustrates the experimental results for the estimated bending stiffnesses of all the elements of the test specimen as shown in FIG. 16 using a 45-element finite element model;

[0040] FIG. 18 illustrates the estimated bending stiffnesses of all the elements of the cantilever aluminum with simulated damage between 9 cm and 15.75 cm from the cantilevered end using a 40-element finite element model;

[0041] FIG. 19 illustrates the estimated bending stiffnesses of all the elements of the cantilever aluminum beam with simulated damage between 29.25 cm and 36 cm from the cantilevered end using a 40-element finite element model;

[0042] FIG. 20 illustrates the estimated bending stiffnesses of all the elements of the cantilever aluminum beam with multiple simulated damage—one at the 3rd element and the other at the 20th element;

[0043] FIG. 21 illustrates the estimated bending stiffnesses of all the elements of the cantilever aluminum beam with simulated uniform damage from the 16th to the 18th element;

[0044] FIG. 22 illustrates a 50-foot lightning mast test specimen with an eccentric spike at the top;

[0045] FIG. 23 illustrates the experimental results for the estimated bending stiffnesses of all the elements of the lightning mast as shown in FIG. 22 with simulated damage between 0.76 m and 1.125 m from the ground using a 40-element finite element model;

[0046] FIG. 24 illustrates the estimated bending stiffnesses of all the elements of the lightning mast as shown in FIG. 22 with simulated damage between 0.76 m and 1.125 m from the ground using a 40-element finite element model;

[0047] FIG. 25 illustrates the estimated bending stiffnesses of all the elements of the lightning mast as shown in FIG. 42 with simulated damage between 6.89 m and 7.35 m from the ground using a 40-element finite element model;

[0048] FIGS. 26A-26C illustrate the estimated bending stiffnesses of all the elements of a cantilever aluminum beam using the first regularization method;

[0049] FIGS. 27A-27C illustrate the estimated bending stiffnesses of all the elements of a cantilever aluminum beam using the second regularization method;

[0050] FIG. 28 illustrates an example of a practical application of the damage detection method of FIG. 1A, in accordance with an embodiment of the invention;

[0051] FIG. 29 illustrates the application of a series of random impacts to the practical application of the damage detection method of FIG. 1A, in accordance with an embodiment of the invention;

[0052] FIG. 30 illustrates a system for applying the series of random impacts shown in FIG. 29 to the practical application of the damage detection method of FIG. 1A, in accordance with an embodiment of the invention;

[0053] FIG. 31 is a block diagram of one preferred embodiment of the random impact device of FIG. 30;

[0054] FIG. 32 illustrates a lightning mast specimen;

[0055] FIGS. 33A-33B are graphical representations of coherence and FRF from single and multiple impact tests of the mast shown in FIG. 32;

[0056] FIG. 34 illustrates a random series of pulses with the same deterministic shape and random amplitudes and arrival times;

[0057] FIG. 35 illustrates an average normalized shape function of force pulses;

[0058] FIGS. 36-38 are graphical representations of analytical and numerical solutions;

[0059] FIG. 39 shows the comparison of the probability density function (PDF) of the experimental arrival time with that from uniform distribution;

[0060] FIG. 40 shows the comparison of the experimental and analytical PDFs for the number of arrived pulses; and

[0061] FIG. 41 shows the comparison of the experimental and analytical PDFs for the pulse amplitudes.

DETAILED DESCRIPTION OF PREFERRED EMBODIMENTS

[0062] Commonly measured modal parameters, such as natural frequencies and mode shapes, are functions of physi-

cal properties of a particular structure. Therefore, changes in these physical properties, such as reductions in stiffness resulting from the onset of cracks or a loosening of a connection, will cause detectable changes in these modal parameters. Thus, if the changes in these parameters are indicators of damage, vibration based damage detection may be, simplistically, reduced to a system identification problem. However, a number of factors have made vibration based damage detection difficult to implement in practice in the past.

[0063] The system and method for detecting structural damage as embodied and broadly described herein is motivated by the observed advantages of vibration based damage detection over currently available technologies. It will be understood that this system and method may be effectively applied to damage detection and assessment for substantially all types and configurations of structures, including, but not limited to, simple beams, hollow tubes, trusses, frames, and the like. However, simply for ease of discussion, the system and method will first be discussed with respect to three examples—a mass-spring model, a beam, and a space frame—for conceptualization purposes. The system and method will later be applied lightning masts in electric substations.

[0064] FIG. 1A shows a system 100 for detecting structural damage according to one embodiment of the invention. System 100 includes a stiffness parameter unit 103 for detecting stiffness of a structure in question. Stiffness parameter unit 103 may include a spectrum analyzer or any other device capable of receiving vibration information and providing natural frequency and/or mode shape data. One example might be a spectrum analyzer capable of performing a fast fourier transform (FFT) and with modal analysis software for deriving mode shape data from vibration information received from sensor 110 if mode shape information is needed. A roving sensor technique or multiple sensors may need to be used if mode shape information needs to be used. If mode shape information is desired, a sensor should be provided at the tip of the hammer or device used to excite the structure. This sensor should be configured to send data to the spectrum analyzer in order to obtain the frequency response function, which the spectrum analyzer (modal analysis software) uses to obtain mode shape information. Stiffness parameter unit 103 is configured to receive vibration information output from the sensor 110 via sensor coupler 113 and input 114. Sensor coupler 113 could be a wire, optical fiber or even a wireless connection between sensor 110 and stiffness parameter unit 103.

[0065] Stiffness parameter unit 103 may include an iterative processing unit 115 capable of determining stiffness parameters using a first order perturbation approach and the generalized inverse method. The first order perturbation approach can include using natural frequencies and/or mode shapes of the structure according to a preferred embodiment of the invention. Iterative processing unit 115 may be capable of converging to a correct result for the output of stiffness parameters even when the system is underdetermined. Stiffness parameter unit 103 may further include an outer iterative processing unit 117 and an inner (nested) iterative processing unit 119 which may operate using a first or higher order perturbation approach and a gradient or quasi-Newton method to be discussed below. Stiffness parameter unit 103 outputs stiffness parameters to damage

information processor 123. Damage information processor includes a damage extent processor 125 and a damage location processor 127. Damage location processor 127 outputs the location(s) of damage and damage extent processor 125 outputs the extent of damage.

[0066] System 100 using the iterative processing units 115 or 117 and 119 is capable of determining the stiffness parameters and ultimately the location(s) and extent of damage for structures with a largest dimension less than 50 meters, 25 meters, 10 meters, 2.5 meters and even 1.5 meters. Examples of this are provided herein.

[0067] The system and method may include a multiple-parameter, general order perturbation method, in which the changes in the stiffness parameters are used as the perturbation parameters. By equating the coefficients of like-order terms involving the same perturbation parameters in the normalization relations of eigenvectors and the eigenvalue problem, the perturbation problem solutions of all orders may be derived, and the sensitivities of all eigenparameters may be obtained. The perturbation method may be used in an iterative manner with an optimization method to identify the stiffness parameters of structures.

[0068] Methodology

[0069] This method presented below can simultaneously identify all the unknown stiffness parameters and is formulated as a damage detection problem. Since the effects of the changes in the inertial properties of a damaged structure are usually relatively small, only the changes in the stiffness properties due to structural damage are considered.

[0070] Consider a N degree-of-freedom, linear, time-invariant, self-adjoint system with distinct eigenvalues. The stiffness parameters of the undamaged structure are denoted by G_i ($i=1, 2, \dots, m$), where m is the number of the stiffness parameters. Structural damage is characterized by reductions in the stiffness parameters. The estimated stiffness parameters of the damaged structure before each iteration are denoted by G_i ($i=1, 2, \dots, m$), and its stiffness matrix, which depends linearly on G_i , is denoted by $K=G_i$, where $G=[G_1, G_2, \dots, G_m]^T$. Here the superscript T denotes matrix transpose. The eigenvalue problem of the structure with stiffness parameters G_i is

$$K\phi^k = \lambda^k M\phi^k \quad (1)$$

[0071] where M is the constant mass matrix, and $\lambda^k = \lambda^k(G)$ and $\phi^k = \phi^k(G)$ ($k=1, 2, \dots, N$) are the k -th eigenvalue and mass-normalized eigenvector respectively. It is noted that $\lambda_k = \omega_k^2$, where ω_k is the k -th natural frequency of the structure. The normalized eigenvectors of (1) satisfy the orthonormality relations

$$(\phi^i)^T M \phi^j = \delta_{ij} \quad (2)$$

[0072] where $1 \leq i, j \leq N$ and δ_{ij} is the Kronecker delta. Before the first iteration, the initial stiffness parameters of the damaged structure are assumed to be $G^{(0)} = \phi_{1,0}^{-1} \phi_1$ ($i=1, 2, \dots, m$), where $0 < \phi_{1,0} \leq 1$, and the eigenvalue problem in (1) corresponds to that of the structure with stiffness parameters $G^{(0)}$. If there is no prior knowledge of the integrity of the structure, one can start the iteration from the stiffness parameters of the undamaged structure and set $\phi_{1,0}=1$. Let G_{di} ($i=1, 2, \dots, m$) denote the stiffness parameters of the

damaged structure. The eigenvalue problem of the damaged structure is

$$K_d \phi_d^k = \lambda_d^k M \phi_d^k \quad (3)$$

[0073] where $K_d = K(G_d)$ is the stiffness matrix with $G_d = [G_{d1}, G_{d2}, \dots, G_{dm}]^T$, and $\lambda_d^k = \lambda^k(G_d)$ and $\phi_d^k = \phi^k(G_d)$ are the k -th eigenvalue and mass-normalized eigenvector respectively. The stiffness matrix K_d is related to K through the Taylor expansion

$$K_d = K(G_d) = K + \sum_{i=1}^m \frac{\partial K}{\partial G_i} \delta G_i \quad (4)$$

[0074] where $\delta G_i = G_{di} - G_i$ ($i=1, 2, \dots, m$) are the changes in the stiffness parameters, and the higher-order derivatives of K with respect to G_i vanish because K is assumed to be a linear function of G_i . Based on the finite element model, the global stiffness matrix of a distributed structure satisfies (4) as its higher-order derivatives with respect to each element stiffness parameter vanish.

[0075] Let the k -th eigenvalue and mass-normalized eigenvector of the damaged structure be related to λ^k and ϕ^k through

$$\begin{aligned} \lambda_d^k &= \lambda^k + \sum_{i=1}^m \lambda_{1,ik}^k \delta G_i + \sum_{i=1}^m \sum_{j=1}^m \lambda_{1,2jk}^k \delta G_i \delta G_j + \\ &\quad \cdots + \sum_{i=1}^m \sum_{j=1}^m \cdots \sum_{r=1}^m \lambda_{1,pjk...r}^k \delta G_i \delta G_j \cdots \delta G_r + \epsilon_{\lambda}^k, \end{aligned} \quad (5)$$

$$\begin{aligned} \phi_d^k &= \phi^k + \sum_{i=1}^m \phi_{1,ik}^k \delta G_i + \sum_{i=1}^m \sum_{j=1}^m \phi_{1,2jk}^k \delta G_i \delta G_j + \\ &\quad \cdots + \sum_{i=1}^m \sum_{j=1}^m \cdots \sum_{r=1}^m \phi_{1,pjk...r}^k \delta G_i \delta G_j \cdots \delta G_r + \epsilon_{\phi}^k \end{aligned} \quad (6)$$

[0076] where $\lambda_{1,1}^k, \lambda_{1,2}^k, \dots, \lambda_{1,m}^k$ and $\lambda_{p,1}^k, \lambda_{p,2}^k, \dots, \lambda_{p,m}^k$ are the coefficients of the first, second, ..., and p -th order perturbations for the eigenvalue, $\phi_{1,1}^k, \phi_{1,2}^k, \dots, \phi_{1,m}^k$ and $\phi_{p,1}^k, \phi_{p,2}^k, \dots, \phi_{p,m}^k$ are the coefficient vectors of the first, second, ..., and p -th order perturbations for the eigenvector, and ϵ_{λ}^k and ϵ_{ϕ}^k are the residuals of order $p+1$. Note that the numbers in the parentheses in the subscripts of the coefficients and coefficient vectors indicate the orders of the terms. By the Taylor expansion, one has for any $p \geq 1$,

$$p! \lambda_{p,1}^k = \frac{\partial^p \lambda^k}{\partial G_1 \partial G_2 \cdots \partial G_p} \quad p! \phi_{p,1}^k = \frac{\partial^p \phi^k}{\partial G_1 \partial G_2 \cdots \partial G_p} \quad (7)$$

[0077] By (7),

$$\lambda_{p,1}^k = \phi_{p,1}^k \frac{\partial^p \lambda^k}{\partial G_1 \partial G_2 \cdots \partial G_p} \quad (8)$$

[0078] are symmetric in the p indices, i,j, . . . , and t. The right-hand sides of (7) are the p-th order sensitivities of the eigenvalues and eigenvectors with respect to the stiffness parameters.

[0079] Using the normalization relations of the eigenvectors, ψ^k and ϕ_d^k , and symmetry of the coefficient vectors in (6), as indicated earlier, one obtains

$$1 = (\phi_d^k)^T M \phi_d^k \quad (8)$$

$$= \left(\phi^k + \sum_{j=1}^m c_{(1)j}^k \delta G_j + \sum_{i=1}^n \sum_{j=1}^m c_{(2ij)}^k \delta G_i \delta G_j + \dots + \sum_{i=1}^n \sum_{j=1}^m \dots \sum_{t=1}^n c_{(p(ij)...t)}^k \delta G_i \delta G_j \dots \delta G_t \delta G_i + \dots \right)^T$$

$$= \left(\phi^k + \sum_{i=1}^m c_{(1)i}^k \delta G_i + \sum_{i=1}^n \sum_{j=1}^m c_{(2ij)}^k \delta G_i \delta G_j + \dots + \sum_{i=1}^n \sum_{j=1}^m \dots \sum_{t=1}^n c_{(p(ij)...t)}^k \delta G_i \delta G_j \dots \delta G_t \delta G_i + \dots \right)^T$$

$$1 + \sum_{i=1}^m [(\phi^k)^T M c_{(1)i}^k + (c_{(1)i}^k)^T M \phi^k]$$

$$\begin{aligned} & \delta G_i + \\ & \sum_{i=1}^n \sum_{j=1}^m \frac{1}{R_{ij}^k} [2\mathbb{I}(\phi^k)^T M c_{(2ij)}^k + (c_{(1)j}^k)^T M c_{(1)i}^k + (c_{(1)j}^k)^T M c_{(1)i}^k + 2\mathbb{I}(c_{(1)j}^k)^T M \phi^k] \delta G_i \delta G_j + \end{aligned}$$

$$\begin{aligned} & \sum_{i=1}^n \sum_{j=1}^m \sum_{t=1}^n \frac{1}{R_{ij}^k} [3\mathbb{I}(\phi^k)^T M c_{(3ijt)}^k + 2\mathbb{I}(c_{(1)j}^k)^T M c_{(2ij)}^k + (c_{(1)j}^k)^T M c_{(2ij)}^k + (c_{(1)j}^k)^T M c_{(3ijt)}^k] + \end{aligned}$$

$$2\mathbb{I}[(c_{(1)j}^k)^T M c_{(1)i}^k + (c_{(2ij)}^k)^T M c_{(1)i}^k + (c_{(2ij)}^k)^T M c_{(1)i}^k] \delta G_i \delta G_j \delta G_i +$$

$$\dots + \sum_{i=1}^n \sum_{j=1}^m \dots \sum_{t=1}^n \frac{1}{R_{ij}^k} [p\mathbb{I}(\phi^k)^T M c_{(p(ij)...t)}^k + (p-1)!]$$

$$\begin{aligned} & [(c_{(1)j}^k)^T M c_{(p(ij)...t)}^k + (c_{(2ij)}^k)^T M c_{(p(ij)...t)}^k + \dots + (c_{(1)j}^k)^T M c_{(p(ij)...t)}^k] + \\ & 2\mathbb{I}(p-2)[(c_{(2ij)}^k)^T M c_{(p-2)j-i}^k + (c_{(2ij)}^k)^T M c_{(p-2)j-i}^k + \dots + (c_{(2ij)}^k)^T M c_{(p-2)j-i}^k] + \dots + \\ & (p-2)(2\mathbb{I})[(c_{(p-2)j-i}^k)^T M c_{(2ij)}^k + (c_{(p-2)j-i}^k)^T M c_{(2ij)}^k + \dots + (c_{(p-2)j-i}^k)^T M c_{(2ij)}^k] + \\ & (p-1)\mathbb{I}[(c_{(p-1)j-i}^k)^T M c_{(1)j}^k + (c_{(p-1)j-i}^k)^T M c_{(1)j}^k + \dots + (c_{(p-1)j-i}^k)^T M c_{(1)j}^k] + \\ & p\mathbb{I}[(c_{(p)j-i}^k)^T M \phi^k] \delta G_i \delta G_j \dots \delta G_t \delta G_i + \dots \end{aligned}$$

[0080] where the superscript T denotes transpose. For any p-th ($p \geq 1$) order term in the last expression of (8), the coefficient

$$R_{0 \dots r}^i$$

[0081] is defined by

$$R_{0 \dots r}^i = X_1 X_2 \dots X_n,$$

[0082] where X_1, X_2, \dots, X_n ($1 \leq \alpha \leq p$) are the numbers of the first, second, \dots , and last distinct indices within indices, i, j, \dots , and t, with $X_1 + X_2 + \dots + X_n = p$. For instance, $R_{1234} = 1!1!1!1!1! = 1$ with $a=4$, and $R_{112223} = 2!3!1! = 2!3!$ with $a=3$. Some explanations of the general p-th order term in the last expansion in (8) are in order. It includes $p+1$ types of terms ordered from the beginning to the end of the expression within the braces, with each type of terms except the first and last ones enclosed in square brackets. The c-th ($1 \leq c \leq p+1$) type of terms is obtained by multiplying a (c-1)-th order term in the expansion of $(\phi_d^k)^T$ by a (p-c+1)-th order term in the expansion of $M\phi_d^k$. For the c-th type of term, where $2 \leq c \leq p$, the p indices, i, j, \dots , and t are distributed in the subscripts of the two vectors pre- and post-multiplying M, whose numbers of indices in the subscripts are c-1 and p-c+1 respectively. For the first and last ((p+1)-th) types of terms, all the p indices lie in the subscripts of the vectors post- and pre-multiplying M, respectively. The number of terms within each set of square brackets equals the number of different combinations of indices in the subscripts of the vectors pre- and post-multiplying M. When all the p indices, i, j, \dots , and t, have distinct values, due to symmetry of these vectors in their indices, terms of the c-th ($1 \leq c \leq p+1$) type, involving different permutations of the same indices in the subscripts of the vectors, are equal and combined, resulting in the scaling factor $(c-1)(p-c+1)!$ in front of the square brackets. Consequently, the indices in the second through p-th summations range from the values of their preceding summation indices to m. When any of the p indices, i, j, \dots , and t, have equal values, the corresponding terms in each type are given by those in the previous case divided by

$$R_{0 \dots r}^i$$

[0083] For instance, the 4th order term of the form $\delta G_i \delta G_j$ ³ in the expansion of $(\phi_d^k)^T M\phi_d^k$ can be obtained from the expression for the p-th order term in (8):

$$\begin{aligned} & \frac{1}{1!3!} [4(\phi_d^k)^T M_{01222}^k + 3[(\phi_{112}^k)^T M_{01222}^k + (\phi_{112}^k)^T M_{01222}^k + \\ & (\phi_{0112}^k)^T M_{01222}^k + (\phi_{0112}^k)^T M_{01222}^k] + \\ & 2!2![(\phi_{0112}^k)^T M_{01222}^k + (\phi_{0112}^k)^T M_{01222}^k + \end{aligned} \quad (9)$$

-continued

$$\begin{aligned} & (\phi_{0112}^k)^T M_{01222}^k + (\phi_{0112}^k)^T M_{01222}^k + \\ & 3[(\phi_{011222}^k)^T M_{0112}^k + (\phi_{011222}^k)^T M_{0112}^k + \\ & (\phi_{011222}^k)^T M_{0112}^k + (\phi_{011222}^k)^T M_{0112}^k + \\ & 4[(\phi_{011222}^k)^T M_{0112}^k + (\phi_{011222}^k)^T M_{0112}^k = \\ & [4(\phi_d^k)^T M_{012222}^k + [(\phi_{111}^k)^T M_{012222}^k + 3(\phi_{111}^k)^T M_{012222}^k + \\ & 4(\phi_{01112}^k)^T M_{012222}^k + [(\phi_{01112}^k)^T M_{012222}^k + \\ & 3[(\phi_{011122}^k)^T M_{0112}^k + 4(\phi_{011122}^k)^T M_{0112}^k] \} \delta G_1 \delta G_2^3 = \end{aligned}$$

[0084] where p=4 and the four indices involved, i, j, l, and o, are i=1 and j=l=o=2.

[0085] Equating the coefficients of the δG_i (i=1, 2, \dots , m) terms in (8) and using symmetry of the mass matrix yields

$$(\phi^k)^T M_{ij}^k \phi^{j-k} = \quad (10)$$

[0086] Equating the coefficients of the $\delta G_i \delta G_j$ terms and using symmetry of M and $z_{(cij)}^k$ yields

$$(\phi^k)^T M_{ijkl}^k = -\frac{1}{2!} (\phi_{112}^k)^T M_{ijkl}^k \quad (11)$$

[0087] for all i, j=1, 2, \dots , m. Following a similar procedure, one obtains

$$\begin{aligned} & (\phi^k)^T M_{ijpq}^k = \quad (12) \\ & -\frac{2!}{3!} [(\phi_{112}^k)^T M_{ijpq}^k + (\phi_{112}^k)^T M_{iqjk}^k + (\phi_{112}^k)^T M_{iqkj}^k] \end{aligned}$$

[0088] for i, j,l=1, 2, \dots , m. Equating the coefficients of the $\delta G_i \delta G_j \dots \delta G_s \delta G_t$ terms of p-th order in (8) yield

$$\begin{aligned} & (\phi^k)^T M_{ijpqrs}^k = \quad (13) \\ & -\frac{1}{2(p!)^2} [(p-1)![(\phi_{112}^k)^T M_{ijpq-1s}^k + (\phi_{112}^k)^T M_{ijpq-1s}^k + \\ & \dots + (\phi_{112}^k)^T M_{z_{ijpq-1s}}^k] + \\ & 2!(p-2)![(\phi_{112}^k)^T M_{z_{ijpq-2s}}^k + (\phi_{112}^k)^T M_{z_{ijpq-2s}}^k + \\ & \dots + (\phi_{112}^k)^T M_{z_{ijpq-2s}}^k] + \dots + \\ & (p-2)!2![(\phi_{112}^k)^T M_{z_{ijpq-2s}}^k + (\phi_{112}^k)^T M_{z_{ijpq-2s}}^k + \\ & \dots + (\phi_{112}^k)^T M_{z_{ijpq-2s}}^k] + \dots + \\ & (p-1)![(\phi_{112}^k)^T M_{z_{ijpq-1s}}^k + (\phi_{112}^k)^T M_{z_{ijpq-1s}}^k + \\ & \dots + (\phi_{112}^k)^T M_{z_{ijpq-1s}}^k]] \end{aligned}$$

[0089] for i, j, \dots , l=1, 2, \dots , m. The p-1 types of terms, enclosed in the p-1 sets of square brackets on the right-hand side of (13), are ordered from the beginning to the end of the expression within the braces, and their structures are readily observed. When p is odd, by symmetry of

[0096] where

$$M \text{ and } \zeta_{(1)y}^l, r, \text{ the } y - th \left(1 \leq y \leq \frac{p-l}{2} \right)$$

$$P_{(1)w}^l$$

[0090] type of terms is identical to the (p-y)-th type, and the two types of terms can be combined. Similarly, when p is even, the

$$y - th \left(1 \leq y \leq \frac{p}{2} - 1 \right)$$

[0091] type of terms equals and can be combined with the (p-y)-th type of terms. In this case, however, there is a separate type, the

$$\left(\frac{p}{2} \right) - th \text{ type,}$$

[0092] of terms in the middle of the expression.

[0093] Substituting (4)-(6) into (3) yields

$$\begin{aligned} & \left\{ K + \sum_{i=1}^m \frac{\partial K}{\partial G_i} \delta G_i \right\} \left\{ \phi^l + \sum_{i=1}^m \zeta_{(1)y}^i \delta G_i + \sum_{i=1}^m \sum_{j=1}^m \zeta_{(2)y}^{ij} \delta G_i \delta G_j + \right. \\ & \quad \left. \sum_{i=1}^m \sum_{j=1}^m \sum_{k=1}^m \zeta_{(3)y}^{ijk} \delta G_i \delta G_j \delta G_k + \dots \right\} = P_{(1)kl}^l = 0 \quad (18) \\ & \left\{ \lambda^l + \sum_{i=1}^m \lambda_{(1)y}^i \delta G_i + \sum_{i=1}^m \lambda_{(2)y}^{iij} \delta G_i \delta G_j + \right. \\ & \quad \left. \sum_{i=1}^m \sum_{j=1}^m \sum_{k=1}^m \lambda_{(3)y}^{ijk} \delta G_i \delta G_j \delta G_k + \dots \right\} \\ & M \left\{ \phi^l + \sum_{i=1}^m \zeta_{(1)y}^i \delta G_i + \sum_{i=1}^m \sum_{j=1}^m \zeta_{(2)y}^{ij} \delta G_i \delta G_j + \right. \\ & \quad \left. \sum_{i=1}^m \sum_{j=1}^m \sum_{k=1}^m \zeta_{(3)y}^{ijk} \delta G_i \delta G_j \delta G_k + \dots \right\} \quad \zeta_{(1)y}^l. \end{aligned}$$

[0094] Equating the coefficients of the δG_i ($i=1, 2, \dots, m$) terms in (14) yields

$$K \zeta_{(1)y}^l + \frac{\partial K}{\partial G_i} \phi^l = \lambda^l M \zeta_{(1)y}^l + \lambda_{(1)y}^l M \phi^l \quad (15)$$

[0092] Equating the coefficients of the $\delta G_i \delta G_j$ terms in (14) yields

$$2K \zeta_{(1)y}^l + \frac{\partial K}{\partial G_i} \zeta_{(1)y}^l + \frac{\partial K}{\partial G_j} \zeta_{(1)y}^l = 2\lambda^l M \zeta_{(2)y}^l + \lambda_{(1)y}^l M \zeta_{(1)y}^l + \lambda_{(1)y}^l M Z_{(1)y}^l + 2\lambda_{(2)y}^l M \phi^l \quad (20)$$

[0095] Expanding $Z_{(1)y}^l$ using normalized eigenvectors of (1) as basis vectors, one has

[0103] Expanding

$$\zeta_{(1)y}^l = \sum_{w=1}^N P_{(1)wy}^l \phi^w \quad (16)$$

$$\zeta_{(2)y}^l$$

[0104] using normalized eigenvectors of (1) as basis vectors, one has

$$\zeta_{(2)ij}^k = \sum_{u=1}^N P_{(2)ju}^k \phi^u$$

[0105] where

$$P_{(2)ju}^k$$

[0106] is the coefficient of the u-th term and the number in the parentheses in its subscript corresponds to that of

$$\zeta_{(2)ij}^k,$$

[0107] Pre-multiplying (20) by $(\phi^k)^T$ and using (1), (2), (10), and (21) yields

$$\lambda_{(2)ij}^k = \frac{1}{2!} (\phi^k)^T \left[\frac{\partial K}{\partial G_i} \zeta_{(1)j}^k + \frac{\partial K}{\partial G_j} \zeta_{(1)i}^k \right] \quad (22)$$

[0108] Substituting (21) into (11) and using (2) yields

$$P_{(2)jv}^k = -\frac{1}{2!} (\zeta_{(1)v}^k)^T M_{(2)ij}^k \quad (23)$$

[0109] Pre-multiplying (20) by $(\psi^v)^T$, where $1 \leq v \leq N$ and $v \neq k$, and using (1), (2), and (21) yields

$$\begin{aligned} P_{(2)jv}^k &= \frac{1}{2!(\lambda^k - \lambda^v)} (\phi^k)^T \\ &\quad \left\{ \left[\frac{\partial K}{\partial G_i} \zeta_{(1)j}^k + \frac{\partial K}{\partial G_j} \zeta_{(1)i}^k \right] - [\lambda_{(1)v}^k M_{(2)ij}^k + \lambda_{(1)j}^k M_{(2)vi}^k] \right\} \end{aligned} \quad (24)$$

[0110] By (21), (23) and (24) we have determined

$$\zeta_{(2)jv}^k$$

[0111] Equating the coefficients of the $\delta G_i \delta G_j$ terms in (14) yields

$$\begin{aligned} 3! K_{(2)ij}^k + 2! \left[\frac{\partial K}{\partial G_i} \zeta_{(2)jv}^k + \frac{\partial K}{\partial G_j} \zeta_{(2)iv}^k + \frac{\partial K}{\partial G_v} \zeta_{(2)ij}^k \right] = \\ 3! \lambda^k M_{(2)ijv}^k + 2! [\lambda_{(1)v}^k M_{(2)ij}^k + \lambda_{(1)j}^k M_{(2)vi}^k + \lambda_{(1)v}^k M_{(2)ji}^k] + \end{aligned} \quad (25)$$

$$- \text{continued}$$

$$2! [\lambda_{(1)v}^k M_{(2)ij}^k + \lambda_{(1)j}^k M_{(2)vi}^k] 3! \lambda_{(2)jv}^k M_{(2)ij}^k$$

[0112] Expanding

$$\zeta_{(3)jv}^k$$

[0113] using normalized eigenvectors of (1) as basis vectors, one has

$$\zeta_{(3)jv}^k = \sum_{u=1}^N P_{(3)juv}^k \phi^u \quad (26)$$

[0114] where

$$P_{(3)juv}^k$$

[0115] is the coefficient of the u-th term and the number in the parentheses in its subscript corresponds to that of

$$\zeta_{(3)juv}^k$$

[0116] Pre-multiplying (25) by $(\phi^v)^T$ and using (1), (2), (10), and (26) yields

$$\begin{aligned} \lambda_{(3)jv}^k &= \frac{2!}{3!} (\phi^v)^T \left[\frac{\partial K}{\partial G_i} \zeta_{(2)jv}^k + \frac{\partial K}{\partial G_j} \zeta_{(2)iv}^k + \right. \\ &\quad \left. \frac{\partial K}{\partial G_v} \zeta_{(2)ij}^k - \lambda_{(1)v}^k M_{(2)ij}^k - \lambda_{(1)j}^k M_{(2)vi}^k - \lambda_{(1)v}^k M_{(2)ji}^k \right] \end{aligned} \quad (27)$$

[0117] Substituting (26) into (12) and using (2) yields

$$P_{(3)jv}^k = -\frac{2!}{3!} [(\zeta_{(1)v}^k)^T M_{(2)ij}^k + (\zeta_{(1)j}^k)^T M_{(2)vi}^k + (\zeta_{(1)v}^k)^T M_{(2)ji}^k] \quad (28)$$

[0118] Pre-multiplying (25) by $(\phi^v)^T$, where $1 \leq v \leq N$ and $v \neq k$, and using (1), (2), and (26) yields

$$\begin{aligned} P_{(3)jv}^k &= \frac{2!}{3!(\lambda^k - \lambda^v)} (\phi^v)^T \left[\frac{\partial K}{\partial G_i} \zeta_{(2)jv}^k + \frac{\partial K}{\partial G_j} \zeta_{(2)iv}^k + \frac{\partial K}{\partial G_v} \zeta_{(2)ij}^k - \lambda_{(1)v}^k M_{(2)ij}^k - \right. \\ &\quad \left. \lambda_{(1)j}^k M_{(2)iv}^k - \lambda_{(1)v}^k M_{(2)iv}^k - \lambda_{(1)j}^k M_{(2)vi}^k - \lambda_{(1)v}^k M_{(2)ji}^k \right] \end{aligned} \quad (29)$$

[0119] By (26), (28) and (29) we have determined

$$\zeta_{(3)jv}^k$$

[0120] We proceed now to derive the perturbation solutions for the general p-th order terms in (5) and (6). Equating the coefficients of the $\delta G_1 \dots \delta G_p \delta G_1$ terms of order p in (14) yields

$$\begin{aligned} & p! K_{\alpha(p)}^{\beta} \delta_{[p]}^{[p]} \dots \alpha + (p-1)! \left[\frac{\partial K}{\partial G_j} \delta_{[p-1]j}^{[p]} \dots \alpha + \frac{\partial K}{\partial G_j} \delta_{[p-1]k}^{[p]} \dots \alpha + \dots + \right. \\ & \quad \left. \frac{\partial K}{\partial G_j} \delta_{[p-1]l}^{[p]} \dots \alpha \right] \\ & = p! \lambda_1^k M_{\alpha(p)}^{\beta} \dots \alpha + (p-1)! [\lambda_{11}^k M_{\alpha(p-1)}^{\beta} \dots \alpha + \\ & \quad \lambda_{11}^k M_{\alpha(p-1)j}^{\beta} \dots \alpha + \dots + \lambda_{11}^k M_{\alpha(p-1)l}^{\beta} \dots \alpha + \\ & \quad 2!(p-2)! \lambda_{12}^k M_{\alpha(p-2)j}^{\beta} \dots \alpha + \lambda_{12}^k M_{\alpha(p-2)l}^{\beta} \dots \alpha + \dots + \\ & \quad \lambda_{12}^k M_{\alpha(p-2)k}^{\beta} \dots \alpha + \dots + p! \lambda_{1p}^k M_{\alpha(p)}^{\beta} \dots \alpha] \end{aligned} \quad (30)$$

[0121] Expanding

$$\delta_{[p]}^{[p]} \delta_{[p]}^{[p]} \dots \alpha$$

[0122] using normalized eigenvectors of (1) as basis vectors, one has

$$\delta_{[p]}^{[p]} \delta_{[p]}^{[p]} \dots \alpha = \sum_{u=1}^n P_{[p]u} \delta_{[p]}^{[p]} \dots \alpha u^k \quad (31)$$

[0123] where

$$P_{[p]u}^{[p]} \delta_{[p]}^{[p]} \dots \alpha$$

[0124] is the coefficient of the u-th term and the number in the parenthesis in its subscript corresponds to that of

$$\delta_{[p]}^{[p]} \delta_{[p]}^{[p]} \dots \alpha$$

[0125] Pre-multiplying (30) by $(\Phi^k)^T$ and using (1), (10), (31) and orthonormality relations of eigenvectors yields

$$\begin{aligned} \lambda_{[p]}^k \delta_{[p]}^{[p]} \dots \alpha &= \frac{1}{p!} (\Phi^k)^T [(p-1)! \left(\frac{\partial K}{\partial G_j} \delta_{[p-1]j}^{[p]} \dots \alpha + \right. \\ & \quad \left. \frac{\partial K}{\partial G_j} \delta_{[p-1]k}^{[p]} \dots \alpha + \dots + \frac{\partial K}{\partial G_j} \delta_{[p-1]l}^{[p]} \dots \alpha \right) - \\ & \quad (p-1)! \lambda_{11}^k M_{\alpha(p-1)j}^{\beta} \dots \alpha + \lambda_{11}^k M_{\alpha(p-1)l}^{\beta} \dots \alpha + \dots + \\ & \quad \lambda_{11}^k M_{\alpha(p-1)k}^{\beta} \dots \alpha - 2!(p-2)! \lambda_{12}^k M_{\alpha(p-2)j}^{\beta} \dots \alpha + \\ & \quad \lambda_{12}^k M_{\alpha(p-2)l}^{\beta} \dots \alpha + \dots + \lambda_{12}^k M_{\alpha(p-2)k}^{\beta} \dots \alpha - \dots - \\ & \quad (p-2)! 12! (\lambda_{1p}^k M_{\alpha(p-2)j}^{\beta} \dots \alpha + \lambda_{1p}^k M_{\alpha(p-2)l}^{\beta} \dots \alpha + \dots + \\ & \quad \lambda_{1p}^k M_{\alpha(p-2)k}^{\beta} \dots \alpha)] \end{aligned} \quad (32)$$

[0126] The p-th order sensitivities of eigenvalues are obtained from (7) and (32). They depend on the eigenvalue and eigenvector sensitivities of orders up to p-2 and p-1 respectively. Substituting (31) into (13) and using (2) yields

$$\begin{aligned} P_{[p]q}^{[p]} \delta_{[p]}^{[p]} \dots \alpha &= \\ & \frac{1}{2(p-1)!} [(p-1)! \left((\lambda_{11}^k)^T M_{\alpha(p-1)k}^{\beta} \dots \alpha + (\lambda_{11}^k)^T M_{\alpha(p-2)k}^{\beta} \dots \alpha + \dots + \right. \\ & \quad (\lambda_{11}^k)^T M_{\alpha(p-1)l}^{\beta} \dots \alpha + 2!(p-2)! \left((\lambda_{12}^k)^T M_{\alpha(p-2)l}^{\beta} \dots \alpha + \right. \\ & \quad (\lambda_{12}^k)^T M_{\alpha(p-2)j}^{\beta} \dots \alpha + \dots + (\lambda_{12}^k)^T M_{\alpha(p-2)k}^{\beta} \dots \alpha + \dots + \\ & \quad (p-2)! 12! \left((\lambda_{1p}^k)^T M_{\alpha(p-2)k}^{\beta} \dots \alpha + (\lambda_{1p}^k)^T M_{\alpha(p-2)l}^{\beta} \dots \alpha + \right. \\ & \quad \dots + (\lambda_{1p}^k)^T M_{\alpha(p-2)j}^{\beta} \dots \alpha + (p-1)! \left((\lambda_{1(p-1)k}^k)^T M_{\alpha(p-1)k}^{\beta} \dots \alpha + \right. \\ & \quad (\lambda_{1(p-1)k}^k)^T M_{\alpha(p-1)l}^{\beta} \dots \alpha + \dots + (\lambda_{1(p-1)k}^k)^T M_{\alpha(p-1)j}^{\beta} \dots \alpha)] \end{aligned} \quad (33)$$

[0127] Pre-multiplying (30) by $(\Phi^v)^T$, where $1 \leq v \leq N$ and $v \neq k$, and using (1), (2), and (31) yields

$$\begin{aligned} P_{[p]q}^{[p]} \delta_{[p]}^{[p]} \dots \alpha &= \\ & \frac{1}{p! (k-1)!} (\Phi^v)^T [(p-1)! \left(\frac{\partial K}{\partial G_j} \delta_{[p-1]j}^{[p]} \dots \alpha + \frac{\partial K}{\partial G_j} \delta_{[p-1]k}^{[p]} \dots \alpha + \right. \\ & \quad \dots + \left. \frac{\partial K}{\partial G_j} \delta_{[p-1]l}^{[p]} \dots \alpha \right) - (p-1)! \\ & \quad (\lambda_{11}^k M_{\alpha(p-1)j}^{\beta} \dots \alpha + \lambda_{11}^k M_{\alpha(p-1)k}^{\beta} \dots \alpha + \dots + \lambda_{11}^k M_{\alpha(p-1)l}^{\beta} \dots \alpha) - \\ & \quad 2!(p-2)! (\lambda_{12}^k M_{\alpha(p-2)j}^{\beta} \dots \alpha + \lambda_{12}^k M_{\alpha(p-2)k}^{\beta} \dots \alpha + \dots + \\ & \quad \lambda_{12}^k M_{\alpha(p-2)l}^{\beta} \dots \alpha) - \dots - (p-1)! (\lambda_{1p}^k M_{\alpha(p-1)j}^{\beta} \dots \alpha + M_{\alpha(p-1)k}^{\beta} \dots \alpha + \\ & \quad \lambda_{1p}^k M_{\alpha(p-1)l}^{\beta} \dots \alpha + \dots + \lambda_{1p}^k M_{\alpha(p-1)j}^{\beta} \dots \alpha)] \end{aligned} \quad (34)$$

[0128] By (31), (33) and (34) we have determined

$$\delta_{[p]}^{[p]} \delta_{[p]}^{[p]} \dots \alpha$$

[0129] The p-th order sensitivities of eigenvectors can be subsequently obtained from (7). They depend on the eigenvalue and eigenvector sensitivities of orders up to p-1.

[0130] Equations (5) and (6) serve both the forward and inverse problems. In the former one determines the changes in the eigenparameters with changes in the stiffness parameters. Damage detection is treated as an inverse problem, in which one identifies iteratively the changes in the stiffness parameters from a selected set of measured eigenparameters of the damaged structure: λ_d^k ($k=1, 2, \dots, n_d$) and Φ_d^k ($k=1, 2, \dots, n_\Phi$), where $1 \leq k \leq n_d$, $n_\Phi \leq N$. Here λ_d^k and Φ_d^k are assumed to be the perfect eigenparameters; simulated noise is included in the measured eigenparameters in the beam and frame examples that follow. Often we choose a set of n measured eigenparameter pairs to detect damage, i.e., $n_d = n_\Phi = n$. Let the number of the measured degrees of freedom of Φ_d^k be N_m ; $N_m = N$ and $N_m < N$ when we have complete and incomplete eigenvector measurements, respectively. With reduced measurements the unmeasured degrees of freedom of Φ_d^k is estimated first using a modified

eigenvector expansion method (see the beam and frame examples below) and Φ_d^k is mass-normalized subsequently. Only the component equations corresponding to the measured degrees of freedom of Φ_d^k are used in (6). The system equations in Eqs. (5) and (6) involves $n_x+n_\phi N_m$ scalar equations with m unknowns, which are in general determinate if $n_x+n_\phi N_m=m$, under-determined if $n_x+n_\phi N_m < m$, and over-determined if $n_x+n_\phi N_m > m$. In the first iteration, λ^k and Φ^k in (5) and (6) correspond to the eigenparameters of the structure with the initial stiffness parameters $G_i^{(0)}$. With the perturbation terms determined as shown above, the changes in the stiffness parameters $\delta G_i^{(0)}$, where the number in the superscript denotes the iteration number, can be solved from (5) and (6) using an optimization method discussed below. The estimated stiffness parameters of the damaged structure are updated by $G_i^{(1)}=G_i^{(0)}+\delta G_i^{(1)}$. With the updated stiffness parameters, the eigenparameters, λ^k and Φ^k , in (5) and (6) are re-calculated from the eigenvalue problem (1) and the perturbation terms are re-evaluated. One subsequently finds $\delta G_i^{(2)}$ using the same method as that in the first iteration. This process is continued until the termination criterion, $|\delta G_i^{(L)}| < \epsilon$, where L is the last iteration number and ϵ is some small constant, is satisfied for all $i=1, 2, \dots, m$. Note that after the w -th ($1 \leq w \leq L$) iteration, we set $G_i^{(w)}$ to G_{hi} if $G_i^{(w)} > G_{hi}$ and to zero or some small stiffness value ϵ_G if $G_i^{(w)} < 0$. A flowchart for the iterative algorithm is shown in FIG. 1B. When a single iteration is used, the iterative method becomes a direct method.

[0131] FIG. 1B shows steps included in a method for detecting structural damage in accordance with one embodiment of the present invention. The method includes as an initial step measuring one or more eigenparameters, λ^k, Φ^k (Block 1). These eigenparameters are then compared with estimated eigenparameters associated with the stiffness parameters, $G_i^{(0)}$ (Block 2). The differences between the measured and estimated eigenparameters are then used by the perturbation method to establish system equations (5) and (6) (Block 3). The perturbation method may be a first or higher order multiple-parameter perturbation procedure.

[0132] Next, an optimization method may be used to find the changes in the stiffness parameters $\delta G_i^{(w)}$ (Block 4). These values are then compared to the predetermined value ϵ (Block 5), and if the absolute values are less than ϵ the stiffness parameters identified are set as $G_i^{(w-1)}$ (Block 6).

[0133] If the absolute values are not all less than ϵ , the process proceeds along an iterative path where the stiffness parameters are first updated (Block 7). The stiffness parameters are then bounded between 0 or ϵ_G and G_{hi} (Block 8), and eigenparameters associated with the updated stiffness parameters are calculated (Block 9). The comparison of Block 2 is then performed based on these calculated, or estimated, eigenparameters.

[0134] Optimization Methods

[0135] Neglecting the residuals of order $p+1$ in (5) and (6) yields a system of polynomial equations of order p . When $n_x+n_\phi N_m \leq m$, $\delta G_i^{(w)} (i=1, 2, \dots, m)$ at the w -th iteration can be solved from the resulting equations. There are generally an infinite number of solutions when $n_x+n_\phi N_m < m$, a unique solution when $n_x+n_\phi N_m = m$ and $p=1$, and a finite number of solutions when $n_x+n_\phi N_m = m$ and $p>1$. When $n_x+n_\phi N_m > m$, one generally cannot find $\delta G_i^{(w)}$ to satisfy all the equations, and an optimization method can be used to find $\delta G_i^{(w)}$ which

minimize an objective function related to the errors in satisfying these equations. We use here the same notations, e_x^k and e_ϕ^k to denote the errors in satisfying the system equations in (5) and (6) respectively. Consider the objective function

$$J = \sum_{k=1}^{n_x} W_x^k (e_x^k)^2 + \sum_{k=1}^{n_\phi} W_\phi^k (e_\phi^k)^T (e_\phi^k) \quad (35)$$

[0136] where W_x^k ($k=1, 2, \dots, n_x$) and W_ϕ^k ($k=1, 2, \dots, n_\phi$) are the weighting factors, and J is a function of $\delta G_i^{(w)}$ when one substitutes the expressions for e_x^k and e_ϕ^k in (5) and (6) into (35). When the first-order perturbations are retained in (5) and (6), the least-squares method can be used to determine $\delta G_i^{(w)}$ which minimize (35) with $W_x^k=W_\phi^k=1$. Other weighting factors can be handled by dividing (5) and (6) by

$$\frac{1}{\sqrt{W_x^k}} \text{ and } \frac{1}{\sqrt{W_\phi^k}}$$

[0137] respectively. The method determines essentially the generalized inverse of the resulting system matrix, and is also known as the generalized inverse method. When the perturbations up to the p -th ($p \geq 1$) order are included in (5) and (6), the gradient and quasi-Newton methods [25] can be used to determine $\delta G_i^{(w)}$ iteratively. Unlike the generalized inverse method, the methods are applicable when other objective functions are defined. While the optimization methods are introduced for over-determined systems, they can be used when $n_x+n_\phi N_m \leq m$, in which case $J=0$ (i.e., $e_x=e_\phi=0$) when the optimal solutions are reached.

[0138] Gradient Method

[0139] To minimize the objective function in (35) at the w -th iteration, one can use the algorithm

$$\delta G_{(b)}^{(w)} = \delta G_{(b-1)}^{(w)} - \alpha_b f_{b-1} \quad (36)$$

[0140] to update the changes in the stiffness parameters, where

$$\delta G_{(b)}^{(w)} = (\delta G_{1(b)}^{(w)}, \delta G_{2(b)}^{(w)}, \dots, \delta G_{m(b)}^{(w)})^T,$$

[0141] $\alpha_b > 0$ is the step size, and f_{b-1} equals the gradient vector

$$g_{b-1} = \left(\frac{\partial J}{\partial G_1^{(w)}}, \frac{\partial J}{\partial G_2^{(w)}}, \dots, \frac{\partial J}{\partial G_m^{(w)}} \right)^T$$

[0142] associated with

$$\delta C_{(b-1)}^{(n)}.$$

[0143] Note that the subscript b ($b \geq 1$) in all the variables in (36) denotes the number of nested iterations. The initial values used are

$$\delta C_{(0)}^{(n)} = 0.$$

[0144] The nested iteration is terminated when $\alpha_b \|g_b\|_\infty < \gamma$, where $\|\cdot\|_\infty$ is the infinity norm and γ is some small constant or the number of nested iterations exceeds an acceptable number, D.

[0145] Quasi-Newton Methods

[0146] Due to its successive linear approximations to the objective function, the gradient method can progress slowly when approaching a stationary point. The quasi-Newton methods can provide a remedy to the problem by using essentially quadratic approximations to the objective function near the stationary point. The iteration scheme of these methods is given by (36) with $B_{b-1} = B_{b-1} \|g_{b-1}\|$, where B_{b-1} is an approximation to the inverse of the Hessian matrix used at the b-th nested iteration, and the other variables the same as those previously discussed. Initially, we set

$$\delta C_{(0)}^{(n)} = 0$$

[0147] and $B_0 = I$, the identity matrix. The matrix B_b is updated using either the DFP formula

$$B_b = B_{b-1} + \frac{(\delta G_{(b)}^{(n)} - \delta G_{(b-1)}^{(n)}) (\delta G_{(b)}^{(n)} - \delta G_{(b-1)}^{(n)})^T}{(\delta G_{(b)}^{(n)} - \delta G_{(b-1)}^{(n)})^T (g_b - g_{b-1})} - \frac{(B_{b-1} (g_b - g_{b-1}) | (B_{b-1} (g_b - g_{b-1}))^T)}{(g_b - g_{b-1})^T B_{b-1} (g_b - g_{b-1})} \quad (37)$$

[0148] or the BFGS formula

$$B_b = B_{b-1} + \left[1 + \frac{(g_b - g_{b-1})^T B_{b-1} (g_b - g_{b-1})}{(\delta G_{(b)}^{(n)} - \delta G_{(b-1)}^{(n)})^T (g_b - g_{b-1})} \right] \frac{(\delta G_{(b)}^{(n)} - \delta G_{(b-1)}^{(n)}) (\delta G_{(b)}^{(n)} - \delta G_{(b-1)}^{(n)})^T}{(\delta G_{(b)}^{(n)} - \delta G_{(b-1)}^{(n)})^T (g_b - g_{b-1})} - \frac{(B_{b-1} (g_b - g_{b-1}) | (B_{b-1} (g_b - g_{b-1}))^T)}{[(\delta G_{(b)}^{(n)} - \delta G_{(b-1)}^{(n)})^T (g_b - g_{b-1})]} \quad (38)$$

[0149] The nested iteration is terminated when $\alpha_b \|B_{b-1} g_b\|_\infty < \gamma$ or the number of iterations exceeds D. A flowchart for

the quasi-Newton methods, including the step size search procedure as outlined below, is shown in FIG. 2.

[0150] Step Size Search Procedure

[0151] The optimal step size for the gradient and quasi-Newton methods is determined in each nested iteration to minimize the function

$$J(\delta C_{(b-1)}^{(n)} - \alpha_b f_{b-1}) = F(x_b)$$

[0152] with respect to α_b . The search procedure is divided into two phases: an initial search to bracket the optimum α_b^* and a golden section search to locate α_b^* within the bracket, as shown in FIG. 2.

[0153] Initial Bracketing. Choose the starting point $x_1 = \mathbf{0}$ and an initial increment $\Delta = 0$. Let $x_2 = x_1 + \Delta$, $F_1 = F(x_1)$, and $F_2 = F(x_2)$. Since for the gradient and quasi-Newton methods, $f_0 = g_0$ and it is along a descent direction of J when Δ is sufficiently small, one has $F_2 < F_1$. Rename 2Δ as Δ , and let $x_3 = x_2 + \Delta$ and $F_3 = F(x_3)$. If $F_3 > F_2$, stop and α_b^* is contained in the interval (x_1, x_2) . Otherwise, rename x_2 as x_1 and x_3 as x_2 , then F_2 becomes F_1 and F_3 becomes F_2 . Rename 2Δ as Δ , and let $x_3 = x_2 + \Delta$ and $F_3 = F(x_3)$. Compare $|x_3 - x_2|$ and $|x_2 - x_1|$, and repeat the above procedure if $F_3 < F_2$ until $F_3 > F_2$, with the final interval (x_1, x_3) containing α_b^* .

[0154] Golden Section Search. If $|x_3 - x_2| > |x_2 - x_1|$, define a new point:

$$x_4 = x_2 + 0.382(x_3 - x_2) \quad (39)$$

[0155] Otherwise, rename x_1 as x_3 and x_3 as x_1 , and then define x_4 using (40). Let $F_4 = F(x_4)$. If $F_2 < F_4$, rename x_4 as x_3 , then F_2 becomes F_3 . Otherwise, rename x_2 as x_3 and x_4 as x_2 , then F_2 becomes F_3 and F_4 becomes F_2 . Compare $|x_3 - x_2|$ and $|x_2 - x_1|$, and repeat the above procedure until $|x_3 - x_2| \leq \epsilon_a$, where ϵ_a is some small constant. Then choose

$$\alpha_b^* = \frac{x_1 + x_2}{2}.$$

MASS-SPRING SYSTEM EXAMPLE

[0156] The algorithm discussed above is used to identify the stiffness parameters of a N-degree-of-freedom system consisting of a serial chain of masses and springs, such as the system shown in FIG. 3. Let the masses of the system be $M_i = 1$ kg ($i = 1, 2, \dots, N$), and the stiffnesses of the undamaged springs be $G_{ij} = 1$ N/m ($i = 1, 2, \dots, m$), where $m = N + 1$. The system is said to have a small, medium and large level of damage if the maximum reduction in the stiffnesses is within 30%, between 30 and 70%, and over 70%, respectively. The mass matrix M is an NxN identity matrix, and the stiffness matrix K is a banded matrix with entries $K_{ii} = G_i + G_{i+1}$ ($i = 1, 2, \dots, N$), $K_{i(i+1)} = K_{(i+1)i} = -G_{i+1}$ ($i = 1, 2, \dots, N - 1$), and all other entries equal to zero. The matrices

$$\frac{\partial K}{\partial G_i} \text{ and } \frac{\partial K}{\partial G_N}$$

[0157] have a unit value in entries (1, 1) and (N, N), respectively, and zero entries elsewhere. The nonzero entries of the matrices

$$\begin{aligned} \frac{\partial K}{\partial G_i} \quad (i = 2, 3, \dots, N-1) \text{ are} \\ \left(\frac{\partial K}{\partial G_i} \right)_{i=1, i=1} = \left(\frac{\partial K}{\partial G_i} \right)_{ii} = 1 \quad \text{and} \\ \left(\frac{\partial K}{\partial G_i} \right)_{i=N-1, i=N} = \left(\frac{\partial K}{\partial G_i} \right)_{iN} = -1. \end{aligned}$$

[0158] We look at a forward problem first with $N=3$ and $m=4$. The stiffnesses of the damaged system are $G_{11}=G_{22}=1/N/m$, $G_{12}=0.3N/m$ and $G_{21}=0N/m$. The undamaged system is considered as the unperturbed system and the damaged system as the perturbed system. Based on the eigenparameters of the undamaged system, the eigensolutions of the damaged system are obtained using the first-, second-, and third-order perturbations, as shown in Table 1 below. The results show that even with the large changes in stiffness, the third-order perturbation solutions compare favorably with the exact solutions for the damaged system. The higher-order perturbation solutions can be used for large order systems when their direct eigensolutions become costly.

Since vanishing stiffness in any spring other than the two end ones in FIG. 1 can result in two decoupled subsystems, when $G_i^{(w)} \leq 0$ we set $G_i^{(w)}$ to $\epsilon_G=0.1N/m$ in the first two iterations and to $0.1N/m$ in the remaining iterations for all the cases considered here. A relatively large value is assigned to ϵ_G in the initial iterations to avoid close eigenvalues in the mass-spring system and small denominators in (19). This improves convergence especially when a small number of eigenparameter pairs are used. A smaller value is used for ϵ_G in the later iterations to improve the accuracy of stiffness estimation when there is a large level of stiffness reduction. Using the first-order perturbations and different numbers of eigenparameter pairs, the maximum errors in estimating the stiffnesses of the damaged system at the w-th iteration, defined by

$$E = \max_{i=1, \dots, N} \frac{|G_i^{(w)} - G_{di}|}{G_{di}} \quad (40)$$

[0160] are shown in FIGS. 4A and 4B for all the iterations. In FIG. 4A p=1 and n=1,2,3, and in FIG. 4B p=1 and n=4,5, ..., 9. When n=1, the error decreases slowly, though monotonically, and there is an estimation error of 1.5% at the end of iteration. While the errors can increase with the iteration number before approaching zero for n=3, they decrease monotonically for n=2 and n≥4. All the stiffnesses are exactly identified at the end of iteration when n≥2. Note that the number of the system equations equals and exceeds the number of unknowns when n=1 and n≥2, respectively. Since the system equations are linear, they have a unique

TABLE I

B eigensolutions of the damaged system from an eigenvalue problem solver (exact) and perturbation analysis

Eigenparameters	Exact	Unperturbed	Perturbed		
			1st order	2nd order	3rd order
λ^1	0.309602	0.58579	0.30576	0.15670	0.30090
λ^2	1.27538	2.00000	1.15000	1.25500	1.29344
λ^3	2.21859	3.44121	2.14424	2.18830	2.20567
Φ^1	$\begin{cases} 0.16516 \\ 0.65733 \\ 0.73528 \end{cases}$	$\begin{cases} 0.50000 \\ 0.70711 \\ 0.50000 \end{cases}$	$\begin{cases} 0.28523 \\ 0.68836 \\ 0.74129 \end{cases}$	$\begin{cases} 0.16111 \\ 0.66444 \\ 0.79452 \end{cases}$	$\begin{cases} 0.12907 \\ 0.65040 \\ 0.76653 \end{cases}$
Φ^2	$\begin{cases} 0.95541 \\ 0.07840 \\ -0.28470 \end{cases}$	$\begin{cases} 0.70711 \\ -0.00000 \\ -0.70711 \end{cases}$	$\begin{cases} 0.95459 \\ 0.10607 \\ -0.45962 \end{cases}$	$\begin{cases} 0.00188 \\ 0.14319 \\ -0.31776 \end{cases}$	$\begin{cases} 0.97976 \\ 0.12310 \\ -0.26810 \end{cases}$
Φ^3	$\begin{cases} 0.24478 \\ -0.74952 \\ 0.61507 \end{cases}$	$\begin{cases} 0.50000 \\ -0.70711 \\ 0.50000 \end{cases}$	$\begin{cases} 0.36477 \\ -0.72586 \\ 0.60871 \end{cases}$	$\begin{cases} 0.29635 \\ -0.74132 \\ 0.62482 \end{cases}$	$\begin{cases} 0.26445 \\ -0.74875 \\ 0.62362 \end{cases}$

[0159] Consider now the damage detection problem with $N=9$, $m=10$, $G_{as}=0.5N/m$, $G_{ds}=0.7N/m$, $G_{d10}=0.8N/m$ and $G_{di}=1N/m$ ($i=1, 2, 3, 4, 5, 6, 7, 9$). We set $W_h^k=W_\Phi^k=1$, $\epsilon=0.001$, $\gamma=10^{-10}$, $\sigma_{i,j}=0$ for all i , and $D=500$; the actual numbers of nested iterations in all the cases are much smaller than D.

solution when n=1, and J has a unique minimum when n≥2. With the small γ gradient method and the quasi-Newton methods using the DFP and BFGS formulas yield exactly the same results as the generalized inverse method (not shown here). Because the generalized inverse method does not

involve any nested iteration, it is the most efficient one among the four methods. While not shown here, the results indicated that that the quasi-Newton methods converge faster than the gradient method and the BFGS method has the similar performance to the DFP method. In what follows the BFGS method will be used with the higher-order perturbations. With the second-order perturbations the errors shown in FIG. 4C decrease monotonically for all n (n=1,2, ..., 9). The errors at w=1 in the expanded view decrease in the order n=3,2,4,9,7,8, with the lines for n=5 and 7 virtually indistinguishable. In FIG. 4(A-C) the following symbols are used for different \rightarrow n=1; \rightarrow n=2; \rightarrow n=3;
 \rightarrow n=4; \rightarrow n=5; \rightarrow n=6; \rightarrow n=7; \rightarrow n=8; \rightarrow n=9. While the use of the second-order perturbations improves the accuracy of stiffness estimation in each iteration and reduces the number of iterations, it takes a much longer time to compute the higher-order perturbations and the associated optimal solutions.

[0161] When only the first few eigenvalues are used, for instance, $n_s=5$ and $n_o=0$, the stiffnesses identified with the first-order perturbations,

$$\begin{aligned} G^{(0)} = & 0.875, 0.976, 0.926, 0.864, 0.699, 0.699, 0.864, \\ & 0.926, 0.976, 0.875 \text{ N/m} \end{aligned} \quad (41)$$

[0162] where the number in the superscript denotes the last iteration number, correspond to those of a different system with the same eigenvalues for the first five modes as the damaged system. The same stiffnesses are identified with the second-order perturbations. Similarly, when the first eigenvector is used, i.e., $n_o=1$ and $n_s=0$, the stiffnesses identified with the first-order perturbations are those of a different system with the same eigenvector for the first mode as the damaged system:

$$\begin{aligned} G^{(0)} = & 0.989, 0.991, 0.995, 1, 0.520, 0.829, 0.940, \\ & 0.668, 0.959, 0.768^T \text{ N/m} \end{aligned} \quad (42)$$

[0163] With the second-order perturbations the stiffnesses of the damaged system are identified. The stiffnesses identified are not unique because the system equations in each iteration are under-determined. The solution given by the generalized inverse method here in each iteration is the minimum norm solution. Increasing the number of eigenparameters used can avoid this problem.

[0164] If the system has a large level of damage, i.e., $G_{ds}=0.3 \text{ N/m}$, $G_{d10}=0.1 \text{ N/m}$, with the other parameters unchanged, the stiffnesses of the damaged system are identified with the first-order perturbations after 55 iterations when $n=1$ and 6 iterations when $n=2$ and 3 as shown in FIG. 5A. For $n=4,5,6,7$, the errors decrease monotonically and the number of iterations is reduced slightly, as shown in FIG. 5B, which has an expanded view near $w=1$. With the second-order perturbations the errors shown in FIG. 5C decrease monotonically for $n=1,2, \dots, 5$, and the number of iteration for $n=1$ is reduced from 55 in FIG. 5A to 4. The errors at $w=1$ in the expanded view in FIG. 5C decrease in the order n=3,2,4,5, with the lines for n=2 and 4 virtually indistinguishable. The symbols used in FIG. 5A-C for $n=1, 2, \dots, 7$ are the same as those in FIG. 4A-C.

[0165] Finally, consider a large order system with a large level of damage: $N=39$, $m=40$, $G_{d12}=0.7 \text{ N/m}$, $G_{d10}=G_{d37}=0.1 \text{ N/m}$, $G_{d28}=0.8 \text{ N/m}$, $G_{d1}=1 \text{ N/m}$ ($1 \leq i \leq 40$ and $i \neq 12, 19, 28, 37$), and the other parameters are the same as those in the previous example. With the first-order perturbations the exact stiffnesses are identified after 57 iterations when $n=1$,

as shown in FIG. 6A. Using a larger number of eigenparameter pairs ($n=2,3,4,5$) significantly reduces the number of iterations, as shown in FIG. 6B. The errors at $w=2$ in the expanded view in FIG. 6B decrease in the order n=4,2,3,5. With the second-order perturbations the exact stiffnesses are identified after 6 iterations when $n=1$ and 3 iterations when $n=2$, as shown in FIG. 6C, which has an expanded view for $1 \leq w \leq 4$. The symbols used in FIG. 6(A-C) for $n=1, 2, \dots, 5$ are the same as those in FIGS. 4A-C and 5A-C.

FIXED-FIXED BEAM EXAMPLE

[0166] The algorithm discussed above may be applied to detecting structural damage in an aluminum beam with fixed boundaries. The beam of length $L=0.7 \text{ m}$, width $W=0.0254 \text{ m}$, and thickness $H=0.0031 \text{ m}$ has an area moment of inertia

$$I = \frac{1}{12} W H^3 = 6.3058 \times 10^{-11} \text{ m}^4$$

[0167] and a mass density $\rho=2715 \text{ kg/m}^3$. The finite element method is used to model its transverse vibration. The beam is divided into N_e elements, as shown in FIG. 7, with the length of each element being

$$l_e = \frac{L_e}{N_e}.$$

[0168] There are N_e+1 nodes. With V_i and θ_i denoting the translational and rotational displacements at node i ($i=1, 2, \dots, N_e+1$), the displacement vector of the i-th ($i=1, 2, \dots, N_e$) element is $[V_{i,0}, V_{i,1}, \theta_{i,1}]^T$. The Young's modulus is assumed to be constant over each beam element and that of the i-th element is denoted by G_i . The Young's modulus of the undamaged beam is $G_u=69 \times 10^9 \text{ N/m}^2$. Hence $G_{ue}=G_u$ for $i=1, 2, \dots, m$, where $m=N_e$. Small to large levels of damage correspond to reductions of the moduli defined for the Mass-Spring Example. The mass and stiffness matrices of the i-th beam element are

$$M_i^e = \frac{\rho W H l_e}{420} \begin{bmatrix} 156 & -22l_e & 54 & 13l_e \\ -22l_e & 4l_e^2 & -13l_e & -3l_e^2 \\ 54 & -13l_e & 156 & 22l_e \\ 13l_e & -3l_e^2 & 22l_e & 4l_e^2 \end{bmatrix}. \quad (43)$$

$$K_i^e = \frac{G_i I}{l_e^3} \begin{bmatrix} 12 & 6l_e & -12 & 6l_e \\ 6l_e & 4l_e^2 & -6l_e & 2l_e^2 \\ -12 & -6l_e & 12 & -6l_e \\ 6l_e & 2l_e^2 & -6l_e & 4l_e^2 \end{bmatrix}$$

[0169] Using the standard assembly process yields the $2(N_e+1) \times 2(N_e+1)$ global mass and stiffness matrices. Constraining the translational and rotational displacements of the two nodes at the boundaries to zero yields the $N \times N$ M and K matrices, where $N=2(N_e+1)$ is the degrees of freedom of the system. The displacement vector of the system, involving the displacements of the 2nd through N_e -th node, is $[V_{2,0}, V_{3,0}, \dots, V_{N_e}, \theta_{N_e}]^T$. The matrix

$$\frac{\partial K}{\partial G_i}$$

[0170] ($i=1, 2, \dots, m$) can be obtained from K by setting $G_1=1$ and $G_2=\dots=G_{i-1}=G_{i+1}=\dots=G_m=0$. The parameters $W_{\lambda}^k, W_{\phi}^k, \epsilon_s, \gamma, \alpha_p$ and α_d are set to the same values as those previously discussed, and ϵ_c is set to 0.15 G_h in the first two iterations and to 0.05 G_h in the remaining iterations. The first-order perturbations are used unless indicated otherwise.

[0171] Consider first the cases with $N_e=m=10$ and $N=18$. When the system has a medium level of damage:

$$G_{\phi}(1, 1, 1, 0.5, 1, 1, 0.7, 1, 1, 0.8)^T \times G_h \quad (44)$$

[0172] the stiffness parameters of the damaged system are identified after 6 iterations with $n=1$. When the system has a large level of damage:

$$G_{\phi}(1, 1, 1, 0.3, 1, 1, 0.7, 1, 1, 0.1)^T \times G_h \quad (45)$$

[0173] the stiffness parameters of the damaged system are identified after 7 iterations with $n=1$. Consider next the cases with $N_e=20, 40$ and 80. For the set with medium and large levels of damage, the stiffness parameters of the first 10 elements are given by (44) and (45), respectively, and those of the remaining elements are G_h . In all the cases the stiffness parameters of the damaged systems are identified within 10 iterations when $n=1$. The numbers of iterations are reduced slightly when the second-order perturbations are used. Note that the system equations are over-determined when $n=1$.

[0174] When only the translational degrees of freedom of an eigenvector are measured, a modified eigenvector expansion method is used to estimate the unmeasured rotational degrees of freedom. To this end, Φ_d^k is partitioned in the form $\Phi_d^k=[(\Phi_m^k)^T, (\Phi_{du}^k)^T]^T$, where Φ_m^k and Φ_{du}^k are the measured and unmeasured degrees of freedom of Φ_d^k , respectively. Similarly, Φ^k in (6) is partitioned in the form $\Phi^k=[(\Phi_m^k)^T, (\Phi_d^k)^T]^T$, where Φ_m^k and Φ_d^k correspond to the measured and unmeasured components of Φ_d^k , respectively. Since Φ_{dm}^k, Φ_m^k and Φ_d^k are known in each iteration, Φ_{du}^k is estimated from $\Phi_{du}^k=k[(\Phi_m^k)^T]^{-1}\Phi_d^k$, where the superscript denotes generalized inverse. Once the rotational degrees of freedom of Φ_d^k are determined, Φ_d^k and Φ^k are converted to their original forms and Φ_d^k is mass-normalized. Only the component equations corresponding to the measured degrees of freedom of Φ_d^k are used in (6) and the system equations are determinate when $n=1$. The exact stiffness parameters of the damaged systems considered above can be identified. For the 10- and 20-element beams with the medium levels of damage, the stiffness parameters are identified after 6 and 24 iterations, respectively, when $n_a=1$ and $n_p=2$. For the 10- and 20-element beams with the large levels of damage, the stiffness parameters are identified after 9 iterations when $n_a=1$ and $n_p=3$ and 10 iterations when $n=2$, respectively.

[0175] Finally, the effects of measurement noise on the performance of the algorithm are evaluated for the 10-element beam with the large level of damage. Simulated noise is included in the measured eigenparameters:

$$\lambda_d = \lambda_d^* + \epsilon_s + v R_{\lambda} \lambda_d^* + \Phi_d = \Phi_d^* + \epsilon_s + v R_{\Phi} \Phi_d^* \quad (46)$$

[0176] where λ_d^* and Φ_d^* are the k -th perfect eigenvalue and eigenvector, respectively, R_{λ} is a uniformly distributed random variable in the interval $[-1, 1]$, R_{Φ} is a diagonal matrix whose diagonal entries are independently, uniformly distributed random variables in the interval $[-1, 1]$, and $v \in [0, 1]$ is the noise level. Note that R_{λ} and R_{Φ} are generated for each measured mode. Each random parameter is generated 10 times and the average is used. Three different noise levels are considered: $v=5\%$, 10% and 20% . When all the degrees of freedom of an eigenvector are measured, the stiffness parameters identified with $n=1, 2$, and 3 are shown in FIGS. 8A, 8B, and 8C, respectively. The following symbols are used for different noise levels: \blacksquare , $v=5\%$; \blacksquare , $v=10\%$; \blacksquare , $v=20\%$. When only the translational degrees of freedom of an eigenvector are measured, and the eigenvector expansion method described above is used and the stiffness parameters identified with $n=2$ and $n=3$ are shown in FIGS. 9A and 9B, respectively. The same symbols as those in FIG. 8A-C are used in FIG. 9A-B for different noise levels. The stiffness parameters corresponding to $v=0$ in FIGS. 8 and 9 are the exact values. It is seen that in the presence of noise, the stiffness parameters can be accurately identified with an increased number of measured eigenparameters.

[0177] Space Frame Example

[0178] The damage detection method can be applied to more complex structures, such as, for example, the modular, four bay space frame shown in FIG. 10. In this example and all the following examples the first order perturbation approach along with the generalized inverse method is used. The four-bay space frame example shown in FIG. 10 is made of extruded aluminum with 48 members, and is 8' tall, 1.46' wide and 1.8' deep. The horizontal and diagonal members have the same cross-sectional dimensions (25.4 mm \times 12.7 mm) and the vertical members are "L"-angles with cross-sectional dimensions 50.8 mm \times 50.8 mm \times 6.35 mm (thickness). All the members are connected through bolted joints. The frame is assumed to be fixed to the ground. The finite element method is used to model the 3-dimensional vibration of the frame, with each member modeled with four 12-degrees-of-freedom beam elements. The total degrees of freedom are 960 when the boundary conditions are applied. The Young's modulus is assumed to be constant over each member and that of the i -th ($1 \leq i \leq m=48$) member is denoted by G_i . The Young's modulus of the undamaged member is $G_h=69 \times 10^9$ N/m 2 and $G_{hi}=G_h$. A vertical (member 1) and a diagonal (member 48) member in the first bay are assumed to have 70% and 30% reductions in Young's modulus, respectively, and all the other members are assumed to be undamaged. The first two vibration modes, corresponding to the bending of the frame along the x and y directions, respectively, are used to detect damage. The translational degrees of freedom of the 16 nodes, denoted by "S" in FIG. 10, along the x and y directions are assumed to be measured with 10% measurement noise. All the other degrees of freedom are estimated using the eigenvector expansion method discussed above and the measured modes are mass-normalized. The Young's moduli of all the members of the damaged truss are identified as shown in FIG. 10, with the maximum estimation error less than 7%. Note that the truss has closely spaced vibration modes. With the modes arranged in the order of increasing frequencies in each iteration, the method has effectively handled mode switching that has occurred in the damage detection process.

[0179] In summary, the damage detection method identifies stiffness parameters in structures, which have a small, medium, and large level of damage if the maximum reduction in the stiffnesses is within 30%, between 30 and 70%, and over 70%, respectively: A large level of damage is studied in many examples because this poses the most challenging case, with sever mismatch between the eigenparameters of the damaged and undamaged structures.

[0180] The damage detection method as embodied and broadly described herein can be applied to structures that can be modeled with beam elements. A beam element is an element that has one dimension that is much longer than the other two. This element is very good at modeling "I"-beams, rectangular beams, circular beams, "L"-angles, "C"-channels, pipes, and beams with varying cross sections. Structures that can be modeled with this element include, but are not limited to, lightning masts, light poles, traffic control poles, pillar type supports, bridges, pipelines, steel building frameworks, television, radio, and cellular towers, space structures, cranes, pipelines, railway tracks, and vehicle frames. Structures that can be modeled as beam elements are used simply for ease of discussion, and it is well understood that the damage detection method discussed above may be applied to structures that can be modeled by other elements using the finite element method or modeled by using other methods.

[0181] Damage Detection Using Changes of Natural Frequencies: Simulation and Experimental Validation

[0182] For structures such as beams and lightning masts in electric substations, using only the changes in the natural frequencies can relatively accurately detect the location(s) and extent of damage, even though the system equations are severely underdetermined in each iteration. This is an interesting finding as it is much easier to measure the natural frequencies than the mode shapes, and demonstrates the effectiveness of the iterative algorithm. Extensive numerical simulations on beams and lightning mast confirmed this finding. Experiments on the beam test specimens with different damage scenarios and a lightning mast in an electric substation validated the simulation results. The beam test specimens and the lightning mast are used as examples for demonstration purposes, and the method can be applied to other structures. Note that unlike the beam example shown earlier, where the Euler-Bernoulli beam finite element model is used, the Timoshenko beam finite element model is used in all the examples here. The Timoshenko beam theory is found to be more accurate in predicting the natural frequencies of the lightning masts and circular beams than the Euler-Bernoulli beam theory.

[0183] For a cantilever beam, simulation results show that the damage located at a position within 0-35% and 50-95% of the length of the beam from the cantilevered end can be easily detected with less than 5 measured natural frequencies, and the damage located at a position within 35-50% of the length of the beam from the cantilevered end and at a position within 5% of the length of the beam from the free end can be relatively accurately detected with 10-15 measured natural frequencies.

[0184] Numerical and Experimental Verification

[0185] Cantilever Aluminum Beams

[0186] Experimental damage detection results for four different scenarios are shown first, followed by various simulation results.

[0187] Scenario 1: Evenly-Distributed Damage Machined from the Top and the Bottom Surfaces of the Beam Test Specimen.

[0188] The aluminum beam test specimen shown in FIG. 12 is 45 cm long by 2.54 cm wide by 0.635 cm thick. It is divided into 40 elements (each element has a length of 1.125 cm). The beam has a section (from approximately 10 cm to 15 cm from the cantilevered end) of 5 cm long and 7.62E-4 m thick machined both from the top and the bottom surfaces of the beam. This corresponds to 56% of damage (or reduction of bending stiffness EI) along the length of five elements (from the 9th to the 13th element). Using the changes of the first 2 to 5 measured natural frequencies, damage is detected within 7 elements using 2 or 5 measured frequencies (from the 7th to the 13th element with 5 measured frequencies and from the 5th to the 11th element with 2 measured frequencies) and within 8 elements using 3 or 4 measured natural frequencies (both from the 6th to the 13th element), as shown in FIG. 13. With 5 measured frequencies the average damage of the 7 elements in FIG. 13, from 6.75 cm to 14.625 cm, is 46%. Note that the elements with damage less than 10% are not accounted for here. The extent of damage detected is slightly lower than the actual extent because the predicted damage occurs at 2 more elements (the 7th and 8th elements) than the actual one. The error results from the solution of the severely underdetermined system equations (5 equations with 80 unknowns).

[0189] Scenario 2: The Same Aluminum Beam Test Specimen as in Scenario 1 Clamped at the Other End.

[0190] The same beam was tested in the clamped-free configuration with the clamped end reversed, which placed the damage from 25 cm to 30 cm (from the 23rd to the 27th element) from the cantilevered end. The damage detection results with 3 to 5 measured frequencies are shown in FIG. 14. With 5 measured frequencies the average damage between 23.625 cm to 32.625 cm (from the 22nd to the 29th element) is 40%. Again the elements with damage less than 10% are not included.

[0191] Scenario 3: Undamaged Cantilever Aluminum Beam Test Specimen with the Same Dimensions as Above.

[0192] An undamaged aluminum beam test specimen was clamped at one end with the same configuration as shown in FIG. 12. With the first 3 to 4 measured frequencies the maximum error for the estimated bending stiffnesses of all the elements is within 10%, as shown in FIG. 15.

[0193] Scenario 4: A Cut of Small Width on a Cantilever Aluminum Beam Test Specimen, Shown in FIG. 16 with the Same Dimensions as Above.

[0194] The beam shown below has a cut that is 0.4191 cm deep and 0.1016 cm wide, which corresponds to a 96% reduction in bending stiffness at the cut. The beam is divided into 45 elements and the cut is located in the middle of the 23rd element. With 3 to 5 measured natural frequencies, the damage is detected at several elements surrounding the 23rd

element, as shown in **FIG. 17**. It was found there was a roughly 50%, 40%, and 60% reduction in stiffness at the 22nd, 23rd, and 24th element, respectively. The estimated damage extent at the above elements is lower than that at the rest because the damage is distributed along these elements.

[0195] To examine the effectiveness and robustness of the damage detection algorithm, various simulations with different damage scenarios were carried out. In this way, we can gain more insight concerning the accuracy of the finite element model, convergence of the estimated bending stiffnesses of all the elements of the beam with the increased numbers of measured natural frequencies and/or mode shapes, and region of the beam within which the damage can be detected with few measured frequencies. With the cantilever aluminum beam divided into 40 elements, the following two simulations have the similar damage location and extent to those in Scenarios 1 and 2 in the experiments:

[0196] Simulation 1: Uniform Damage Between 9.0 cm and 15.75 cm from the Cantilevered End of the Beam with the Same Dimensions as Discussed Above.

[0197] Simulation 2: Uniform Damage Between 29.25 cm and 36 cm from the Cantilevered End of the Beam with the Same Dimensions as Discussed Above.

[0198] Simulation results in **FIG. 18** and **FIG. 19** show that the damage can be relatively accurately detected with the first 3 to 5 measured frequencies, and can be accurately detected with the first 10 measured frequencies.

[0199] With the cantilever aluminum beam divided into the same number of elements, two more simulations are presented here: one for a multiple damage scenario—70% of damage at the 3rd element and 30% of damage at the 20th element, and the other for a 50% of uniform damage from the 16th to the 18th element (i.e., the damage is located at a position within 35-50% of the length of the beam from the cantilevered end).

[0200] Simulation 3: Multiple Damage of the Beam with the Same Dimensions as Discussed Above: 70% of Damage at the 3rd Element and 30% of Damage at the 20th Element.

[0201] Simulation results in **FIG. 20** show that the multiple damage can be relatively accurately detected with the first 3 to 5 measured frequencies, and accurately detected with the first 10 measured frequencies.

[0202] Simulation 4: Uniform Damage from the 16th to the 18th Element of the Beam with the Same Dimensions as Discussed Above.

[0203] Simulation results in **FIG. 21** show that the damage within 35-50% of the length of the beam from the cantilever end can be accurately detected with 10-15 measured frequencies.

[0204] Lightning Masts

[0205] The lighting mast shown in **FIG. 22** has two sections of constant cross-sections and an eccentric spike. The lengths of the lower and upper sections are 6.89 m and 6.83 m, respectively, and that of the spike above the upper section is 1.4375 m. Both mode shapes and natural frequencies were measured for this mast. The mode shapes were measured by using a laser Doppler vibrometer. The natural frequencies were measured using both the laser Doppler vibrometer and an accelerometer. It takes about 0.5-1.5 days

to measure the mode shapes and about 30 minutes to measure the natural frequencies. It would be even more difficult to measure the mode shapes for some of the taller lightning masts, which are 100 and 130 feet tall. A finite element model was made using OpenFEM. Once the model was completed the measured and calculated natural frequencies and mode shapes were compared. The mast was expected to be undamaged, since by inspection the measured and calculated natural frequencies matched (Table 2). It was found that the first mode shape measurement is affected by wind and high modes are less affected by the wind. The measured frequencies are not affected by the wind and can be used for damage detection.

TABLE 2

Comparison of measured and calculated (from the finite element model) natural frequencies			
Mode #	Measured	FEM	Error %
1	1.17	1.18	-0.8648
2	5.10	5.23	-2.4104
3	7.83	7.89	-0.8418
4	8.17	8.67	-6.1104
5	16.60	16.55	0.31327
6	29.26	30.36	-3.7385
7	45.32	47.85	-5.5831
8	47.75	50.87	-6.5191
9	54.10	55.81	-3.1439
10	67.45	68.83	-2.0476
11	74.70	78.99	-5.7456

[0206] Damage detection was then performed using only the first 4 to 7 measured natural frequencies, as shown in Table 2. The mast is modeled by 40 elements; the lower section has 18 elements, the upper section has 15 elements, and the spike has 7 elements. The experimental damage detection results are shown in **FIG. 23**. The mast is modeled by 40 elements with 20 elements in each of the two sections. It appears that the elements around the joints near the middle of the mast (8.2 m in **FIG. 23**) and at the free end of the mast (13.72 m in **FIG. 23**) had some damage. This is most likely due to the fact that the joints were modeled in the finite element model as being infinitely stiff, which is almost never the case. Also, the spike is actually connected to the free end of the mast at two points. In the finite element model here it is assumed that the spike is attached to the mast along the whole line of contact that has a length of 0.34 m, which makes the model a little stiffer. Similar damage detection results were obtained with different numbers of measured frequencies.

[0207] Simulations for the same lightning mast as shown in **FIG. 22** with different damage scenarios are carried out. Shown in **FIG. 24** are the simulation results for the mast with 70% damage between 0.76 m and 1.15 m from the ground. Shown in **FIG. 25** are the simulation results for the mast with 50% damage between 6.89 m and 7.35 m from the ground. In both cases the location and extent of damage can be relatively accurately detected using the first 5 measured natural frequencies and accurately detected using the first 8 or 10 measured frequencies.

[0208] Methods to Handle Some Ill-Conditioned System Equations

[0209] When the first order perturbation approach is used, one needs to solve in each iteration a system of linear algebraic equations

$$\Delta G = F \quad (47)$$

[0210] which are the linearized equations of (5) and (6), where A is the system matrix, F is the vector representing the differences between the measured and estimated natural frequencies and/or mode shapes, δG is the optimal changes in the stiffness parameters to be found. While the gradient and quasi-Newton methods can be used, the generalized inverse method is most efficient because it does not involve nested iterations, and thus $\delta G = A^*F$, where A^* is the generalized inverse of A . The problem (47) may be ill posed for certain cases, especially in the first several iterations, because A^* can be relatively large and small changes in F can result in large changes in the solution δG . Since the stiffness parameters cannot be negative or greater than the corresponding values of the undamaged structure, the solution may not converge.

[0211] Ill-conditioning problems do not occur in all the examples described above. Sometimes they can occur. Consider, for example, a cantilever aluminum beam of the same dimensions as those of the beam shown in FIG. 12. The beam is divided into 36 elements and assumed to have 30% of damage at the 5th element and 90% of damage at the 18th element. The translational degrees of freedom of the first or second mode shape vector are used to detect damage. The system equations are determinate, and the ill-conditioning problem occurs in the iterations. When a natural frequency is also used in addition to an incomplete eigenvector described above, the ill-conditioning problem can also occur. The following regularization methods can be used to handle the ill-conditioning problem:

[0212] Method 1. Estimate A^* from $(A^T A + \eta I)^{-1} A^T$, where η is a small positive constant that can be searched in several ways. One way is set $\eta = \mu \cdot 1.618 \times \min(10, \| \delta G \|_\infty)$, where $\mu \cdot \mu_\infty$ denotes the infinity norm, with the initial value $\eta = \| A^T A \|_\infty$, until $\| \delta G \|_\infty$ is less than 0.8, for example.

[0213] Method 2. To constrain the magnitude of δG , we include it in the objective function to be minimized. For example, we can minimize the following objective function

$$f(\delta G) = \sum_{i=1}^{N_s} \sum_{j=1}^m (F_i - A_{ij}\delta G_j)^2 + \sum_{j=1}^m (\delta G_j)^2 \quad (48)$$

[0214] instead of (35), where $N_s = n_s + n_w N_m$ is the number of equations in (5) and (6). The optimal solution can be obtained by using the generalized inverse method for the expanded system $A^* \cdot [A; I]$ and the expanded vector $F^* = [F; 0]$, where I is the $m \times m$ identity matrix and 0 is the $m \times 1$ zero vector.

[0215] Note that the solutions from the regularization methods are not strictly the optimal solutions for the original objective function in (35). With accurate and sufficient

measurement information and proper handling of the ill-conditioning problem, the system equations can become well conditioned in the last few iterations and regulation does not need to be applied. Consequently the stiffness parameters can be more accurately determined. Sometimes regulation may over constrain the magnitude of δG , and the termination criterion $\| \delta G \|_\infty < \epsilon$ may be satisfied during the regulation process. In this case, we may set

$$\delta G_i = \frac{3\epsilon \delta G_i}{\| \delta G \|_\infty}$$

[0216] to amplify the magnitude of δG , and the iteration is terminated after the system equations become well conditioned. Since the second regulation method does not need to search for η , it can be more effective when it works. When one carries out the damage detection procedures using different combinations of measured frequencies and mode shapes and obtains the same or similar stiffness parameters, one can have sufficient confidence on the results obtained.

[0217] Using only the translational degrees of freedom of the first eigenvector and the first regulation method, the estimated bending stiffnesses of all the elements of the beam are shown in FIG. 26A. Using the translational degrees of freedom of the second eigenvector and the first regulation method, the estimated bending stiffnesses of all the elements of the beam are shown in FIG. 26B. In both cases the locations of damage are exactly detected and the extent is relatively accurately determined. Using the translational degrees of freedom of the first eigenvector along with the first natural frequency and the first regulation method, the bending stiffnesses of all the elements of the beam are exactly determined, as shown in FIG. 26C.

[0218] Similarly, using the translational degrees of freedom of the first eigenvector and the second regulation method, the estimated bending stiffnesses of all the elements of the beam are shown in FIG. 27A. Using the translational degrees of freedom of the second eigenvector and the second regulation method, the estimated bending stiffnesses of all the elements of the beam are shown in FIG. 27B. In both cases the locations of damage are exactly detected and the extent is relatively accurately determined. Using the translational degrees of freedom of the first eigenvector along with the first natural frequency and the second regulation method, the bending stiffnesses of all the elements of the beam are exactly determined, as shown in FIG. 27C.

[0219] Conclusions

[0220] Thus, the sensitivities of eigenparameters of all orders may, for the first time, be derived using a multiple-parameter, general-order perturbation method. The higher-order solutions may be used to estimate the changes in the eigenparameters with large changes in the stiffness parameters. The perturbation method may be combined with an optimization method to form a robust iterative damage detection algorithm. The gradient and quasi-Newton methods can be used for the first or higher order system equations, and the generalized inverse method can be used efficiently with the first order system equations because it does not involve nested iterations. Including the higher-order perturbations can significantly reduce the number of

iterations when there is a large level of damage. A modified eigenvector expansion method is used to estimate the unmeasured component of the measured mode shape. For many cases, the location(s) and extent of damage can be relatively accurately detected using only measured natural frequencies. Methods to handle ill-conditioned system equations that may occasionally arise are developed and shown to be effective. Numerical simulations on different structures including spring-mass systems, beams, lightning masts, and frames show that with a small number of measured eigenparameters, the stiffness parameters of the damaged system may be accurately identified in all the cases considered. Experiments on the different beam test specimens and the lightning mast in an electric substation validated the theoretical predictions. The methodology can be readily applied to various operation structures of different sizes by incorporating their finite element models or other mathematical models.

[0221] One example of a practical application of this damage detection method is shown in FIG. 28, in which a structure 10 may represent any type of structure that can be modeled by beam elements, on which periodic damage assessment must be conducted. This includes, but is not limited to, structures such as lightning masts, utility poles, cell towers, and other such structures. A structure that can be modeled by beam elements is used simply for ease of discussion, and it is well understood that the general order perturbation method discussed above may be applied to a number of different structural members without departing from the spirit of the invention as embodied and broadly described herein.

[0222] The structure 10 divided into elements E₁ through E_n, and with nodes N₁ through N_n, is equipped with a sensor 40, such as, for example, an accelerometer. The sensor 40 is configured to measure a response to an impact F or a force from a shaker applied to the structure 10. The impact F may be applied in the form of a single impact, as shown in FIG. 28, or it may be in the form of a series of random impacts F₁ through F_n, as shown in FIG. 29. The location on the beam where the impact F is applied may be varied, but the impact F is preferably not applied at one of the nodal points of vibration modes whose natural frequencies and mode shapes need to be measured. In either instance, the sensor 40 senses a response in the structure 10 to the impact F or the force from the shaker, and transmits that response to a processor 20 equipped with, among other elements, the damage detection method 30 discussed above.

[0223] In accordance with the method as described above, upon receipt of the response signal from the sensor 40, the processor 20 accesses and performs the method 30 as previously discussed, and, as the data converges, determines an extent and location, by element, of any structural damage present in the structure 10.

[0224] Although the convergence of the system to resolution is not dependent on where the impact F is applied to the structure 10, a signal to noise ratio of the response may be increased, and an efficiency of the system optimized, as the application point of the impact F is moved away from a fixed point N₀, if one needs to measure the natural frequencies and/or mode shapes of lower modes. Similarly, although the system will converge regardless of the average energy and timing of the impact F or series of impacts F₁-F_n applied

to the structure 10, a signal to noise ratio of the response may be increased, and an efficiency of the system optimized based on a random series of impacts or the random shaker excitation to the structure 10, if the structure is large or slightly nonlinear or if there is an ambient excitation to the structure such as wind.

[0225] The structure 10 may be excited in a number of different manners. For example, an impact F may be applied manually or a shaker may be used, at any given point on the structure 10, excluding the fixed point N₀, or the nodal points of vibration modes whose natural frequencies and/or mode shapes need to be measured. However, in an effort to increase the signal to noise ratio in the signal provided by the sensor 40 to the processor 30 if the structure is large or slightly nonlinear or if there is an ambient excitation to the structure such as wind and to provide the convenience and portability over the shaker test, a series of random impacts F₁-F_n shown in FIG. 29 may be applied manually or by a specially designed device to generate the impact F. Although accurate and reliable damage assessments can be achieved regardless of how the impact F is applied to the structure 10, results may be improved using a random series impact method, which involves using a series of impacts F of random amplitudes and random arrival times. A series of random impacts has been shown to increase an energy input to the structure 10, improve the signal to noise ratio, especially in such situations as strong wind excitation, and average out slight nonlinearities that arise, for example, from bolted joints and extract linearized eigenparameters.

[0226] FIG. 29 illustrates a structure 10, sensor 40 and processor 20 similar to those shown in FIG. 28. An impact F in FIG. 29 is applied to the structure 10, at a location other than N₀ or one of the nodal points of vibration modes whose natural frequencies and/or mode shapes need to be measured, as a series of random impacts F₁ through F_n delivered at random amplitude and arrival time. These random impacts F₁-F_n may be delivered manually, or, as shown in FIG. 30, may be delivered in an automated fashion through the use of a random impact hammer device 1550.

[0227] Different methods have been employed in conventional vibration testing in order to excite a test specimen. Shaker testing, in which a specimen is, simplistically, shaken in order to impart a high level of energy, can produce a high signal to noise ratio, and can induce random excitation, which can average out slight nonlinearities and extract linearized eigenparameter parameters. However, shaker testing is not practically employed in the field on relatively large structures, and can be cost prohibitive to conduct. Single impact hammer testing addresses the shortfalls of shaker testing, in that it is portable and inexpensive to conduct. However, single impact hammer testing falls short where shaker testing is strong, in that low energy input of single impact hammer testing produces a low energy input, a low signal to noise ratio with no randomization. To address the need for a system which combines the advantages of shaker testing and single impact hammer testing, a Random Impact Series method for hammer testing is presented which yields a high energy, high signal to noise ratio, random system. A novel stochastic model is developed to simulate the random impact series produced manually and to generate a random impact series for a specially designed random impact device.

[0228] FIG. 31 shows a random impact device 1550, according to one embodiment of the invention. Random

impact device 1550 includes random signal generating unit 1560 and a random impact actuator 1570 with impact applicator 1580. The impact applicator 1580 preferably includes a sensor 1581, such as a force transducer, attached at its tip. Sensor 1581 is preferably configured to send data to the spectrum analyzer in stiffness parameter unit 103 in order to obtain mode shape information, as discussed above in connection with FIG. 1A. Sensor 1581 can be coupled to the spectrum analyzer in any manner known in the art including, but not limited to, wire, optical fiber or even a wireless connection. Random impact signal generating unit 1560 generates outputs 1590 and 1591 to random impact actuator 1570. It should be appreciated that outputs 1590 and 1591 could be coupled to the random impact actuator 1570 in any manner known in the art including, but not limited to, cables, wires, optical fibers, wireless communications, and so forth.

[0229] Output 1590 corresponds to the amplitude ψ_p , as discussed below. In particular, random signal generating unit 1560 outputs a value corresponding to ψ_p , as discussed below. Output 1591 corresponds to τ_i , as discussed below.

[0230] Impact applicator 1580 is shown, for purposes of illustration, as impacting structure 1600 in a reciprocating motion. Impact applicator 1580 is shown to have an impact path 1610, such that when a structure 1600 lies within the impact region 1610, impact applicator 1580 impacts structure 1600 with a force of random amplitude that arrives at a random time, as discussed below. The impact applicator 1580 and impact region 1610 as shown in FIG. 31 is one possible embodiment, and other shapes and impact regions may be used while still falling within the scope of the present invention.

[0231] Although random signal generating unit 1560 is shown to output two outputs 1590 and 1591 that correspond to ψ_p and τ_i below, it should be understood that signal generating unit 1590 could output any signal or signals that ultimately results in random impact actuator 1570 driving impact applicator 1580 to impact structure 1600 with random arrival times τ_i and random amplitudes ψ_p .

[0232] As discussed above, vibration information is obtained by sensor 110, and is sent to stiffness parameter unit 103 via sensor coupler 113. The stiffness parameter unit 103 sends stiffness parameters to the damage information processor 123. While the random impact device can be used for damage detection purposes as discussed above, it can certainly be used just for obtaining the natural frequencies and/or mode shapes of the structure for modal testing purposes.

[0233] Experiments conducted on lightning masts by the applicant confirm that multiple impact testing performs better than single impact testing when there is wind excitation to the masts. Results are shown for a 65 foot tall mast with a 5 foot spike, as shown in FIG. 32, referred to hereinafter simply as a seventy foot tall mast. The mast has two constant cross section schedule 40 pipes of equal length. It can be seen from the results shown in FIGS. 33A-33B that the multiple impact test has much better coherence, is less noisy away from the resonances, and can pick up the modes that were missing in the single impact test. The multiple impact test is better at exciting the lower modes that can also be excited by the wind, which can be seen by comparing the frequency response functions (FRF) between 0 and 30 Hz.

It can been seen from the FRF for the multiple impact tests that there are some modes that are missed at near 4 Hz and 7 Hz with the single impact test, and the mode at 10 Hz is much improved compared to the single impact test.

[0234] A stochastic model will now be discussed which describes the random impact series $F_i \cdot F_n$, modeled as a Poisson process. The Poisson process is one of a general class of processes that arises in problems concerning the counting of events in the course of time. The force pulses in the series are assumed to have an arbitrary, deterministic shape function and random amplitudes and arrival times. The force signal in a finite time interval is shown to consist of wide sense stationary and non-stationary parts. The expectations of the average power densities associated with the entire force signal and the stationary part of the signal are derived and compared, and the power spectral density is related to the average power density and the autocorrelation function associated with the stationary part of the force signal. Numerical simulation is conducted to validate analytical predictions, and a relationship between the Fourier transform and the discrete Fourier transform used in a numerical simulation is produced. Experiments on the four bay space frame, as shown in FIG. 10, validated the distributions of the random variables and the Poisson process.

[0235] Stochastic Model of a Random Impact Series

[0236] A random impact series is modeled here as a sum of force pulses with the same shape and random amplitudes and arrival times:

$$x(t) = \sum_{i=1}^{N(t)} \psi_i y(t - \tau_i) \quad t \in (0, \infty) \quad (49)$$

[0237] where t is time, $x(t)$ is the time function of the force signal, $\tau_i \in (0, t]$ is the random arrival time of the i -th pulse, and $y(t - \tau_i)$ is the deterministic shape function for all the pulses, ψ_i is the random variable describing the amplitude of the i -th pulse, and $N(t)$ is the number of the pulses that have arrived during the time interval $(0, t]$ and is modeled as a Poisson process with stationary increments. All the pulses are assumed to be of width Δt , and $y(t - \tau_i)$ satisfies $y(t - \tau_i) = 0$ if $t < \tau_i$ and $t > \tau_i + \Delta t$.

[0238] Since a finite time record is used for the force signal in modal testing, we consider only the pulses that arrive during the time interval $(0, T]$ of length T , as shown in FIG. 34. Note that $y(0)$ and $y(\Delta t)$ do not have to be equal to zero in this model. Because the pulses arriving after time t ($t < T$) will not affect the force signal at time t , the random process $N(t)$ in (49) can be replaced by $N(T)$. Also, if a pulse arrives at time T , it will vanish at time $T + \Delta t$. The last pulse in FIG. 34 arrives at time T_{NT} and ends at a time between T and $T + \Delta t$. To include completely this last possible pulse, we consider the time interval $t \in (0, T + \Delta t)$. Equation (49) is rewritten as

$$x(t) = \sum_{i=1}^{N(T)} \psi_i y(t - \tau_i), \quad \tau_i \in (0, T] \text{ and } t \in (0, T + \Delta\tau] \quad (50)$$

[0239] For the Poisson process $N(t)$ with stationary increments, the probability of the event $\{N(t)=n\}$, where n is an integer, is

$$P_{N(t)}(n, t) = \frac{e^{-\lambda t} (\lambda t)^n}{n!},$$

[0240] where λ is the constant arrival rate of the pulses. By replacing t with T , the probability of the event $\{N(T)=n\}$ is

$$P_{N(T)}(n, T) = \frac{e^{-\lambda T} (\lambda T)^n}{n!} \quad (51)$$

[0241] All the arrival times τ_i , where $i=1,2,3,\dots,N(T)$, are identically distributed, mutually independent random variables. Because the arrival rate of the pulses is constant, the arrival times τ_i are uniformly distributed in $[0, T]$ with the probability density function

$$P_{\tau_i}(t) = \begin{cases} \frac{1}{T}, & 0 \leq t \leq T \\ 0, & \text{elsewhere} \end{cases} \quad (52)$$

[0242] Similarly, ψ_i ($i=1,2,\dots,N(T)$) are identically distributed random variables, which are mutually independent and independent of the distribution of the arrival times τ_i . While the distribution of ψ_i ($i=1,2,\dots,N(T)$) is not used in the subsequent derivation, it is assumed that ψ_i satisfy the Gaussian distribution with the probability density function

$$\rho_{\psi_i}(\psi) = \frac{1}{\sqrt{2\pi}\sigma} e^{-\frac{(\psi-\mu)^2}{2\sigma^2}}, \quad 0 < \psi < \infty \quad (53)$$

[0243] where $\mu=\mathbb{E}[\psi_i]$ is the mean and $\sigma^2=\mathbb{E}[\psi_i^2]-\mathbb{E}^2[\psi_i]$ is the variance of ψ_i . While the distribution in (53) is not used in the analytical derivations, it is used in the numerical simulation and validated experimentally for a manually applied random impacts on a four bay space frame, as shown in FIG. 10.

[0244] Force Spectrum and its Expectation

[0245] The force spectrum is the Fourier transform of the force signal in (50):

$$X(j\omega) = F[x(t)] = \sum_{i=1}^n \psi_i e^{-j\omega\tau_i} \quad (54)$$

$$\int_{-\infty}^{\infty} \left\{ \sum_{i=1}^n \psi_i y(t - \tau_i) \right\} e^{-j\omega t} dt = \sum_{i=1}^{N(T)} \psi_i \int_{\tau_i}^{\tau_i + \Delta\tau} y(t - \tau_i) e^{-j\omega t} dt$$

-continued

$$X(j\omega) = \sum_{i=1}^{N(T)} \psi_i e^{-j\omega\tau_i} \int_0^{\Delta\tau} y(u) e^{-j\omega u} du \quad (55)$$

[0246] where F denotes Fourier transform, $X(j\omega)$ is the Fourier transform of $x(t)$, ω is the angular frequency, and $j=\sqrt{-1}$. Let $u=t-\tau_i$, then $t=u+\tau_i$ and $dt=du$. Equation (54) becomes

$$E[X(j\omega)] = E \left[\sum_{i=1}^{N(T)} \psi_i e^{-j\omega\tau_i} \int_0^{\Delta\tau} y(u) e^{-j\omega u} du \right] \quad (56)$$

[0247] Since the integral in (55) is a deterministic function, the expectation of the force spectrum is

$$\begin{aligned} E[X(j\omega)] &= E \left[\sum_{i=1}^{N(T)} \psi_i e^{-j\omega\tau_i} \right] \int_0^{\Delta\tau} y(u) e^{-j\omega u} du \\ &= \sum_{n=0}^{\infty} P_{N(T)}(n, T) \sum_{i=1}^{N(T)} \psi_i e^{-j\omega\tau_i} \int_0^{\Delta\tau} y(u) e^{-j\omega u} du \end{aligned} \quad (57)$$

[0249] we have from (56)

$$E[X(j\omega)] = E \left[\sum_{i=1}^{N(T)} \psi_i e^{-j\omega\tau_i} \right] N(T) \int_0^{\Delta\tau} y(u) e^{-j\omega u} du \quad (58)$$

[0250] Since $\psi_i e^{-j\omega\tau_i}$ ($i=1,2,\dots,n$) are independent of each other and ψ_i is independent of $e^{-j\omega\tau_i}$, we have

$$E \left[\sum_{i=1}^n \psi_i e^{-j\omega\tau_i} \right] = \sum_{i=1}^n E[\psi_i e^{-j\omega\tau_i}] = \sum_{i=1}^n E[\psi_i] E[e^{-j\omega\tau_i}] \quad (58)$$

[0251] Since ψ_i ($i=1,2,\dots,n$) are identically distributed random variables and so are τ_i ($i=1,2,\dots,n$), we have from (58)

$$E \left[\sum_{i=1}^n \psi_i e^{-j\omega\tau_i} \right] = n E[\psi_1] E[e^{-j\omega\tau_1}] \quad (59)$$

[0252] Substituting (59) into (57) yields

$$E[X(j\omega)] = \sum_{n=0}^{\infty} P_{1|1}(n, T)nE[\phi_1] \left[\int_{-\infty}^{\infty} e^{-j\omega\tau} p_{11}(\tau) d\tau \right] \int_0^{\Delta\tau} y(u)e^{-j\omega u} du \quad (60)$$

[0253] Substituting (51) and (52) into (60) yields

$$\begin{aligned} E[X(j\omega)] &= \sum_{n=0}^{\infty} \left[\frac{(\lambda T)^n e^{-j\lambda T}}{n!} nE[\phi_1] \left[\int_0^T \left(\frac{1}{T} \right) e^{-j\omega\tau} d\tau \right] \right. \\ &\quad \left. \int_0^{\Delta\tau} y(u)e^{-j\omega u} du \right] \\ &= \sum_{n=1}^{\infty} \frac{(\lambda T)^{n-1} e^{-j\lambda T}}{(n-1)!} (\lambda T)E[\phi_1] \left\{ \frac{e^{-j\omega T} - 1}{-j\omega T} \right\} \\ &\quad \int_0^{\Delta\tau} y(u)e^{-j\omega u} du \\ &= \frac{\lambda E[\phi_1] (1 - e^{-j\omega T})}{j\omega} \int_0^{\Delta\tau} y(u)e^{-j\omega u} du \end{aligned} \quad (61)$$

[0254] where Taylor expansion of $e^{j\lambda T}$ has been used.

[0255] Average Power Density of $x(t)$ in $[0, T + \Delta\tau]$ and its Expectation

[0256] The average power density of the force signal in (50) is defined as

$$S_1(\omega) = \frac{X(j\omega)X^*(j\omega)}{T + \Delta\tau} \quad (62)$$

[0257] where $X^*(j\omega)$ is the complex conjugate of $X(j\omega)$:

$$X^*(j\omega) = \sum_{n=1}^{N(T)} \psi_n e^{jn\omega T} \int_0^{\Delta\tau} y(u)e^{jn\omega u} du \quad (63)$$

[0258] Substituting (55) and (53) into (62) yields

$$\begin{aligned} S_1(\omega) &= \frac{\sum_{n=1}^{N(T)} \psi_n e^{-j\omega T} n \int_0^{\Delta\tau} y(u)e^{-j\omega u} du}{T + \Delta\tau} \\ &\quad + \sum_{n=1}^{N(T)} \psi_n e^{j\omega T} \int_0^{\Delta\tau} y(v)e^{j\omega v} dv \end{aligned} \quad (64)$$

$$\begin{aligned} &= \frac{\left(\int_0^{\Delta\tau} \int_0^{\Delta\tau} y(u)y(v)e^{-j\omega(u-v)} du dv \right)}{T + \Delta\tau} \\ &\quad + \sum_{n=1}^{N(T)} \sum_{m=1}^{N(T)} \psi_n \bar{\psi}_m e^{j\omega(\tau_i - \tau_m)} \end{aligned}$$

[0259] Let $k=u-v$, then $u=k+v$ and $du=dk$. The double integral in (64) becomes

$$\begin{aligned} &\int_{-\Delta\tau}^{\Delta\tau} \int_0^{\Delta\tau} y(u)y(v)e^{-j\omega(u-v)} du dv = \\ &\quad \int_0^{\Delta\tau} dv \int_{-v}^0 y(v+k)y(v)e^{-jk\omega} dk + \\ &\quad \int_0^{\Delta\tau} dv \int_0^{v-\Delta\tau} y(v+k)y(v)e^{-jk\omega} dk \end{aligned} \quad (65)$$

[0260] Interchanging the order of integration in (65) yields

$$\begin{aligned} &\int_0^{\Delta\tau} \int_0^{\Delta\tau} y(u)y(v)e^{-j\omega(u-v)} du dv = \\ &\quad \int_{-k}^0 dk \int_{-k}^{\Delta\tau} y(v+k)y(v)e^{-jk\omega} dv + \\ &\quad \int_0^{\Delta\tau} dk \int_0^{\Delta\tau-k} y(v+k)y(v)e^{-jk\omega} dv \end{aligned} \quad (66)$$

[0261] Let $v+k=\gamma$, then $v=\gamma-k$ and $dv=d\gamma$. The first integral on the right-hand side of (66) becomes

$$\begin{aligned} &\int_{-k}^0 dk \int_{-k}^{\Delta\tau} y(v+k)y(v)e^{-jk\omega} dv = \\ &\quad \int_{-k}^0 dk \int_0^{\Delta\tau+k} y(\gamma)y(\gamma-k)e^{-jk\omega} d\gamma \end{aligned} \quad (67)$$

[0262] Changing γ in (67) back to v and substituting the resulting expression into (66) yields

$$\begin{aligned} &\int_0^{\Delta\tau} \int_0^{\Delta\tau} y(u)y(v)e^{-j\omega(u-v)} du dv = \\ &\quad \int_{-k}^0 \int_{-k}^{\Delta\tau-k} y(v+k)y(v)e^{-jk\omega} dk \end{aligned} \quad (68)$$

[0263] Noting that

$$\int_0^{\Delta\tau-k} y(v+k)y(v) dv$$

[0264] is an even function of k , we have

$$\begin{aligned} &\int_0^{\Delta\tau-k} y(v+k)y(v) dv = \\ &\quad - \int_0^{\Delta\tau-k} y(v+\lvert k \rvert)y(v)\cos(\omega k) dk \end{aligned} \quad (69)$$

[0265] Substituting (69) into (68) and substituting the resulting expression into (64) yields

$$S_1(\omega) = \frac{1}{T + \Delta\tau} \left(\int_{-\Delta\tau}^{\Delta\tau} \int_0^{|\Delta\tau - |\tau|} y(v + |k|) y(v) d\tau v \cos(\omega k) dk \right) \quad (70)$$

$$\sum_{m=1}^{N(T)N(T)} \psi_m \psi_i e^{\lambda i (vT - \tau_m)}$$

[0266] Since the double integral in (70) is deterministic, we have

$$E[S_1(\omega)] = \frac{1}{T + \Delta\tau} \left(\int_{-\Delta\tau}^{\Delta\tau} \int_0^{|\Delta\tau - |\tau|} y(v + |k|) y(v) d\tau v \cos(\omega k) dk \right) \quad (71)$$

$$E \left[\sum_{m=1}^{N(T)N(T)} \psi_m \psi_i e^{\lambda i (vT - \tau_m)} \right]$$

[0267] Since

$$E \left(\sum_{m=1}^{N(T)N(T)} \psi_m \psi_i \sin[j\omega(\tau_i - \tau_m)] \right) = 0, \quad \psi_i (i = 1, 2, \dots, N(T))$$

[0268] are identically distributed random variables, and so are τ_i ($i = 1, 2, \dots, N(T)$), we have

$$E \left[\sum_{m=1}^{N(T)N(T)} \psi_m \psi_i e^{\lambda i (vT - \tau_m)} \right] = E \left[\sum_{m=1}^{N(T)N(T)} \psi_m \psi_i \cos(j\omega(\tau_i - \tau_m)) \right] = \quad (72)$$

$$E \left[\sum_{j=1}^{N(T)} \psi_j^2 + \sum_{m=1}^{N(T)N(T)} \psi_m \psi_i \cos(j\omega(\tau_i - \tau_m)) \right] \\ E[N(T)\psi_i^2 + [N^2(T) - N(T)]\psi_i^2 \cos(\tau_1 - \tau_2)]$$

[0269] Since τ_1 and τ_2 are independently, uniformly distributed random variables in $[0, T]$, the probability density function of $\tau_1 - \tau_2$ is

$$p_{\tau_1 - \tau_2}(r) = \begin{cases} \frac{T - |\lambda|r}{T^2}, & -T \leq r \leq T \\ 0, & \text{elsewhere} \end{cases} \quad (73)$$

[0270] Using (51) and (73) in (72) yields

$$E \left[\sum_{m=1}^{N(T)N(T)} \psi_m \psi_i e^{\lambda i (vT - \tau_m)} \right] = \sum_{k=0}^{\infty} P_{1|1}(n, T) n E[\psi_1^2] + \quad (74)$$

$$\sum_{k=0}^{\infty} P_{1|1}(n, T) (n^2 - n) E[\psi_1^2]$$

-continued

$$\int_{-\infty}^{\infty} \cos(\omega t) p_{\tau_1 - \tau_2}(\tau) d\tau \\ = \lambda T E[\psi_1^2] + 2\lambda^2 E^2[\psi_1] \frac{1 - \cos(\omega T)}{\omega^2}$$

[0271] Substituting (74) into (71) yields

$$E[S_1(\omega)] = \frac{1}{T + \Delta\tau} \left(\int_{-\Delta\tau}^{\Delta\tau} \int_0^{|\Delta\tau - |\tau|} y(v + |k|) y(v) d\tau v \cos(\omega k) dk \right) \times \quad (75)$$

$$\left(2\lambda^2 E^2[\psi_1] \frac{1 - \cos(\omega T)}{\omega^2} + \lambda T E[\psi_1^2] \right)$$

[0272] Mean and Autocorrelation Functions of x(t)

[0273] The first-order cumulant function of $x(t)$ in (50), $\kappa_1[x(t)]$, is equal to its mean function, $E[x(t)]$. The second-order cumulant function of $x(t)$, $\kappa_2[x(t_1)x(t_2)]$, is related to its autocorrelation function, $E[x(t_1)x(t_2)]$ through

$$E[x(t_1)x(t_2)] = \kappa_2[x(t_1)x(t_2)] + \kappa_1[x(t_1)]\kappa_1[x(t_2)] \quad (76)$$

[0274] where t_1 and t_2 are any two time instants in $[0, T + \Delta\tau]$. Following the derivations, the first- and second-order cumulant functions of $x(t)$ are

$$\kappa_1[x(t)] = E[x(t)] = E[\psi_1] = \int_0^T y(u) du \quad (77)$$

$$\kappa_2[x(t_1)x(t_2)] = E[\kappa_{xx}(t_1, t_2)] = E[\psi_1^2] = \int_{t_1 - T}^{t_2} y(u) du \quad (78)$$

[0275] where $t \in [0, T + \Delta\tau]$. Let $t - \alpha = u$ in (75), then $du = du$. We have from (77)

$$E[x(t)] = \lambda E[\psi_1] = \int_{t-T}^t y(u) du \quad (79)$$

[0276] Let

$$W(t) = \int_0^t y(u) du \quad (80)$$

[0277] Noting that $y(u) = 0$ when $u < 0$ and $u > \Delta\tau$, we have from (79)

$$E[x(t)] = \begin{cases} \lambda E[\psi_1] W(t), & 0 < t < \Delta\tau \\ \lambda E[\psi_1] W(\Delta\tau), & \Delta\tau \leq t \leq T \\ \lambda E[\psi_1] [W(\Delta\tau) - W(t - T)], & T < t \leq T + \Delta\tau \end{cases} \quad (81)$$

[0278] where $T > \Delta\tau$ is assumed. Let $t_1 - \alpha = u$ and $t_2 - t_1 - k$ in (78), then $dt_1 = du$ and $t_2 - \alpha = u + k$. We have from (78)

$$\kappa_{xx}(t_1, t_2) = \lambda E[\psi_1^2] \int_{t_1 - T}^{t_2} y(u) y(u + k) du \quad (82)$$

[0279] When $|k| > \Delta\tau$, $y(u)y(u+k) = 0$ and hence $\kappa_{xy}(t_1, t_2) = 0$. When $0 \leq k \leq \Delta\tau$, we have from (82) for different t_1

$$\kappa_{xy}(t_1, t_2) = \begin{cases} \lambda E[\psi_1^2] \int_0^{t_1} y(u)y(u+k)du, & 0 \leq t_1 < \Delta\tau - k \\ \lambda E[\psi_1^2] \int_0^{\Delta\tau-k} y(u)y(u+k)du, & \Delta\tau - k \leq t_1 \leq T \\ \lambda E[\psi_1^2] \int_{t_1-T}^{\Delta\tau} y(u)y(u+k)du, & T < t_1 \leq T + \Delta\tau \\ 0, & T + \Delta\tau - k < t_1 \leq T + \Delta\tau \end{cases} \quad (83)$$

[0280] When $-\Delta\tau \leq k < 0$, we have from (82) for different t_1

$$\kappa_{xy}(t_1, t_2) = \begin{cases} \lambda E[\psi_1^2] \int_{-k}^{t_1} y(u)y(u+k)du, & -k \leq t_1 < \Delta\tau \\ \lambda E[\psi_1^2] \int_{-k}^{\Delta\tau} y(u)y(u+k)du, & \Delta\tau \leq t_1 \leq T - k \\ \lambda E[\psi_1^2] \int_{t_1-T}^{-k} y(u)y(u+k)du, & T - k < t_1 \leq T + \Delta\tau \\ 0, & 0 \leq t_1 < -k \end{cases} \quad (84)$$

[0281] Let $u+k=v$ in (84), then $u=v-k$ and $du=dv$. We have from (84) after changing v back to u

$$\kappa_{xy}(t_1, t_2) = \begin{cases} \lambda E[\psi_1^2] \int_0^{t_1+k} y(u-k)y(u)du, & -k \leq t_1 < \Delta\tau \\ \lambda E[\psi_1^2] \int_0^{\Delta\tau+k} y(u-k)y(u)du, & \Delta\tau \leq t_1 \leq T - k \\ \lambda E[\psi_1^2] \int_{t_1-T}^{-k} y(u-k)y(u)du, & T - k < t_1 \leq T + \Delta\tau \\ 0, & 0 \leq t_1 < -k \end{cases} \quad (85)$$

[0282] Combining the second equations in (83) and (85), we have for t_1 and t_2 in $[\Delta\tau, T]$

$$\kappa_{xy}(t_1, t_2) = \lambda E[\psi_1^2] \int_0^{\Delta\tau-|k|} y(u)y(u+|k|)du \quad (86)$$

[0283] Since by the second equation in Eq. (81), $E[x(t)]$ is a constant for $t \in [\Delta\tau, T]$, and by (86), $\kappa_{xy}(t_1, t_2)$ is a function of $k = t_2 - t_1$ for t_1 and t_2 in $[\Delta\tau, T]$, $x(t)$ is a wide-sense stationary random process in $[\Delta\tau, T]$. Substituting the second equation in (81) and (86) into (76) yields the autocorrelation function for t_1 and t_2 in $[\Delta\tau, T]$

$$R_{xy}(k) \triangleq E[x(t_1)x(t_2)] = \begin{cases} \lambda E[\psi_1^2] \int_0^{\Delta\tau-|k|} y(u)y(u+|k|)du + \lambda^2 E^2[\psi_1] W^2(\Delta\tau) & k = t_2 - t_1 \\ 0, & k \neq t_2 - t_1 \end{cases} \quad (87)$$

[0284] Fourier Transform of the Mean Function of $x(t)$ and its Equivalence to $E[X(j\omega)]$

[0285] Applying the Fourier transform to $E[x(t)]$ in Eq. (81) yields

$$F[E[x(t)]] = \lambda E[\psi_1] \left\{ \int_0^{\Delta\tau} W(t)e^{-j\omega t} dt + \int_{\Delta\tau}^T W(\Delta\tau)e^{-j\omega t} dt + \int_T^{T+\Delta\tau} [W(\Delta\tau) - W(t-\tau)]e^{-j\omega t} dt \right\} \quad (88)$$

[0286] The three integrals in (88) are referred to as I_1 , I_2 , and I_3 , respectively. Consider first the third integral in (88)

$$I_3 \int_T^{T+\Delta\tau} [W(\Delta\tau) - W(t-\tau)]e^{-j\omega t} dt \quad (89)$$

[0287] Let $t - \Delta\tau = 0$ in (88), then $t = T + \Delta\tau$ and $dt = d0$. We have from Eq. (89)

$$I_3 = e^{-j\omega\Delta\tau} \int_0^{\Delta\tau} e^{j\omega 0} W(\Delta\tau)e^{-j\omega 0} d0 - e^{-j\omega\Delta\tau} \int_0^{\Delta\tau} e^{j\omega 0} W(0)e^{-j\omega 0} d0 \quad (90)$$

[0288] Changing 0 in (90) back to t and combining I_1 and I_3 yields

$$I_1 + I_3 = e^{-j\omega\Delta\tau} \int_0^{\Delta\tau} W(\Delta\tau)e^{-j\omega t} dt + (1 - e^{-j\omega\Delta\tau}) \int_0^{\Delta\tau} W(0)e^{-j\omega t} dt \quad (91)$$

[0289] Adding I_2 to (91), simplifying the expression, and substituting it into (88) yields

$$\begin{aligned} F[E[x(t)]] &= \lambda E[\psi_1] \left[(1 - e^{-j\omega\Delta\tau}) \int_0^{\Delta\tau} W(t)e^{-j\omega t} dt + e^{-j\omega\Delta\tau} \int_0^{\Delta\tau} W(\Delta\tau)e^{-j\omega t} dt \right] = \lambda E[\psi_1] \\ &\quad (1 - e^{-j\omega\Delta\tau}) W(\Delta\tau) \left[\frac{1}{j\omega} + \int_0^{\Delta\tau} \left(\frac{W(t)}{W(\Delta\tau)} - 1 \right) e^{-j\omega t} dt \right] \end{aligned} \quad (92)$$

[0290] We will show that $F[E[x(t)]]$ in (92) is equivalent to $E[X(j\omega)]$ in (91). By (80), we have

$$W(t) = \begin{cases} 0, & t \in (-\infty, 0) \\ \int_0^t I_1(\tau)d\tau, & t \in [0, \Delta\tau] \\ W(\Delta\tau), & t \in (\Delta\tau, \infty) \end{cases} \quad (93)$$

[0291] The integral in (61) can be written as

$$\begin{aligned} \int_0^{\Delta\tau} y(u)e^{-j\omega u} du &= \int_0^{\Delta\tau} y(u)du + \int_0^{\Delta\tau} y(u)(e^{-j\omega u} - 1)du \\ &= \int_0^{\Delta\tau} y(u)du - j\omega \int_0^{\Delta\tau} y(u) \int_0^u v e^{-j\omega v} dv du \end{aligned}$$

[0292] Interchanging the order of integration in the double integral in (94) and using (93) yields

$$\begin{aligned} \int_0^{\Delta T} y(u)e^{-ju\omega} du &= \\ \int_0^{\Delta T} y(u)du - j\omega \int_0^{\Delta T} dy &\int_0^{\Delta T} y(u)e^{-ju\omega} du \\ &= W(\Delta\tau) \left\{ 1 + j\omega \int_0^{\Delta T} \left[\frac{W(v)}{W(\Delta\tau)} - 1 \right] e^{-ju\omega} dv \right\} \end{aligned} \quad (95)$$

[0293] Substituting (95) into (61) yields (91). This shows that the expectation E and the Fourier transform F are commutative as both are linear operators.

[0294] Equation (92) consists of two parts: the first part,

$$\lambda E[\psi_1](1 - e^{-j\omega\tau})W(\Delta\tau) \frac{1}{j\omega},$$

[0295] is the Fourier transform of the stationary part of $E[x(i)]$ in $[\Delta\tau, T]$, and the second part,

$$\lambda E[\psi_1](1 - e^{-j\omega\tau})W(\Delta\tau) \int_0^{\Delta T} \left(\frac{W(t)}{W(\Delta\tau)} - 1 \right) e^{-jt\omega} dt,$$

[0296] is the sum of the Fourier transforms of the nonstationary parts of $E[x(i)]$ in $[0, \Delta\tau]$ and $[T, T+\Delta\tau]$. When $\Delta\tau \rightarrow 0$, since

[0297] is finite,

$$\int_0^{\Delta T} \left(\frac{W(t)}{W(\Delta\tau)} - 1 \right) e^{-jt\omega} dt,$$

[0298] and consequently the second part of $E[X(j\omega)]$, approaches zero.

[0299] Average Power Density of $x(i)$ in $[\Delta\tau, T]$, Its Expectation, and Power Spectral Density

[0300] Since $x(i)$ is stationary in $[\Delta\tau, T]$, the average power density of $x(i)$ in $[\Delta\tau, T]$ is defined as

$$S_x(\omega) = \frac{X_x(j\omega)X_x^*(j\omega)}{T - \Delta\tau} \quad (96)$$

[0301] where $X_x(j\omega) = \int_{\Delta\tau}^T x(t)e^{-j\omega t} dt$. Taking the expectation of (96) yields

$$E[S_x(\omega)] = \frac{1}{T - \Delta\tau} \int_{\Delta\tau}^T \int_{\Delta\tau}^T E[x(t_1)x(t_2)]e^{-j\omega(t_1-t_2)} dt_1 dt_2 \quad (97)$$

[0302] Let $k=t_2-t_1$ in (97), then $dk=dt_2$. Since $E[x(t_1)x(t_2)] = R_{xx}(k)$, (97) becomes after interchanging the order of integration

$$\begin{aligned} E[S_x(\omega)] &= \frac{1}{T - \Delta\tau} \int_{\Delta\tau}^T dt_1 \int_{t_1-\Delta\tau}^{T-t_1} R_{xx}(k)e^{jk\omega} dk \\ &= \int_{-(T-\Delta\tau)}^{T-\Delta\tau} R_{xx}(k) \left(1 - \frac{|k|}{T - \Delta\tau} \right) e^{jk\omega} dk \end{aligned} \quad (98)$$

[0303] Substituting (87) into (98) yields

$$\begin{aligned} E[S_x(\omega)] &= \lambda E[\psi_1^2] \\ &\quad \int_{-(T-\Delta\tau)}^{T-\Delta\tau} \int_0^{\Delta T-|k|} y(u+|k|)y(u)du \left(1 - \frac{|k|}{T - \Delta\tau} \right) e^{jk\omega} dk + \\ &\quad 2\lambda^2 E^2[\psi_1]W^2(\Delta\tau) \int_{-(T-\Delta\tau)}^{T-\Delta\tau} \left(1 - \frac{|k|}{T - \Delta\tau} \right) e^{jk\omega} dk \end{aligned} \quad (99)$$

[0304] Noting that $y(u)y(u+|k|)=0$ when $|k|>\Delta\tau$ and

$$\int_0^{\Delta T-|k|} y(u+|k|)y(u)du \left(1 - \frac{|k|}{T - \Delta\tau} \right)$$

[0305] an even function of $|k|$, we have from (99)

$$\begin{aligned} E[S_x(\omega)] &\approx 2\lambda^2 E^2[\psi_1]W^2(\Delta\tau) \frac{1 - \cos\omega(T - \Delta\tau)}{\omega^2(T - \Delta\tau)} + \lambda E[\psi_1^2] \\ &\quad \int_{-\Delta\tau}^{\Delta\tau} \int_0^{\Delta T-|k|} y(u+|k|)y(u)du \left(1 - \frac{|k|}{T - \Delta\tau} \right) \cos\omega k dk \end{aligned} \quad (100)$$

[0306] where $T>2\Delta\tau$ has been assumed.

[0307] The power spectral density of $x(t)$ can be obtained from (100) by increasing T to infinity

$$S_x(\omega) = \lim_{T \rightarrow \infty} S_x(\omega) = 2\pi\lambda^2 E^2[\psi_1]W^2(\Delta\tau)\delta(\omega) + \quad (101)$$

$$\lambda E[\psi_1^2] \int_{-\Delta\tau}^{\Delta\tau} \int_0^{\Delta T-|k|} I(u+|k|)I(u)\cos(\omega u)dk$$

[0308] where we have used

$$\lim_{T \rightarrow \infty} \frac{1 - \cos\omega(T - \Delta\tau)}{\omega^2(T - \Delta\tau)} = \lim_{T \rightarrow \infty} \frac{2\sin^2 \frac{\omega(T - \Delta\tau)}{2}}{\pi\omega^2(T - \Delta\tau)} = \delta(\omega) \quad (102)$$

[0309] in which $\delta(\mathbb{C})$ is the Dirac delta function. The power spectral density can also be obtained from (98) by increasing T to infinity

$$\lim_{\Delta\tau \rightarrow 0} \frac{\langle S_1(\omega) \rangle}{R_{S_1}(k)} = \lim_{\Delta\tau \rightarrow 0} \frac{\langle E[S_1(\omega)] \rangle}{\int_{-\infty}^{\infty} dk / R_{S_1}(k)} = \lim_{\Delta\tau \rightarrow 0} \frac{\langle R_{S_1}(k) e^{ik\Delta\tau} \rangle}{\int_{-\infty}^{\infty} dk / R_{S_1}(k)} \quad (103)$$

[0310] where $R_{S_1}(-k) = R_{S_1}(k)$ has been used. Equation (103) is the well-known Wiener-Khintchine theorem, which states the power spectral density is the Fourier transform of the autocorrelation function. Substituting (87) into (83), and noting that $I(u)I(u+|\mathbb{C}|) = 0$ when $|k| > \Delta\tau$ and the Fourier transform of 1 is $2\pi\delta(\omega)$, yields (101). Note that the power spectral density is only defined for a wide-sense stationary process with an infinite time record. When the mean amplitude of each pulse $E[\psi_1]$ is not equal to zero, there is an associated delta function in the power spectral density.

[0311] Comparison of $E[S_1(\omega)]$ and $E[S_2(\omega)]$

[0312] By (100), $E[S_2(\omega)]$ consists of two parts: the first part,

$$2\lambda^2 E^2[\psi_1] W^2(\Delta\tau) \frac{1 - \cos\omega(T - \Delta\tau)}{\omega^2(T - \Delta\tau)},$$

[0313] which depends on the arrival rate λ , the mean amplitude of each pulse $E[\psi_1]$, the total area of the normalized shape function $W(\Delta\tau)$, and the time length $T - \Delta\tau$, describes the average effects of the stationary part of $x(t)$ in $[\Delta\tau, T]$ and is referred to here as the first-order statistical power density, and the second part,

$$\lambda E[\psi_1^2] \int_{-\Delta\tau}^{\Delta\tau} \int_0^{\Delta\tau - |k|} y(u + |k|) y(u) du \left(1 - \frac{|k|}{T - \Delta\tau} \right) \cos\omega k dk,$$

[0314] which depends on the mean square amplitude of each pulse $E[\psi_1^2]$ and the shape function $y(\mathbb{D})$ in addition to λ , T , and $\Delta\tau$, describes the variational effects of the stationary part of $x(t)$ and is referred to here as the second-order statistical power density. While $E[S_1(\omega)]$ in (75) consists of two parts, the first part,

$$\frac{2\lambda^2 E^2[\psi_1]}{T + \Delta\tau} \left[\int_{-\Delta\tau}^{\Delta\tau} \int_0^{\Delta\tau - |k|} y(v + |k|) y(v) dv \cos(\omega k) dk \right] \frac{1 - \cos(\omega T)}{\omega^2},$$

[0315] depends also on the shape function $y(\mathbb{D})$ as the shape function is used in calculating the power associated with the nonstationary parts of $x(t)$ in $[0, \Delta\tau]$ and $[T, T + \Delta\tau]$.

[0316] When the shape function is a delta function (i.e., $\Delta\tau \rightarrow 0$), the nonstationary parts of $x(t)$ vanish and $E[S_1(\omega)]$ in (75) can be shown to be equivalent to $E[S_2(\omega)]$ in (100). By (68) and (69), we have

$$\int_{-\Delta\tau}^{\Delta\tau} \int_0^{\Delta\tau - |k|} y(v + |k|) y(v) dv \cos(\omega k) dk = \quad (104)$$

-continued

$$\left| \int_0^{\Delta\tau} y(v) e^{-j\omega v} dv \right|^2$$

[0317] When $y(v) = W_0 \delta(v)$, where W_0 is a constant, we have from (104)

$$\lim_{\Delta\tau \rightarrow 0} \int_{-\Delta\tau}^{\Delta\tau} \int_0^{\Delta\tau - |k|} y(v + |k|) y(v) dv \cos\omega k dk = \quad (105)$$

$$\lim_{\Delta\tau \rightarrow 0} \left| \int_0^{\Delta\tau} W_0 \delta(v) e^{-j\omega v} dv \right|^2 = W_0^2$$

[0318] Since $|k| < \Delta\tau$ in (100), we have $|k| \rightarrow 0$ as $\Delta\tau \rightarrow 0$ and hence

$$\lim_{\Delta\tau \rightarrow 0} \left(1 - \frac{|k|}{T - \Delta\tau} \right) = 1 \quad (106)$$

[0319] Substituting (105) and (106) into (100) and noting that $W(\Delta\tau) = W_0$ when $y(v) = W_0 \delta(v)$, and substituting (105) into (75) and noting that $T + \Delta\tau \rightarrow T$ as $\Delta\tau \rightarrow 0$, yields

$$E[S_2(\omega)] = \quad (107)$$

$$E[S_1(\omega)] = 2\lambda^2 E^2[\psi_1] \frac{1 - \cos\omega T}{\omega^2 T} W_0^2 + \lambda E[\psi_1^2] W_0^2$$

[0320] By (104) the power spectral density in (101) can be expressed as

$$S_1(\omega) = 2\lambda^2 E^2[\psi_1] W^2(\Delta\tau) \delta(\omega) + \lambda E[\psi_1^2] W_0^2 \quad (108)$$

[0321] Where $Y(\omega) = \int_0^{\Delta\tau} y(t) e^{-j\omega t}$. When $T \rightarrow \infty$ in (75), we have by using (104)

$$S_1(\omega) = \lim_{T \rightarrow \infty} \frac{2\lambda^2 E^2[\psi_1] W^2(\Delta\tau) \delta(\omega) + \lambda E[\psi_1^2] W_0^2}{\langle Y(\omega)^2 \rangle} \quad (109)$$

[0322] Equation (109) has a slightly different form from that of (108) because the power associated with the nonstationary parts of $x(t)$ is included in (109). When $y(t) = W_0 \delta(t)$ (108) and (109) reduce to

$$S_1(\omega) = S(\omega) = 2\lambda^2 E^2[\psi_1] W_0^2 \delta(\omega) + \lambda E[\psi_1^2] W_0^2 \quad (110)$$

[0323] Equation (110) can also be obtained from (106) by letting $T \rightarrow \infty$ and using

$$\lim_{T \rightarrow \infty} \frac{1 - \cos\omega T}{\pi\omega^2 T} = \lim_{T \rightarrow \infty} \frac{2\sin^2 \frac{\omega T}{2}}{\pi\omega^2 T} = \delta(\omega) \quad (111)$$

EXAMPLES AND NUMERICAL SIMULATION

[0324] When the shape function of the pulses is represented by a half sine wave, i.e.,

$$y(t) = \sin\left(\frac{\pi t}{\Delta\tau}\right) H(t) - H(t - \Delta\tau) \quad (112)$$

[0325] where $H(0)$ is the Heaviside function, we obtain by using (60), (64), and (103)

$$E[X(j\omega)] = -\frac{E(\psi_1)j\pi\Delta\tau[1 + e^{-j\lambda\Delta\tau}(e^{-j\lambda\omega T} - 1)}{j\omega\Delta\tau^2 - \pi^2\Delta\tau^2} \quad (113)$$

$$E[S_1(j\omega)] = \frac{2\pi^2\Delta\tau^2[1 + \cos(\omega\Delta\tau)]}{(\omega^2\Delta\tau^2 - \pi^2)^2(T + \Delta\tau)} \left[\lambda TE(\psi_1^2) - \frac{2\lambda^2 E^2(\psi_1)(\cos\omega T - 1)}{\omega^2} \right] \quad (114)$$

$$E[S_2(j\omega)] = \lambda E(\psi_1^2)\Delta\tau^2 \left\{ \begin{array}{l} [-2T\pi^4 - 2T\cos(\omega\Delta\tau)\pi^4 + \\ (4\cos(\omega\Delta\tau)\pi^4 + \pi^4)\Delta\tau] \\ \hline (\omega^2\Delta\tau^2 - \pi^2)^2(T - \Delta\tau) \end{array} \right. \quad (115)$$

$$\begin{aligned} & \left. \begin{array}{l} [(-8\sin(\omega\Delta\tau))\omega\pi^2 + \\ 2T\cos(\omega\Delta\tau)\omega^2\pi^2 + 2T\pi^2\omega^2\Delta\tau^2] \\ \hline (\omega^2\Delta\tau^2 - \pi^2)^2(T - \Delta\tau) \end{array} \right. + \\ & \left. \begin{array}{l} \frac{[(\omega^4\Delta\tau^5 - 4\cos(\omega\Delta\tau)\omega^2\pi^2 - 2\omega^2\pi^2)\Delta\tau^3]}{(\omega^2\Delta\tau^2 - \pi^2)^2(T - \Delta\tau)} \\ \hline \end{array} \right. + \\ & \left. \begin{array}{l} \frac{8\lambda E^2(\psi_1)\Delta\tau^2(1 - \cos\omega(T - \Delta\tau))}{\pi^2\omega^2(T - \Delta\tau)} \end{array} \right) \end{aligned}$$

[0326] Consider next the normalized shape function $y(t)$ shown in FIG. 35 with unit maximum amplitude. It is obtained by averaging a series of normalized force pulses from impact tests in the four-bay space frame as shown in FIG. 10. There are 21 sample points in the shape function, which are connected, as shown in FIG. 34. Other parameters used are $T=8$ s, $\Delta\tau=20\pi/T=1024\pi=0.15625$ s where $h=T/1024=0.0078125$ s is the sampling interval, $\lambda=4.14$ /s, $E[\psi_1]=0.8239N$, and $E[\psi_1^2]=0.7163N^2$. The curve for $E[x(t)]$ in the time interval from 0 to 8.15625 s, shown as a solid line in FIG. 36, is calculated using (81). It is seen that $E[x(t)]$ increases from 0 to 0.0352 N in the first 0.15625 s, remains at 0.0352 N from 0.15625 s to 8 s, and decreases from 0.0352 N to 0 in the last 0.15625 s. The curve for $20\log|E[X(j\omega)]|$ in the frequency range from 0 to 50 Hz, shown as a dotted line in FIG. 37, is calculated using (61). The curve for $10\log|E[S_i(j\omega)]|$ in the same frequency range,

shown as a solid line in FIG. 38, is calculated using (75). The curve for $10\log|E[S_i(j\omega)]|$ with $\lambda=1$ /s and the other parameters unchanged is shown as a dashed line in FIG. 38. It is seen that $E[S_i(j\omega)]$ increases by 4.14 to 15.6247 times in the frequency range shown when λ is increased from $\lambda_2=1$ /s to $\lambda_1=4.14$ /s. This result can be shown by using (75)

$$\frac{\lim_{\omega \rightarrow \infty} E[S_1(j\omega)]}{\lim_{\omega \rightarrow \infty} E[S_1(j\omega)]} = \frac{\lambda_1^2 E^2(\psi_1)T^2 + \lambda_1 TE[\psi_1^2]}{\lambda_2^2 E^2(\psi_1)T^2 + \lambda_2 TE[\psi_1^2]} = \quad (116)$$

$$\frac{\lambda_1^2 E^2(\psi_1)T + \lambda_1 E[\psi_1^2]}{\lambda_2^2 E^2(\psi_1)T + \lambda_2 E[\psi_1^2]} = 15.6247$$

$$\frac{\lim_{\omega \rightarrow \infty} E[S_1(j\omega)]}{\lim_{\omega \rightarrow \infty} E[S_1(j\omega)]} = \frac{\lambda_1}{\lambda_2} = 4.14 \quad (117)$$

[0327] This shows that a larger arrival rate λ would increase the energy input to the structure over the entire frequency domain.

[0328] Numerical simulation is undertaken next to validate the analytical predictions. The random number $N(T)$ satisfying the Poisson distribution in (51) with $\lambda=4.14$ /s and $T=8$ s is generated using MATLAB. Similarly, the random numbers corresponding to the random variables τ_i ($i=1, 2, \dots, N(T)$), satisfying the uniform distribution in (52), and the random numbers corresponding to the random variables ψ_i ($i=1, 2, \dots, N(T)$), satisfying the Gaussian distribution in (53) with $\mu=0.8239$ N and $\sigma^2=0.7163-0.82392 N^2=0.0375 N^2$, are generated. Using the shape function constructed earlier, a sample function of $x(t)$ in (50) at time $t=rh$, where $t=0, 1, \dots, T$,

$$R-1 \left(R = \frac{T + \Delta\tau}{h} = 1044 \right).$$

[0329] denoted by x_r , can be obtained. The discrete Fourier transform (DFT) of the time series $\{x_r\}$ is calculated using MATLAB. The DFT of the series $\{x_r\}$ is defined by

$$X_q = \frac{1}{R} \sum_{r=0}^{R-1} x_r e^{-j\frac{2\pi qr}{R}} \quad (118)$$

[0330] where $q=0, 1, \dots, R-1$. Equation (118) is an approximate formula for calculating the coefficients of the Fourier series of a periodic function whose values in the period $[0, T+\Delta\tau]$ are given by those of $x(t)$:

$$X_q = \frac{1}{T + \Delta\tau} \int_0^{T + \Delta\tau} x(t) e^{-j\frac{2\pi qt}{T + \Delta\tau}} dt \quad (119)$$

[0331] The Fourier components X_q correspond to harmonics of frequency

$$\omega_q = \frac{2\pi q}{T + \Delta T}.$$

[0332] Recall that the Fourier transform of $x(t)$ in (50) is given by

$$X(j\omega) = \int_0^{T+\Delta T} x(t)e^{-j\omega t} dt \quad (120)$$

[0333] Let

$$\omega = \omega_q = \frac{2\pi q}{T + \Delta T}$$

[0334] in (120) and compare the resulting expression with (119), we find that X_q in (118) multiplied by $T + \Delta T$ provides an approximate value of $X(j\omega)$ at frequency ω_q . Similarly, $X_q X^*_q$ multiplied by $T + \Delta T$ provides an approximate value of

$$S_1(\omega) = \frac{X(j\omega)X^*(j\omega)}{T + \Delta T}$$

[0335] at frequency ω_q . By averaging 5000 sample series of $\{x_i\}$, we obtain the curve for $E[x(0)]$, shown as a dotted line in FIG. 36. By averaging 1000 sample series of $\{20 \log[(T + \Delta T)|X_q|]\}$, we obtain the curve for $20 \log[E[X(j\omega)]]$, shown as a solid line in FIG. 37. By averaging 100 sample series of $\{10 \log[(T + \Delta T)|X_q X^*_q|]\}$, we obtain the curve for $10 \log[E[S_1(j\omega)]]$, shown as a dotted line in FIG. 38. The numerical results are in good agreement with the analytical ones.

[0336] The stochastic model was experimentally validated for an experimenter conducting manually a random series of impacts on the four bay space frame as shown in FIG. 10. One hundred ensemble averages were used. The experimental probability density functions of the arrival time, the number of arrived pulses, and the pulse amplitudes are in good agreement with the analytical values, as shown in FIGS. 39-41.

[0337] Thus, the system and method for detecting structural damage and the random impact series method as embodied and broadly described herein can be applied to an unlimited number and type of structures to provide automated, reliable damage detection and assessment and to conduct modal testing. This system could be further automated to conduct periodic tests and provide results to a centralized monitoring section. Regular health monitoring of these types of structures could provide additional protection against potential failure, as well as a characterization of usage and wear over time in particular environmental conditions for predicting useful service life.

[0338] The foregoing embodiments and advantages are merely exemplary and are not to be construed as limiting the

present invention. The present teaching can be readily applied to other types of systems. The description of the present invention is intended to be illustrative, and not to limit the scope of the claims. Many alternatives, modifications, and variations will be apparent to those skilled in the art. In the claims, means-plus-function clauses are intended to cover the structures described herein as performing the recited function and not only structural equivalents but also equivalent structures.

What is claimed is:

1. A system for determining stiffness parameters of a structure, comprising:

a sensor arranged to measure vibrations of said structure and output vibration information; and

a stiffness parameter unit for receiving said vibration information, determining natural frequency data of said structure, and determining the stiffness parameters of said structure using said natural frequency data.

2. The system according to claim 1, further comprising multiple sensors arranged to measure vibrations of said structure and output vibration information.

3. The system according to claim 1, wherein said stiffness parameter unit comprises an iterative processing unit.

4. The system according to claim 1, wherein said stiffness parameter unit comprises an outer iterative processing unit and an inner iterative processing unit.

5. The system according to claim 3, wherein said iterative processing unit determines said stiffness parameters using a first order perturbation process.

6. The system according to claim 3, wherein said iterative processing unit determines said stiffness parameters using a higher order perturbation process.

7. A system for determining stiffness parameters of a structure, comprising:

a sensor arranged to measure vibrations of said structure and output vibration information; and

a stiffness parameter unit for receiving said vibration information and determining said stiffness parameters with an iterative processing unit.

8. The system according to claim 7, wherein said iterative processing unit comprises an outer iterative processing unit and an inner iterative processing unit.

9. The system according to claim 7, wherein said iterative processing unit determines said stiffness parameters using a first order perturbation process.

10. The system according to claim 7, wherein said iterative processing unit determines said stiffness parameters using a higher order perturbation process.

11. A stiffness parameter unit for determining stiffness parameters for a structure, comprising:

an input for receiving vibration data related to the structure;

an analyzer for converting said vibration data to spectral data; and

an iterative processing unit for receiving said spectral data and outputting said stiffness parameters using natural frequencies of the structure.

12. A stiffness parameter unit for determining stiffness parameters for a structure, comprising:

an input for receiving vibration data related to the structure;

- an analyzer for converting said vibration data to spectral data; and
- an interactive processing unit for receiving said spectral data and outputting said stiffness parameters using a perturbation process.
13. The stiffness parameter unit according to claim 12, wherein said perturbation process comprises a first order perturbation process.
14. The stiffness parameter unit according to claim 12, wherein said perturbation process comprises a higher order perturbation process.
15. A system for determining damage information of a structure, comprising:
- a sensor arranged to measure vibrations of said structure and output vibration information;
 - a stiffness parameter unit for receiving said vibration information, determining natural frequency data of said structure, and determining the stiffness parameters of said structure using said natural frequency data; and
 - a damage information processor for receiving said stiffness parameters and outputting damage information.
16. The system according to claim 15, wherein said damage information processor outputs damage location information or extent of damage information.
17. A system, comprising:
- a structure;
 - a sensor arranged to measure vibrations of said structure and output vibration information; and
 - a stiffness parameter unit for receiving said vibration information, determining natural frequency data of said structure, and determining the stiffness parameters of said structure using said natural frequency data.
18. The system according to claim 17, further comprising a damage information processor for receiving said stiffness parameters and outputting location of damage.
19. The system according to claim 18, wherein said damage information processor comprises a damage location processor for determining damage location information.
20. The system according to claim 18, wherein said damage information processor comprises a damage extent processor for determining extent of damage information.
21. The system according to claim 18, wherein said damage information processor comprises a damage extent processor for determining extent of damage information and a damage location processor for determining damage location information.
22. The system according to claim 17, wherein said sensor comprises a velocimeter.
23. The system according to claim 17, wherein said sensor is attached to said structure.
24. The system according to claim 17, wherein said sensor is not attached to said structure.
25. The system according to claim 17, wherein said stiffness parameter unit further comprises a spectral analyzer.
26. The system according to claim 17, wherein said structure comprises a beam.
27. The system according to claim 17, wherein said structure comprises a truss.
28. The system according to claim 17, wherein said structure has a longest dimension less than 1.5 meters.
29. The system according to claim 17, wherein said structure has a longest dimension less than 2.5 meters.
30. The system according to claim 17, wherein said structure has a longest dimension less than 10 meters.
31. The system according to claim 17, wherein said structure has a longest dimension less than 50 meters.
32. A device, comprising:
- a random signal generating unit for generating first and second outputs;
 - a random impact actuator for receiving said first and second outputs; and
 - an impact applicator coupled to said random impact actuator and having an impact region;
- wherein said random impact actuator drives said impact applicator such that the force and arrival times of said impact applicator at said impact region are random.
33. The device of claim 32, wherein said random impact actuator drives said impact applicator in accordance with said first and second outputs.
34. The device of claim 33, wherein the first and second outputs comprise independent random variables.
35. The device of claim 34, wherein the first and second outputs determine the force and arrival times, respectively, of the impact applicator at the impact region.
36. A system, comprising:
- a structure;
 - a random impact device for inducing vibrations in said structure;
 - a sensor arranged to measure vibrations of said structure and output vibration information; and
 - a stiffness parameter unit for receiving said vibration information, determining natural frequency data of said structure, and determining the stiffness parameters of said structure using said natural frequency data.
37. The system of claim 36, wherein the random impact device comprises:
- a random signal generating unit for generating first and second outputs;
 - a random impact actuator for receiving said first and second outputs; and
 - an impact applicator coupled to said random impact actuator and having an impact region;
- wherein said random impact actuator drives said impact applicator such that the force and arrival times of said impact applicator at said impact region are random.
38. The device of claim 37, wherein said random impact actuator drives said impact applicator in accordance with said first and second outputs.
39. The device of claim 38, wherein the first and second outputs comprise independent random variables.
40. The device of claim 39, wherein the first and second outputs determine the force and arrival times, respectively, of the impact applicator at the impact region.
41. A system for determining stiffness parameters of a structure, comprising:

- a sensor arranged to measure vibrations of said structure and output vibration information; and
- a stiffness parameter unit for receiving said vibration information, determining mode shape information, and determining the stiffness parameters of said structure using said mode shape information.
- 42.** The system according to claim 41, further comprising multiple sensors arranged to measure vibrations of said structure and output vibration information.
- 43.** The system according to claim 41, wherein said stiffness parameter unit comprises an iterative processing unit.
- 44.** The system according to claim 41, wherein said stiffness parameter unit comprises an outer iterative processing unit and an inner iterative processing unit.
- 45.** The system according to claim 43, wherein said iterative processing unit determines said stiffness parameters using a first order perturbation process.
- 46.** The system according to claim 43, wherein said iterative processing unit determines said stiffness parameters using a higher order perturbation process.

* * * * *

EXHIBIT 3



US006526354B2

(12) **United States Patent**
Bose et al.

(10) **Patent No.:** US 6,526,354 B2
(45) **Date of Patent:** Feb. 25, 2003

(54) **SONIC WELL LOGGING FOR ALTERATION DETECTION**

WO WO 00/31568 6/2000 G01V1/48
WO WO 01/63322 8/2001

(75) Inventors: Sandip Bose, Bridgeport, CT (US);
Ramachandra Ganesh Shenoy, Paris
(FR)

(73) Assignee: Schlumberger Technology
Corporation, Ridgefield, CT (US)

(*) Notice: Subject to any disclaimer, the term of this
patent is extended or adjusted under 35
U.S.C. 154(b) by 0 days.

(21) Appl. No.: 09/741,573

(22) Filed: Feb. 1, 2001

(65) **Prior Publication Data**

US 2003/0010494 A1 Jan. 16, 2003

(51) Int. Cl. 7 G01V 1/40

(52) U.S. Cl. 702/14; 703/5

(58) Field of Search 702/14, 17; 367/31,
367/73; 703/5, 10; 324/303

(56) **References Cited**

U.S. PATENT DOCUMENTS

- 5,197,038 A * 3/1993 Chang et al. 367/28
5,381,092 A * 1/1995 Freedman 367/31
5,308,215 A * 3/1995 Sinha et al. 367/31
5,475,650 A 12/1995 Sinha et al. 367/31
5,798,982 A * 8/1998 He et al. 367/73
5,838,633 A 11/1998 Sinha 367/31
5,968,109 A * 10/1999 Izraei et al. 701/206
6,449,560 B1 * 9/2002 Kimball 702/6

FOREIGN PATENT DOCUMENTS

GB 2 313 667 12/1997 G01V1/48

OTHER PUBLICATIONS

Alford, R.M. *Shear Data in the Presence of Azimuthal Anisotropy*. 56th Ann. Int'l Soc. Expl. Geophys., Expanded Abstracts. (1986) pp. 476-479.

Burridge, R. and Sinha, B.K. *Inversion for Formation Shear Modulus and Radial Depth of Investigation Using borehole Flexural Waves*. SDR Research Report GEO-002-96-10 (Mar. 21, 1996).

* cited by examiner

Primary Examiner—Edward Lefkowitz

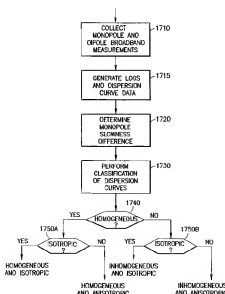
Assistant Examiner—Victor J. Taylor

(74) **Attorney, Agent, or Firm**—Martin M. Novack; William B. Batzer, John J. Ryberg

(57) **ABSTRACT**

A method for determining alteration of a region of an earth formation surrounding an earth borehole, comprising the steps of providing a logging device that is moveable through the borehole; transmitting sonic energy into the formation and receiving, at a plurality of transmitter-to-receiver spacings, sonic energy that has traveled through the formation, and producing signals representative of the received sonic energy for the plurality of transmitter-to-receiver spacings; determining sonic transit times and differential transit times for the respective transmitter-to-receiver spacings; deriving a test statistic from the differential transit times; and determining the presence of alteration of a region of the formations from the test statistic. An associated apparatus for carrying out the method is also described.

35 Claims, 20 Drawing Sheets



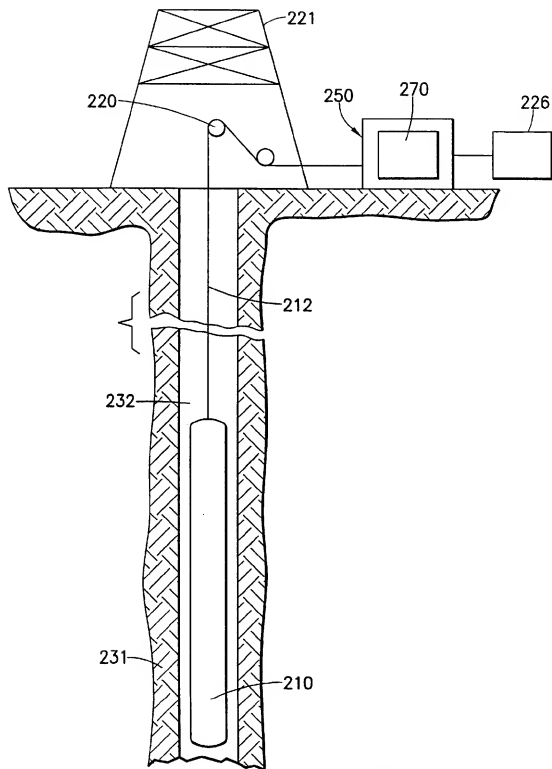


FIG.1

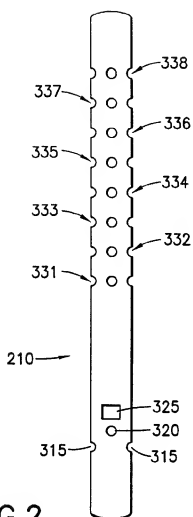


FIG.2

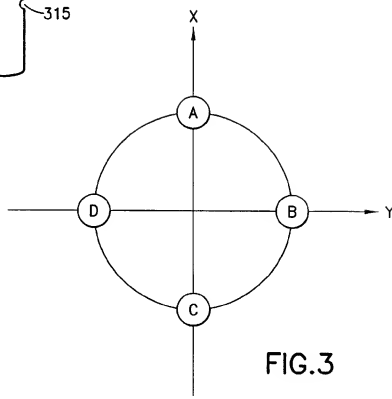
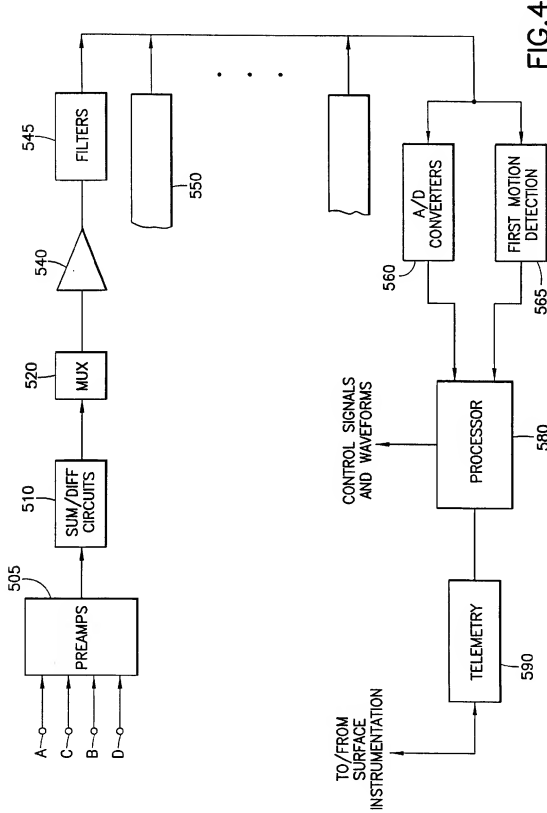


FIG.3



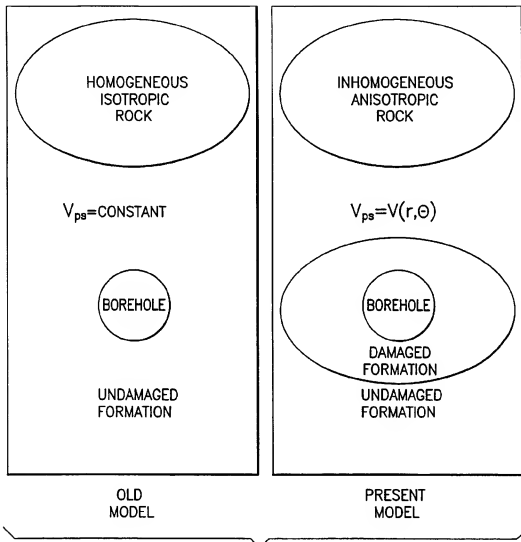


FIG.5

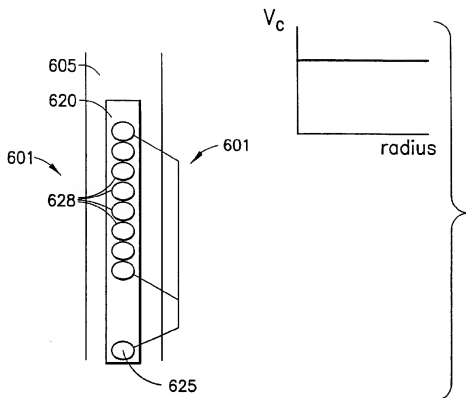


FIG. 6A

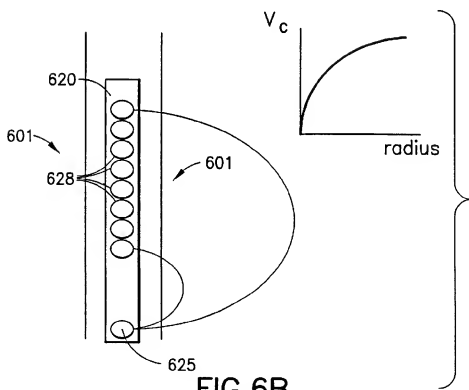


FIG. 6B

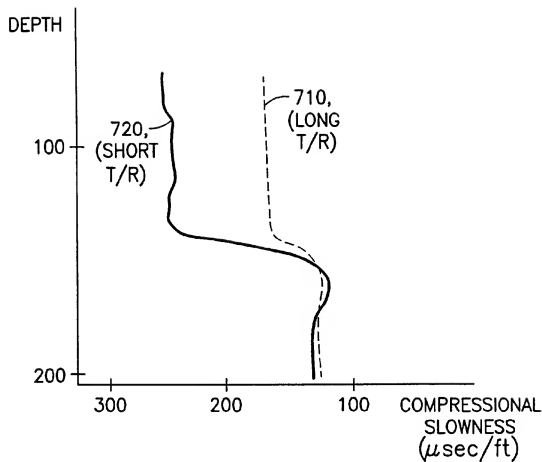


FIG.7

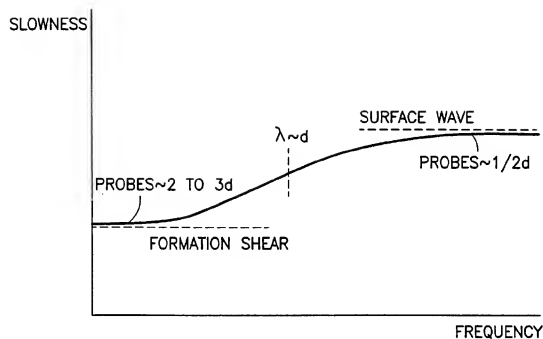


FIG.8

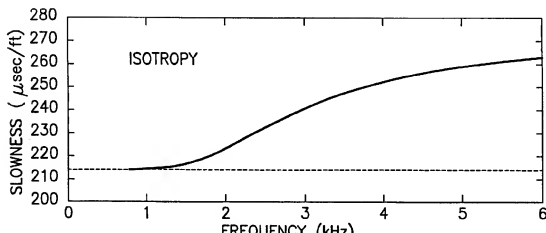


FIG.9A

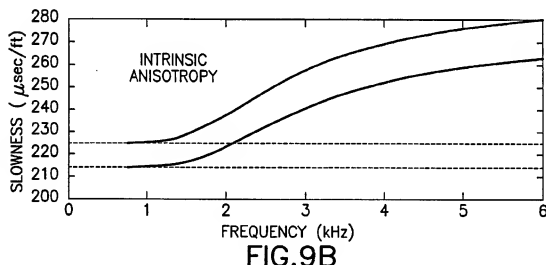


FIG.9B

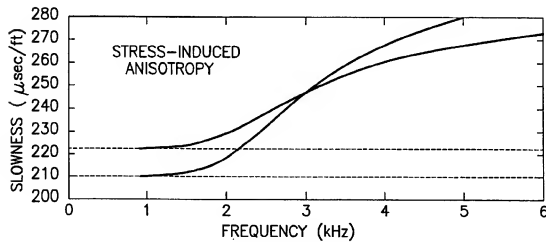


FIG.9C

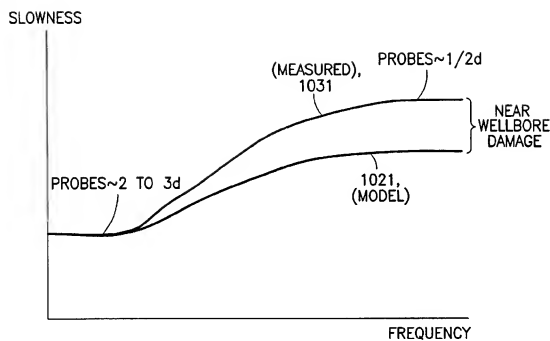


FIG.10

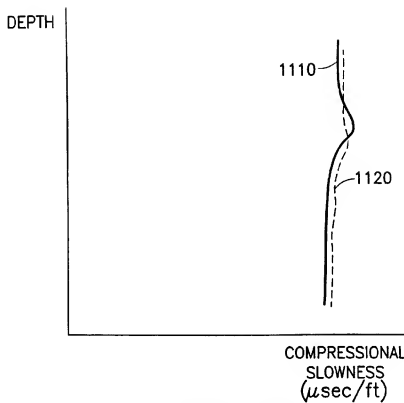


FIG.11A

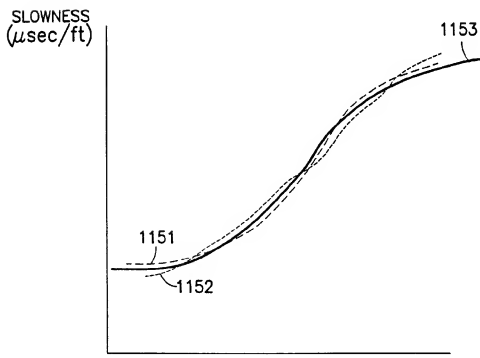
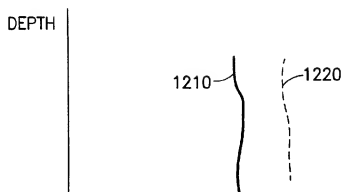


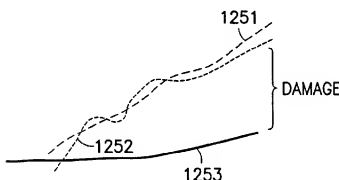
FIG.11B



COMPRESSORIAL
SLOWNESS
(μ sec/ft)

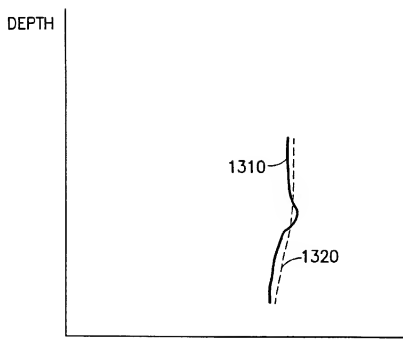
FIG. 12A

SLOWNESS
(μ sec/ft)



FREQUENCY

FIG. 12B



COMPRESSIONAL
SLOWNESS
(μ sec/ft)

FIG.13A

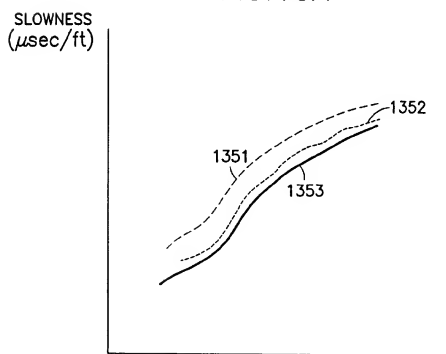


FIG.13B

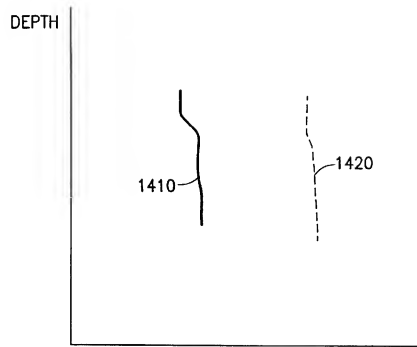


FIG. 14A

COMPRESSIONAL SLOWNESS ($\mu\text{sec}/\text{ft}$)

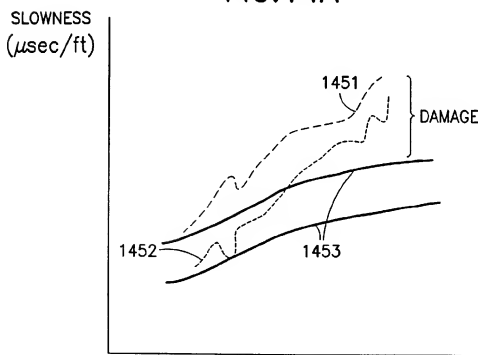


FIG. 14B

FREQUENCY

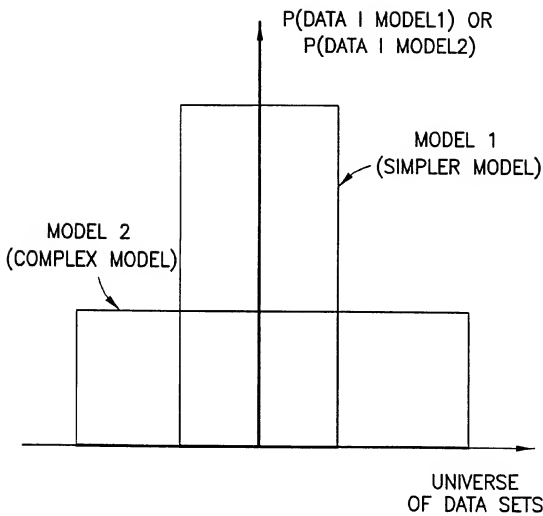


FIG.15

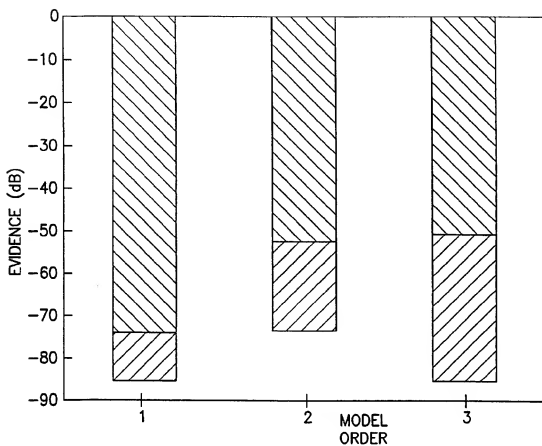


FIG.16



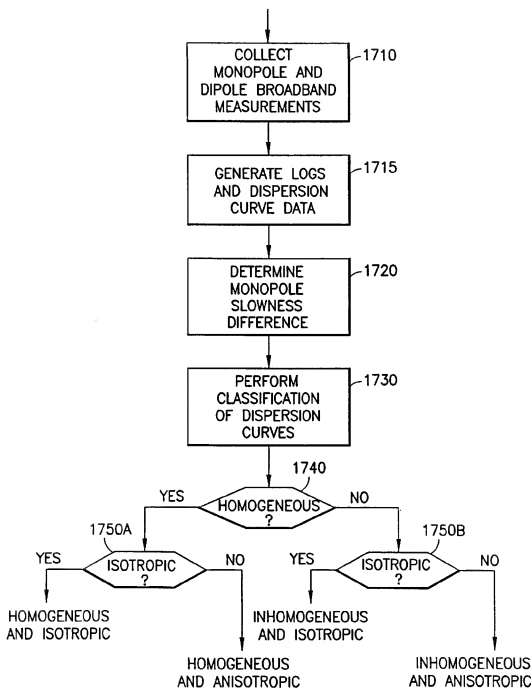


FIG.17

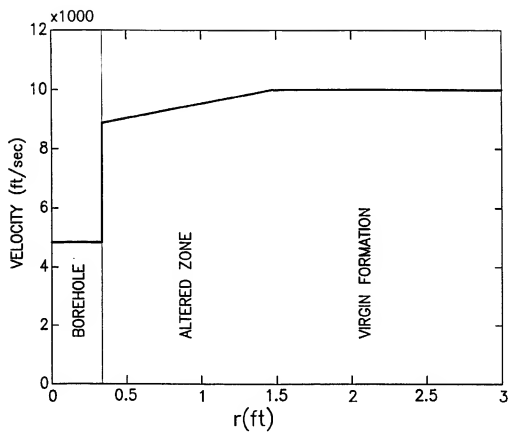


FIG.18

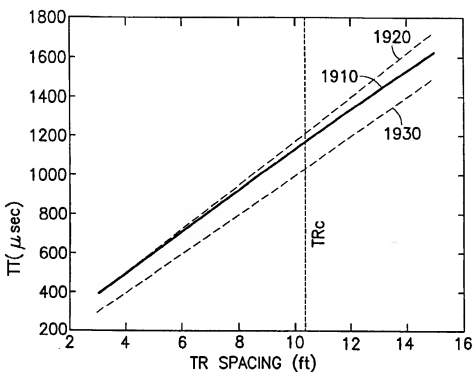


FIG.19

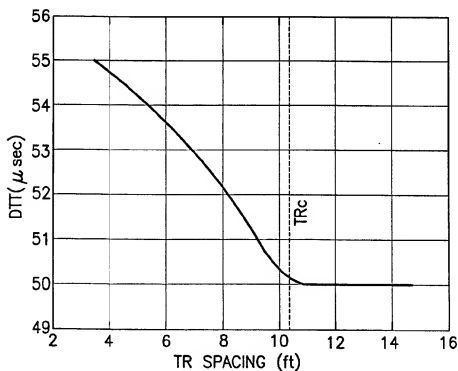


FIG.20

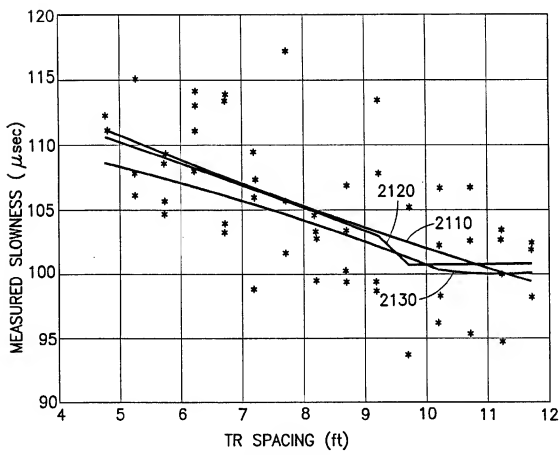


FIG.21

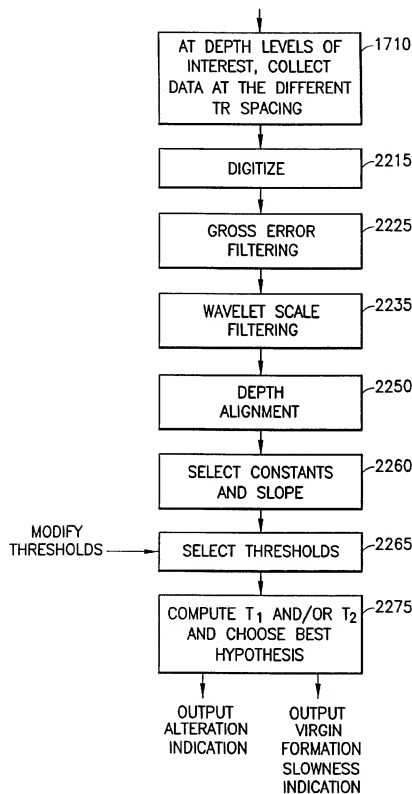


FIG.22

SONIC WELL LOGGING FOR ALTERATION DETECTION

RELATED APPLICATION

The present application contains subject matter that is related to subject matter in copending U.S. patent application Ser. No. 09/741574, entitled "Sonic Well Logging for Characterizing Earth Formations", Attorney Docket Number 601406, incorporated herein by reference, filed of even date herewith, and assigned to the same assignee as the present application.

FIELD OF THE INVENTION

This invention relates to investigation of earth formations, to a method and apparatus for determining properties of earth formations using sonic well logging which can characterize earth formations exhibiting complex acoustic behavior, such as can occur in anisotropic and/or inhomogeneous formations, and to a method and apparatus for determining alteration of a region of formations surrounding an earth borehole.

BACKGROUND OF THE INVENTION

It is well known that mechanical disturbances can be used to establish acoustic waves in earth formations surrounding a borehole, and the properties of these waves can be measured to obtain important information about the formations through which the waves have propagated. Parameters of compressional, shear and Stoneley waves, such as their velocity (or its reciprocal, slowness) in the formation and in the borehole, can be indicators of formation characteristics that help in evaluation of the location and/or producibility of hydrocarbon resources.

An example of a logging device that has been used to obtain and analyze sonic logging measurements of formations surrounding an earth borehole is called a Dipole Shear Sonic Imager ("DSI"—trademark of Schlumberger), and is of the general type described in Harrison et al., "Acquisition and Analysis of Sonic Waveforms From a Borehole Monopole And Dipole Source For The Determination Of Compressional And Shear Speeds And Their Relation To Rock Mechanical Properties And Surface Seismic Data", Society of Petroleum Engineers, SPE 20557, 1990. In conventional use of the DSI logging tool, one can present compressional slowness, Δt_c , shear slowness, Δt_s , and Stoneley slowness, Δt_{sp} , each as a function of depth, z. [Slowness is the reciprocal of velocity and corresponds to the interval transit time typically measured by sonic logging tools.] Typically, the subsurface formations are considered to be homogeneous and isotropic material, where the compressional and shear velocities, V_c and V_s , of the formations are only a function of depth.

It is known that formations can be anisotropic, where the compressional and shear slownesses are a function of azimuth, θ . Anisotropy can occur, for example because of layered shales, aligned fractures or differences in the magnitudes of the principal stresses in the formations.

It is also known that formations may be inhomogeneous, where the slownesses become a function of radial distance r , from the borehole. Inhomogeneity can be caused, for example, by mud-shale interactions or by mechanical damage due to stress concentrations.

It is among the objectives of the present invention to provide an improved technique for characterizing earth formations exhibiting complex acoustic behavior. It is

among the further objects of the invention to provide an improved technique and apparatus for detecting alteration of a region of earth formations surrounding a borehole.

SUMMARY OF THE INVENTION

A form hereof provides a technique for jointly processing monopole and dipole measurements from a sonic logging device to obtain a more complete characterization of the acoustic behavior of formations surrounding an earth borehole. From an integrated sonic inversion, improved estimates of slowness, as well as characterization of the near wellbore damage region, can be obtained.

In accordance with a form hereof, a method is set forth for determining properties of an earth formation surrounding an earth borehole, comprising the following steps: (a) providing a logging device that is moveable through the borehole; (b) transmitting sonic energy into the formation, receiving, at the logging device, sonic energy that has travelled through the formation, and producing signals representative of the received sonic energy; (c) determining, from the signals, whether the formation is anisotropic; (d) determining, from the signals, whether said formation is inhomogeneous; and (e) responsive to the determinations of steps (c) and (d), outputting a characterization of the formation as one of the following types: isotropic/homogeneous, anisotropic/homogeneous, isotropic/inhomogeneous, and anisotropic/inhomogeneous. In an embodiment of this form of the technique, the step (b) includes transmitting sonic energy from a monopole source, and receiving sonic energy from the monopole source at a plurality of different transmitter-to-receiver spacings on the logging device, and the step (d) includes determining whether said formation is inhomogeneous from deviations between signals at different transmitter-to-receiver spacings. In this embodiment, the step (b) also includes transmitting dipole shear sonic energy, receiving dipole shear sonic energy that has travelled through the formation, and producing signals representative of the received sonic energy over a range of frequencies, and the step (c) includes determining whether the formation is anisotropic from said signals. It will be understood that the step of transmitting dipole shear sonic energy can comprise producing what is commonly referred to as a flexural wave by employing a dipole source in the borehole to cause a flexing of the borehole wall.

In a further form hereof, a method is set forth for determining properties of an earth formation surrounding an earth borehole, comprising the following steps: (a) providing a logging device that is moveable through the borehole; (b) transmitting monopole and dipole sonic energy from the logging device into the formations and receiving, at the logging device, monopole and dipole sonic energy that has travelled through the formations, and producing measurement signals representative of the received monopole and dipole sonic energy; (c) devising a plurality of formation models of different complexities; (d) comparing model signals from the models with the measurement signals; and (e) selecting one of the models based on said comparing step. In an embodiment of this form of the invention, the plurality of models includes four models, the models, in order of increasing complexity, being a homogeneous/isotropic model, a homogeneous/anisotropic model, an inhomogeneous/isotropic model, and an inhomogeneous/anisotropic model. Also in this embodiment, the step (e) selection of a model takes into account model complexity as well as the results of the comparing step.

A feature of the new sonic characterization of a form hereof is that a joint processing of compressional and shear

data is being used to indicate the "state" of the formation, in the context of inhomogeneity and/or anisotropy. This "state" of the formation would be a function of depth. Some of the applications fall into two general categories; those requiring "undamaged" parameters, and those applications requiring "damaged" parameters. "Undamaged" parameters (the velocities V_p and V_s of the virgin formation) can be used by geophysics and petrophysics experts to evaluate the reservoir and overburden rock in the traditional manner. With the method hereof, there will be improved confidence that the measurements have a deep enough depth of investigation to be representative of the undamaged formation.

Near wellbore "damaged" parameters are new information of use to drilling and completions engineers. As an example, for inhomogeneity in a reservoir caused by stress concentrations, the location of damaged zones can influence the completion and perforating strategy. One can selectively perforate to avoid damaged zones. Also, detection of damage from sonics can have an impact on other logging measurements that have shallow depths of investigations, so suitable adjustments can be made.

In accordance with a form of the present invention, there is set forth a method for determining alteration of a region of an earth formation surrounding an earth borehole, comprising the following steps: providing a logging device that is moveable through the borehole; transmitting sonic energy into the formation and receiving, at a plurality of transmitter-to-receiver spacings on the logging device, sonic energy that has traveled through the formation, and producing signals representative of the received sonic energy for the plurality of transmitter-to-receiver spacings; determining, from the signals, sonic transit times and differential transit times for the respective transmitter-to-receiver spacings; deriving a test statistic from the differential transit times; and determining the presence of alteration of a region of the formations from the test statistic. In a preferred embodiment of this form of the invention, the test statistic includes a component that depends on the degree to which the differential transit times decrease monotonically as a function of transmitter-to-receiver spacing, and the step of determining the presence of alteration of a region of the formations from the test statistic comprises comparing the test statistic to a threshold.

An embodiment of the invention employs a test statistic T_1 of the form

$$T_1 = \frac{\sum_i (DTT_i - DTT)^2}{\min_{i \neq j} \sum_i (DTT_i - mTR_i - c)^2}$$

where DTT_i are the individual differential transit times, DTT is the average of the differential transit times, TR_i are the individual transmitter-to-receiver spacings, and m and c are constants.

Further features and advantages of the invention will become more readily apparent from the following detailed description when taken in conjunction with the accompanying drawings.

BRIEF DESCRIPTION OF THE DRAWINGS

FIG. 1 is a diagram, partially in block form, of a type of apparatus that can be used in practicing embodiments hereof.

FIG. 2 is a simplified diagram of a type of downhole logging device that can be used in practicing embodiments hereof.

FIG. 3 is a diagram illustrating, in cross-section, the placement of hydrophones that can be used at a receiver station in the logging device of FIG. 3.

FIG. 4 is a block diagram of a portion of the electronics of the FIG. 2 logging device.

FIG. 5 is a conceptual diagram showing, on the left, a traditional model used in sonic characterization of formations and, on the right, a more general model used in a form of hereof.

FIG. 6, which includes FIGS. 6A and 6B, show simplified sonic logging device representations, with a source and receivers, and illustrate ray paths from a monopole source in a homogeneous formation (FIG. 6A) and in an inhomogeneous formation (FIG. 6B).

FIG. 7 illustrates a portion of a log of compressional slowness at relatively long and relatively short transmitter-to-receiver spacings.

FIG. 8 shows a dipole dispersion curve of slowness as a function of frequency.

FIG. 9, which includes FIGS. 9A, 9B, and 9C, shows dipole dispersion curves for situations of formation isotropy (FIG. 9A), formation intrinsic anisotropy (FIG. 9B), and formation stress-induced anisotropy (FIG. 9C).

FIG. 10 shows dipole dispersion curves for a model formation and for measured data, respectively, and illustrates a situation of near wellbore damage.

FIG. 11, which includes FIG. 11A and FIG. 11B, shows, in FIG. 11A, monopole compressional slowness as a function of depth for relatively short and relatively long transmitter-to-receiver spacings for a case of a homogeneous and isotropic formation, and, in FIG. 11B, dipole dispersion curves and a model dipole dispersion curve of slowness as a function of frequency for the case of a homogeneous and isotropic formation.

FIG. 12, which includes FIG. 12A and FIG. 12B, shows, in FIG. 12A, monopole compressional slowness as a function of depth for relatively short and relatively long transmitter-to-receiver spacings for a case of an inhomogeneous and isotropic formation, and, in FIG. 12B, dipole dispersion curves and a model dipole dispersion curve of slowness as a function of frequency for the case of an inhomogeneous and isotropic formation.

FIG. 13, which includes FIG. 13A and FIG. 13B, shows, in FIG. 13A, monopole compressional slowness as a function of depth for relatively short and relatively long transmitter-to-receiver spacings for a case of a homogeneous and anisotropic formation, and, in FIG. 13B, dipole dispersion curves and a model dipole dispersion curve of slowness as a function of frequency for the case of a homogeneous and anisotropic formation.

FIG. 14, which includes FIG. 14A and FIG. 14B, shows, in FIG. 14A, monopole compressional slowness as a function of depth for relatively short and relatively long transmitter-to-receiver spacings for a case of an inhomogeneous and anisotropic formation, and, in FIG. 14B, dipole dispersion curves and a model dipole dispersion curve of slowness as a function of frequency for the case of an inhomogeneous and anisotropic formation.

FIG. 15 shows an example of the model selection, with comparison of simple and complex models.

FIG. 16 illustrates an example of determining the number of dispersion curves resulting from dipole data, using a likelihood factor approach.

FIG. 17 is a flow diagram of a routine for programming a processor to implement a routine in accordance with an embodiment hereof.

FIG. 18 is a diagram of an example of a linear radial profile of velocity around the borehole.

FIG. 19 illustrates the variation of transit time with transmitter-to-receiver spacing for the linear radial profile of FIG. 18.

FIG. 20 shows differential transit time as a function of transmitter-to-receiver spacing for the transit times of FIG. 19.

FIG. 21 shows best fit outcomes for exemplary data showing how two test statistics can be fitted to data.

FIG. 22 is a flow diagram of a routine, in accordance with an embodiment of the invention, for determining alteration around the borehole and virgin formation slowness.

DETAILED DESCRIPTION

Referring to FIG. 1, there is shown a type of apparatus which can be used in practicing embodiments of the invention. Subsurface formations 231 are traversed by a borehole 232 which is typically, although not necessarily, filled with drilling fluid or mud. A logging tool 210 is suspended on an armored cable 212 and may have optional centralizers (not shown). The cable 212 extends up the borehole, over a sheave wheel 220 on a derrick 221 to a winch forming part of surface equipment 250. Known depth gauging apparatus (not shown) is provided to measure cable displacement over the sheave wheel 220 and accordingly the depth of the logging tool 210 in the borehole 232. A device of a type well known in the art is included in the tool 210 to produce a signal indicative of orientation of the body of the tool 210. Processing and interface circuitry within the tool 210 amplifies, samples and digitizes the tool's information signals for transmission and communicates them to the surface equipment 250 via the cable 212. Electrical power and control signals for coordinating operation of the tool 210 are generated by the surface equipment 250 and communicated via the cable 212 to circuitry provided within the tool 210. The surface equipment includes processor subsystem 270 (which can typically include a microprocessor, memory, clock and timing, and input/output functions—not separately shown), standard peripheral equipment (not separately shown), and recorder 226.

The logging device 210 may be, for example, of a type known as a Dipole Shear Sonic Imager ("DSI"—trademark of Schlumberger) generally described in Harrison et al., "Acquisition and Analysis of Sonic Waveforms From a Borehole Monopole and Dipole Source for the Determination of Compressional and Shear Slides and Their Relation to Rock Mechanical Properties and Surface Seismic Data", Society of Petroleum Engineers, SPE 20557, 1990. It will be understood, however, that any suitable logging device can be utilized. Further details of the logging device 210 of this example are shown in FIG. 2. The logging device 210 includes crossed dipole transmitters 315 and 320 (only one end of dipole 320 being visible) and a monopole transmitter 325, so that waves including compressional, shear, Stoneley, and flexural can be excited. Eight, or other suitable number, of spaced apart receiver stations, designated 331 through 338 each comprise four receiver hydrophones mounted azimuthally at ninety degree intervals in the surface of the cylindrical logging device. FIG. 3 shows the hydrophones, designated A, B, C, and D. In an example shown in FIG. 4, an X component can be obtained by subtracting the signals received at A and C (i.e., A-C), and a Y component can be obtained by subtracting the signals received at B and D (i.e., B-D). With four receiver elements at each receiver station, there are a total of thirty two receiver elements in this

example. The receiver stations are also configurable for monopole reception.

The transmitter electronics contain a power amplifier and switching circuitry capable of driving the two crossed-dipole transmitter elements and the monopole element from a programmable waveform. Separate waveforms with appropriate shape and frequency content can be used for dipole, Stoneley and compressional measurements. The receiver electronics processes the signals from the 32 individual receiver elements located at the eight receiver stations which are spaced six inches apart. At each station, four receivers are mounted as shown in FIG. 3 which allows measurement of the dipole and crossed-dipole waveforms by differencing the outputs from opposite receivers, as previously described. Summing the outputs of the receivers can be used to produce a monopole equivalent signal. As further described in Harrison et al., *supra*, the receiver electronics multiplexers, filters, amplifies and channels the signals from the 32 receiver elements to 8 parallel signal paths. These eight parallel analog signals are passed to an acquisition electronics cartridge where eight 12-bit analog-to-digital converters digitize the signals from the receiver electronics. The telemetry circuitry passes the digitized information to the earth's surface.

FIG. 4 shows an example of the acquisition signal path in block diagram form for one of the eight (or other suitable number of) receiver stations, as described in Harrison et al., *supra*. Each receiver has its own charge preamplifier (represented at 505). The output of the receivers, odd numbered pairs being in-line with the upper dipole transmitter and even numbered pairs with the lower dipole transmitter, passes into both a summing circuit (for monopole measurements) and a differencing circuit (for dipole measurements), as represented at 510. Under software control the sum or difference is selected by a multiplexer stage (block 520) and the signal passed to one of eight programmable gain amplifier stages (540) and filters (545). The other similar channels are represented by block 550. The eight parallel analog signals are passed to eight parallel 12-bit A/D converters (represented at 560) where simultaneous waveform digitization is performed. If desired, more bits can, of course, be used to advantage. After digitization, the eight waveforms pass to the memory section associated with downhole processor 580. The processor also provides control signals and waveforms to transmitter and receiver electronics. An alternate path directs the eight analog receiver signals into threshold crossing detection circuitry or digital first motion detection, as represented at block 565. This circuitry detects the time of all up or down going threshold crossings. The digitized waveform data and the threshold crossing time data are passed to the surface using telemetry circuitry 590. It will be understood that more advanced tool implementations, having further transmitters, receivers, and/or transmitter-to-receiver (T/R) spacings, and more powerful processing capabilities, can be used even more advantageously, consistent with the principles hereof, in practicing embodiments of the invention.

In the FIG. 2 embodiment, the processing of signals recorded uphole can be implemented using a processor 270, such as a suitably programmed general purpose digital processor with memory and peripherals conventionally provided. It will be understood, however, that the processing need not be performed at the wellsite, and that signals derived at the wellsites can be processed at a remote location. It will also be understood that other suitable logging tools can be employed in practicing the invention.

The traditional sonic log presents compressional slowness, Δt_c , and shear slowness, Δt_s , and Stoneley

slowness, Δt_{sr} , as a function of depth, z . This description has usually been based on the idea that rock can be described as a homogeneous and isotropic material where the compressional and shear velocities, V_c and V_s , of the formation are only a function of depth. It has become recognized however, that this is not a complete characterization of the formation. Formations may be anisotropic where the compressional and shear slownesses are a function of azimuth, θ . Anisotropy can occur because of layered shales, aligned fractures or differences in the magnitudes of the principal stresses. Formations may also be inhomogeneous where the slownesses become a function of radial distance from the borehole, r . Inhomogeneity can be caused, for example, by mud-shale interactions or by mechanical damage due to stress concentrations.

A form hereof addresses the compressional and shear velocity around a borehole, $V_{c,s}(r,\theta)$, at a single depth and a processing chain to exploit the model. Conceptually, a model of velocity around a borehole model is shown in FIG. 5. The velocities $V_{c,s}(r,\theta)$ associated with the model are described as only a function of radius and azimuth. A typical old model, shown on the left, depicts a homogeneous and isotropic formation with $V_{c,s}(r,\theta)=\text{constant}$. In the old model, the rock around the borehole is assumed to be the same as if no borehole was ever drilled through the rock. The model hereof, on the right, assumes that the drilling process and related stress concentrations and/or mud system may have damaged or altered the rock from its pre-drilled state. At this stage, consider the general case where the altered, changed or damaged rock (see Plona, T. J., Sinha, B. K., Winkler, K. W., and D'Angelo, R., "Measurement of Stress Direction and Mechanical Damage Around Stressed Boreholes Using Dipole and Microseismic Techniques", SPE 47234 presented at Eurock '98 (1998)) can have an elliptical region around the borehole that has been perturbed. The elliptical region implies that the formation can be both anisotropic and inhomogeneous, i.e., $V_{c,s} \neq V(r,\theta)$.

With the rock around the borehole modeled to have both radial and azimuthal variations of sound speeds, an embodiment hereof uses both monopole and dipole data from a sonic tool or tools, processed jointly, to yield a more complete characterization of the formation acoustic properties. Historically, sonic logging has evaluated compressional and shear data independently. In a form of the present invention, compressional and shear data are processed in a joint manner in order to get a more complete characterization of the formation. Inputs to this characterization are the monopole compressional slowness and the dipole shear slowness.

For the monopole input, in this form of the invention, monopole compressional data is obtained at both relatively short transmitter/receiver (T/R) spacings (for example, 3 to 5 ft.) and relatively long T/R spacings (for example, 8 to 12 ft.). The data can be obtained using any suitable technique, for example with the type of equipment described in conjunction with FIGS. 1-4. Reference can be made, for example, to the data obtained in Homby, B. E. "Tomographic Reconstruction of Near-Borehole Slowness Using Refracted Borehole Sonic Arrivals", Geophysics, 58, 1726-1738, (1993).

In the simplified diagrams of FIGS. 6A and 6B, formation is represented at 601, a borehole is represented at 605, a logging device is represented at 620, a monopole source is represented at 625, and receivers are represented at 628.

In FIG. 6A the sound rays are shown as propagating from the monopole source to the receivers in straight lines. The

small graph inset indicates that the sound speed is substantially constant with radius. This is the traditional concept of monopole sonic logging where the assumption is generally that the formation is homogeneous. However, when there is a gradient of sound speed vs radius (i.e., inhomogeneity), it is known that sound propagates in curved ray paths. For the case indicated in FIG. 6B, where the sound speed increases vs radius from the borehole, the ray paths are curved such that energy returns to the borehole. In this case, the ray path that arrives at the nearest receiver senses a velocity that is indicative of the formation near the wellbore (that is, a shallow depth of investigation). In contrast, the ray path that arrives at the farthest receiver senses a velocity which is indicative of the formation relatively far away from the borehole (i.e., a relatively deep depth of investigation, not substantially affected or perturbed by the borehole). Thus, the measured velocity depends on the T/R spacing. The difference in the slowness measurement at short and long T/R spacings provides an indication of formation inhomogeneity.

Consider the example of logs of slowness data as in FIG. 7. The track 710 represents the slowness at the long T/R spacing and is generally indicative of the unperturbed or undamaged rock. The track 720 represents the slowness at the short T/R spacing and is characteristically a higher slowness (i.e., lower velocity). The difference in the two curves, at depth levels between about 100 and 150 ft. in this example, indicates radial variations of velocity (i.e., inhomogeneity).

For the dipole shear measurements, the data is acquired in the crossed dipole mode, and the data can be used to determine the isotropy or anisotropy of the formation. The four-component rotation method of Alford can be used. (See Alford, R. M., 1986, "Shear Data In the Presence Of Azimuthal Anisotropy", 56th Ann. Internat., Soc. Expl. Geophys., Expanded Abstracts, 476-479). Slowness is evaluated as a function of frequency (i.e., the dispersion curve.) In FIG. 8, a basic dipole flexural mode dispersion curve is shown, where "d" refers to the diameter of the borehole. There are several points to observe from this Figure. First, the dispersion curve approaches the formation shear slowness at low frequencies. Second, at low frequencies (and long wavelength) the dipole signal is sensing 2 to 3 borehole diameters into the formation. Third, at high frequencies (and short wavelengths), the dipole signal is sensing approximately $\frac{1}{2}$ the borehole diameter into the formation. Thus, the information at different frequencies is sensing sound speeds at different depths of investigation. (See Sinha, B. K., Norris, A. N., and Chang, S. K., 1994, "Borehole Flexural Modes In Anisotropic Formations", Geophysics, 59, 1037-1052.)

In FIG. 9, which includes graphs 9A, 9B and 9C, it is shown how the dispersion curves indicate the isotropy or anisotropy of the formation. In the plot 9A, there is only one dispersion curve visible. This is because the two curves from the respectively orthogonal dipole pairs (see e.g. FIG. 3) substantially overlap. This is the case when the formation is isotropic. The dispersion curve approaches the shear speed (dashed line) at low frequencies. In the plots 9B and 9C there are two dispersion curves, and this indicates that the formation is anisotropic. The plot 9B shows the case when the formation anisotropy is "intrinsic" and the two dispersion curves do not cross. (See Sinha, B. K., Norris, A. N., and Chang, S. K., 1994, *supra*.) The plot 9C shows the case when there is stress-induced anisotropy and the two dispersion curves cross. (See Sinha, B. K., and Kostek, S., 1996, "Stress Induced Azimuthal Anisotropy In Borehole Flexural

Waves": Geophysics, 61, no. 6, 1899-1907.) The crossing nature of the stress-induced anisotropy dispersion curves is a feature that permits a discrimination to be made between the two types of anisotropy. These stress-induced anisotropy effects have been observed in field data. (Sinha B. K., Kane, M., and Frignet, B., "Dipole Dispersion Crossover And Sonic Logs In Limestone Reservoirs", Geophysics, 65, No. 2 (March-April 2000), pp. 390-407).

In addition to the distinction between isotropy and anisotropy, dispersion curves can also yield an indication of homogeneity/inhomogeneity. This is illustrated in conjunction with FIG. 10. In this Figure, the model data is represented at curve 1021 and the measured data is represented at 1031. The model data can be produced, for example, from measured compressional and shear velocities, formation mass density, mud density, mud compressional velocity, and borehole diameter (see Sinha, B. K., Norris, A. N., Norris, A. N., and Chang, S. K., 1994, Borehole Flexural Modes In Anisotropic Formations, Geophysics, 59, 1037-1052). If the measured data superimposes with the model data, it can be concluded that the formation is homogeneous. When the measured data deviates at high frequency (as in the Figure), it can be concluded that the formation is inhomogeneous. Since the deviation occurs at high frequency that corresponds to probing near to the borehole, this deviation indicates that there is lower sound speed near the borehole wall, i.e., inhomogeneity or damage.

With the basic realization that the rock around the borehole may have both radial and azimuthal variations of sound speeds, both monopole and dipole data from sonic tools can be utilized to give a more complete characterization of the formations acoustic properties. In a preferred embodiment hereof, the sonic characterization includes four categories as follows:

Homogeneous and Isotropic

Inhomogeneous and Isotropic

Homogeneous and Anisotropic

Inhomogeneous and Anisotropic

In the present embodiment, monopole compressional slownesses and dipole shear slownesses are used in determining the appropriate characterizations. From the monopole compressional data, a determination is made as to whether or not the compressional slowness is a function of transmitter-to-receiver (T/R) spacing. If the compressional slowness is not a function of T/R spacing, then the formation is deemed homogeneous. If the compressional slowness is a function of T/R spacing, particularly, if the slowness decreases with increasing T/R spacing, the formation is deemed to be inhomogeneous. [Reference can also be made to the technique described in conjunction with FIGS. 18-22.] From the crossed dipole shear data, it can be determined if the formation is isotropic (one shear slowness) or anisotropic (two shear slownesses). In addition, inhomogeneity can be determined from the deviation of the measured dispersion curve from the modeled curve. With these determinations, an acoustic description of the formation can be given as one of the above-listed characterizations: homogeneous/isotropic; inhomogeneous/isotropic; homogeneous/anisotropic; or inhomogeneous/anisotropic.

The following set of Figures, FIGS. 11-14, show examples of types of sonic field data that highlight homogeneity/inhomogeneity and/or isotropy/anisotropy in formations. The monopole data of these examples is extracted from the idealized data of FIG. 3. (See Hornby, supra.) The dipole data is field data from the sonic logging tool described in conjunction with FIGS. 2-4. Although in

these examples the monopole and dipole data have been derived from different wells, the data has been combined in this set of examples to illustrate the principle hereof. It will be understood that, in practice, the measurements can be taken by a single tool (or, less preferably, plural tools in a single logging run, or plural logging runs).

FIGS. 11A and 11B illustrate the homogeneous and isotropic case. From the monopole data of FIG. 11A, it is seen that the compressional slowness from the short T/R measurement (the log 1110) substantially corresponds to the slowness from the long T/R measurement (the log 1120). This is one indication of homogeneity. From the dipole data of FIG. 11B, two things can be observed. First, the curves 1151, 1152 (measured data) are from the crossed dipole acquisition from orthogonal transmitters/receivers. Since the two dispersion curves lie substantially on top of each other, an isotropic formation is indicated. Secondly, the measured data is similar to the modeled dispersion curve (1153). The model curve is for the homogeneous case. The measured data fitting the model is a second indicator that the formation is homogeneous. Thus, with a joint processing of monopole and dipole data, it is determined that the formation at the depth of these measurements is both homogeneous and isotropic.

FIGS. 12A and 12B illustrate the inhomogeneous and isotropic case. From the monopole data, it can be seen that the compressional slowness from the short T/R measurement (the log 1210) does not correspond to the slowness from the long T/R measurement (the log 1220). This is one indication of inhomogeneity, as described above. From the crossed dipole data of FIG. 12B, it can be observed that the dispersion curves 1251, 1252 (measured data) lie substantially on top of each other. This indicates that the formation is isotropic. Next, a determination is made as to whether the measured dispersion curves fit the modeled dispersion curve (1253). Since, as seen, the measured data does not fit the model, there is a second indicator that the formation is inhomogeneous. Thus, with a joint processing of monopole and dipole data, it is determined that the formation at the depth of these measurements is inhomogeneous and isotropic.

FIGS. 13A and 13B illustrate the homogeneous and anisotropic case. From the monopole data, it can be seen that the compressional slowness from the short T/R measurement (log 1310) substantially corresponds to the slowness from the long T/R measurement (log 1320). This indicates homogeneity. From the crossed dipole data, it can be observed that the dispersion curves 1351, 1352 (measured data) do not lie on top of each other. There is a characteristic difference in slowness at low frequency. This indicates that the formation is anisotropic. Next, the two measured dispersion curves are nearly parallel, or non-crossing. This indicates that this is an intrinsic anisotropic formation. Next, a determination is made as to whether the measured dispersion curves substantially fit the modeled dispersion curve (1353). Since, as seen, the measured data substantially fits the model, there is a second indicator that the formation is homogeneous. Thus, it is determined that the formation at the depth of these measurements is homogeneous and anisotropic.

FIGS. 14A and 14B illustrate the inhomogeneous and anisotropic case. This is the most general case. From the monopole data, it can be seen that the compressional slowness from the short T/R measurement (log 1410) does not correspond to the slowness from the long T/R measurement (log 1420). This is one indication of inhomogeneity. From the crossed dipole data, it can be observed that the dispersion

curves 1451, 1452 do not lie on top of each other. There is a characteristic difference in slowness at low frequency that indicates that the formation is anisotropic. In addition, the measured dispersion curves do not fit the modeled dispersion curve (1453), another indication of inhomogeneity. Thus, it is determined that the formation at the depth of these measurements is inhomogeneous and anisotropic.

In a form of the present invention, an integrated inversion of monopole, dipole and Stoneley data is performed to select a suitable rock model. After classifying the formation using one of the available rock models, the processing chain subsequently computes answer products appropriate to the selected model. In an embodiment hereof, the first stage in the processing chain is to test all of the recorded sonic data for consistency with four different models of the physics as first set forth above in the Table:

Homogeneous/Isotropic
Homogeneous/Anisotropic
Inhomogeneous/Isotropic
Inhomogeneous/Anisotropic

The assumed models vary in complexity. The homogeneous isotropic model is the simplest model whose physics is well understood i.e., there is a complete theoretical understanding of sound propagation in a homogeneous isotropic formation. The inhomogeneous/isotropic and the homogeneous/anisotropic models are more complex, requiring more physical parameters for their description. For each of these models, there is not as complete an understanding of sound propagation as there is for the homogeneous isotropic case. The inhomogeneous/isotropic model is the most complex model, requiring the most physical parameters for its description, and the least well understood of the four models.

The different proposed rock models have varying complexity, and have the property that the same data might be explained equally well by different models. Sound propagation in the homogeneous/isotropic model can be viewed as a special case of sound propagation in the homogeneous/anisotropic model (or, indeed, the other two models) with certain physical parameters set to special values (e.g. the two shear speeds set to the same value). Thus, simply selecting a model based on finding the model which best fits the data may not always be a good criterion on which to base the classification. Qualitatively, a more complex model, with more degrees of freedom, can always be adjusted to fit the data better than a simpler model.

Differing model complexity also highlights a related problem. The more complex models require more physical parameters for their description, some of which cannot be easily inferred from the data. In some cases, more complex models require extremely complicated inversions, or may be severely underdetermined by the available data. An example is the inhomogeneous isotropic rock model, which is intended to address the case of radial variation of slowness away from the borehole. The inhomogeneous isotropic model is much more complicated than the homogeneous anisotropic model, as it covers a continuum of radial slowness profiles.

In a form hereof, the technique for model selection overcomes the problem of differing model complexity, and the problem of indeterminacy for more complex models. Initially, testing is performed for deviations from the homogeneous, isotropic model. This phase relies only on the complete understanding of the homogeneous isotropic model and does not require a complete theoretical description of the other three models, save that they all subsume the homogeneous isotropic model. In an embodiment hereof, the

criterion used for model selection is based on computing Bayesian posterior probabilities for the four different models. FIG. 15 illustrates the qualitative basis of this procedure. A simple model, with a few parameters, describes a smaller family of possible datasets than a more complex model with more parameters. If the horizontal axis describes the universe of possible datasets, then the simpler Model 1 in FIG. 15 describes a smaller subset of datasets compared with the more complex Model 2. Notice that there can be an overlap; that is, certain sets of data can be described by both Models 1 and 2. If one assumes a priori uniform probability density distributions are imposed for datasets described by both models, then it follows that on the region of overlap, the simpler Model 1 is, a priori, the more probable one.

This forms the basis of the model selection procedure of the present embodiment. The data is tested for goodness of fit between a simpler model and a more complex model, which subsumes the simple model. The more complex model is selected not simply if it fits the data better than the simple model; it is only selected if the goodness of fit is sufficiently better to warrant using the added complexity of the more complex model. In this embodiment, two specific statistical tests are applied to select one of the four models. First, there is a test for homogeneity versus inhomogeneity, such as the above-described type of testing for radial variations of velocity, which can be applied to both monopole and dipole data. Second there is a test for isotropy versus anisotropy, such as described above, applied only to dipole data.

As above, the test for inhomogeneity on monopole data comprises a test for differences in monopole compressional slowness near and far from the borehole. Measured transit times, or differential transit times, are tested for deviations from a linear trend (predicted by a homogeneous isotropic model). Also as above, the test for inhomogeneity on dipole data comprises a test for deviation of a measured flexural dispersion curve from a library of known flexural dispersion curves belonging to the homogeneous isotropic model (see e.g. FIG. 10). The measured flexural dispersion curve can be the output of a known dispersion analysis algorithm (see, for example, Ekstrom, M. P., 1995, Dispersion Estimation From Borehole Acoustic Arrays Using A Modified Matrix Pencil Algorithm: 29th Asilomar Conf. Signals Sys. and Compt., Pacific Grove, Calif., October 31). The measured flexural dispersion with error bars is tested for whether it belongs to the known family of curves corresponding to the homogeneous isotropic model, or not.

Following the test for inhomogeneity versus homogeneity, a test is performed for isotropy versus anisotropy. In the present embodiment, and as described in the examples above, this test is only performed on dipole data. The test can be a statistically based test for the presence of one flexural shear (isotropic) versus two flexural shear waves (anisotropic). This can be implemented using comparison of a simple model (one wave present) versus a more complex model (two waves present), and selection of the model using a likelihood factor, as illustrated in FIG. 16, which shows an example in which model order 2 indicates that the estimate of two dispersion curves fits the data best; i.e., has the largest "evidence". An alternative is to use cross-line energy as a test statistic and employ a threshold to decide between anisotropy and isotropy; a technique that is already used as a qualitative indicator of anisotropy. In addition, if Stoneley wave slowness data is available, that information can be incorporated as a constraint on the shear slowness.

FIG. 17 is a flow diagram that represents the processing chain, and which can be used in programming a suitable

processor, such as the processor 270 of the surface equipment of FIG. 1 or a remote processor, in practicing an embodiment hereof. The block 1710 represents the collection of the data signals. A downhole processor could also perform at least part of the technique. The data may, for example, be collected and stored using the logging apparatus described in conjunction with FIGS. 1-4, although it will be understood that other suitable equipment can be utilized. The data in the present embodiment includes both monopole and dipole broadband measurements.

The block 1715 represents the generating of the logs (e.g. in FIGS. 7, 11A, 12A, 13A and 14A) and the actual and model dispersion curves (e.g. in FIGS. 8-10, 11B, 12B, 13B and 14B) from the collected measurement data. The block 1720 represents determination of the monopole slowness difference for the relevant depth range, for example, the slowness difference of FIGS. 11A, 12A, 13A or 14A. The block 1730 represents performance of classification of the dispersion curves as was explained in conjunction with FIGS. 11B, 12B, 13B and 14B, and which can utilize, for example, the type of technique described in conjunction with FIG. 16. The decision block 1740 represents the determination of whether the formation is homogeneous. In the present embodiment, the prior determination of block 1720 is utilized, together with a predetermined threshold, to make a determination of homogeneity/inhomogeneity, for example by determining whether the difference in slowness (as between the relatively short and relatively long T/R spacing measurements of slowness), and deeming the formation homogeneous if the difference does not exceed the predetermined threshold. It will be understood, however, that the degree of inhomogeneity, which will be related to the magnitude of the stated difference, can also be output. [Also, as noted above, a dipole dispersion versus model can also be used as an inhomogeneity indicator.] Determination is then made (decision block 1750, shown as two separate blocks, 1750A and 1750B in the diagram of FIG. 17) is then entered for a determination of whether the formation is isotropic or anisotropic. In the present embodiment, this determination can depend on the previously performed classification of dispersion curves (block 1730) using, for example, the rules described in conjunction with the examples of FIGS. 11B, 12B, 13B, and 14B. It will be understood that the degree of anisotropy can also be quantified, based, for example, on the extent of separation of the dispersion curves. As seen in FIG. 17, depending on the outputs of decision blocks 1750A and 1750B, the characterization of the formation is made as one of: homogeneous/isotropic, homogeneous/anisotropic, inhomogeneous/isotropic, or inhomogeneous/anisotropic. These characterizations can be read out, and the next depth level of interest processed in similar manner.

In accordance with an embodiment of the invention, detection of inhomogeneity (e.g. detection of alteration around the borehole resulting from fluid invasion or from stress concentration around the wellbore) includes determination of changes in the measured slowness as the transmitter-to-receiver (TR) spacing is varied. An existing model would naturally predict, for a ramp-shaped velocity profile, a decrease in measured slowness as the TR spacing is increased. However, Applicant has noted that a problem with using transit time estimates to detect changes in slowness is complicated by the presence of borehole and formation effects as well as gross errors that can occur in transit time estimates as a result, for example, of cycle skips. A feature hereof is the robust determination of alteration around the borehole, even in the presence of these complicating effects.

In an embodiment of the invention, the problem of detecting radial alteration (a radial decrease of slowness) in the near wellbore region is recast as a problem of detecting a variation in measured slowness at different TR spacings. It can be noted that the approach of this embodiment applies only to the case where the slowness decreases with increasing radius; that is, away from the borehole.

Consider first an idealized case, with a perfect borehole and with no lateral variations in slowness in the formations. FIG. 18 shows a linear radial profile of velocity around the borehole. In this example the velocity at the borehole wall ($r=0.35$ ft) is about 9000 ft/sec and the velocity in the virgin formation (starting at $r=1.5$ ft) is about 10,000 ft/sec, with the velocity increasing linearly in the alteration region.

FIG. 19 illustrates (solid line curve 1910) the variation of transit time (TT) with TR spacing for the linear radial profile of FIG. 18. (The corresponding curves, actually straight lines, shown in dashed line, for homogeneous profiles with borehole wall velocity (1920) and virgin formation (1930) are presented for comparison.) As seen, the curve 1910 deviates from linear moveout with TR spacing. This is readily observed in FIG. 20, which shows the differential transit time (DTT) as a function of TR spacing for $\frac{1}{2}$ ft. spacings. The derivative of the transit time with respect to TR spacing or measured slowness shows a monotonic decline until about TR_c, which, in both FIGS. 19 and 20, is the minimum TR spacing at which modeled sonic energy rays penetrate the virgin formation.

In actuality, the TR spacing is not continuously varied, but rather is available for certain discrete values which depend on the transmitter and receiver placements on the logging tool. Therefore, as in FIG. 20, differential transit time, derived from differences between transit times for adjacent receivers for a given transmitter, can be plotted against the average TR spacing of the receivers ($\frac{1}{2}$ ft., in this example). It can be noted that the differential transit time exhibits a clear signature of a monotonically decreasing trend leveling out to a constant value which is the virgin slowness. This provides a basis for devising a detector for radial alteration.

In the present embodiment, an alteration detector is established to solve a hypothesis testing problem based on the above-described differential transit times. It seeks to decide between the following two hypotheses, H₀, H₁:

H₀: DTT=constant

H₁: DTT-decreasing trend with TR.

In this embodiment there is no assumption of a particular radial slowness profile, only that slowness decreases with increasing radius so as to produce a decreasing trend in measured slowness with TR spacing. The detected signals include measurement errors, and a noise component is included in the model.

To a first order, a decreasing trend can be fitted by a line with a negative slope. For this case, the above hypotheses can be cast as follows:

H₀: DTT=s+N

H₁: DTT=mTR+c+N, m<0

Where s, c are constants, m is the slope, and N is the measurement error (noise).

Although the foregoing does not necessarily precisely fit the actual DTT relationship in an alteration, it does capture the behavior to first order and is relatively easy to solve for a test statistic.

The Generalized Likelihood Ratio Test (GLRT) for the above problem with independent identically distributed (i.i.d.) normal errors yields the following test statistic, T₁:

$$T_1 = \frac{\sum_i (DTT_i - \bar{DTT})^2}{\min_{m \in \mathcal{L}_0} \sum_i (DTT_i - mTR_i - c)^2} \quad (1)$$

5

If the errors are not i.i.d., the above statistic can be modified by suitably incorporating the covariance matrix of the errors as weighting coefficients in the terms of the sums, i.e.,

$$T_1 = \frac{\sum_i W_i (DTT_i - \bar{DTT})^2}{\min_{m \in \mathcal{L}_0} \sum_i W_i (DTT_i - mTR_i - c)^2} \quad (1A)$$

Where $W = R^{-1}$ is the inverse of the covariance matrix R , W_{ii} being the weighting coefficients on the diagonal of W .

The test consists of comparing the statistic to a threshold τ which is chosen based on a desired level of false alarms (detection of altered zone where there is none) and choosing H_0 when the threshold is exceeded. This can be written as

$$T_1 > \tau \text{ which is interpreted as } T_1 < \tau \Rightarrow H_0, T_1 > \tau \Rightarrow H_1 \quad (2)$$

In a further form of the present embodiment of the invention, the test statistic can be refined further by noting that the next order fit, especially when there are constant regions in the DTT curve, is a piecewise fit with a monotonic decreasing trend in the smaller TR spacings and with a constant for the longer TR spacings, such that the whole function is monotonic decreasing. This yields the following test statistic

$$T_1 = \frac{\sum_i (DTT_i - \bar{DTT})^2}{\min_{R_c, c_1, m \in \mathcal{L}_0, mR_c = \tau_1} \sum_i (DTT_i - p_{R_c, m, c_1, \tau_1}(TR_i))^2} \quad (3)$$

where

$$p_{R_c, m, c_1, \tau_1}(x) = \begin{cases} mx + c_1, & x < R_c \\ c_2, & x \geq R_c \end{cases} \quad (4)$$

In practice, R_c is chosen to fall in the middle third of the range of TR spacings so as to have enough points for statistical stability. FIG. 21 illustrates the way the straight line and the piecewise straight line are fitted to the data (the star points representing simulated data, including noise) while obtaining T_1 and T_2 . The Figure shows best fit outcomes for T_1 (curve 2110) and T_2 (curve 2120). The expected error free measurement is shown at curve 2130.

Since there are two test statistics T_1 and T_2 , each of which is appropriate in a particular scenario, they can be combined, and the problem can be expressed as that of choosing between three hypotheses:

H0: DTT—constant

H1: DTT—decreasing linear trend with TR

H2: DTT—decreasing piecewise linear and constant trend.

This problem can be solved using the GLRT approach by introducing two threshold numbers τ_0 and τ_{12} and implementing

$$\max = (T_1 < \tau_{12}, T_2 < \tau_0, \frac{\tau_1}{\tau_0} < \frac{T_2}{T_1} < \frac{\tau_{12}}{\tau_{11}}) \quad (5)$$

Numerical simulations using the present embodiment have shown that the performance of the more complex detector based on both T_1 and T_2 for detecting alteration may not be significantly superior to that based on T_1 alone. Accordingly, a variation of the present embodiment uses T_1 alone to detect alteration and uses the ratio of T_2 to T_1 to detect the virgin zone.

The threshold numbers τ_0 and τ_{12} are preferably chosen to control the probability of false alarm (detecting alteration where none is present) and misclassification (finding a leveling out when the actual trend is a continuous decrease). Thus, it is advantageous to know the distributions of these test statistics. It is possible to characterize the distribution of the test statistic T_1 under H_0 with Gaussian errors. It can be shown to have a distribution which is a $(\frac{1}{2}, \frac{1}{2})$ mixture of a point mass at 1 and a shifted F-distribution. This does not depend on the variance of the error and therefore allows a pre-computation of the threshold for fixing the false alarm rate. The distribution of the test statistic T_2 is more complex and, at present, can be selected on the basis of tests and heuristics.

It is seen from equation (2) that the best fit for the T_2 statistic incorporates a constant fit at long TR spacings. This provides an estimate of the virgin slowness when the test for virgin zone picks H12. Referring to FIG. 22, there is shown a flow diagram of a routine for determination of alteration detection that can be used, inter alia, as an input to homogeneity determination (e.g. blocks 1720 and 1740) of FIG. 17. As above, the block 1710 represents collection of the logging data. In the present embodiment, compressional transit time measurements are derived from several different TR spacings. As above noted, such as in conjunction with FIG. 4, the data is digitized and processed (block 2215). As represented by the block 2225 blocks of data are subjected to gross error filtering, which removes data points that are grossly inconsistent with neighboring data. Wavelet scale filtering can then be implemented, as represented by the block 2235. Depth alignment, from measurements at different spacings, can then be performed, as represented by the block 2250, and DTT versus TR is obtained (e.g. in the graph of FIG. 19). The constants s and c are selected and the negative slope m is initialized, as represented by the block 2260. Also, the threshold τ , τ_0 , and τ_{12} are selected (block 2265). Then, as represented by the block 2275, the test statistics T_1 and/or T_2 can then be computed, in accordance with equations (1), (1A), and (3), and the hypotheses from among H0, H1 and/or H11, and H12 can be chosen in accordance with the threshold determinations (2) and/or (5). This can be used to provide a general and/or specific (e.g. from the quantified test statistics, which can also be produced using modified constants and slopes, as indicated) indications of alteration, as an inhomogeneity indicator. Also, as seen from equation (2), the best fit for the test statistic T_2 incorporates a constant fit at long TR spacings. This provides an estimate of the virgin slowness when the test for the virgin zone selects hypothesis H12. Thus, for instance, in the example of FIG. 21, the piecewise fit has a constant slowness (as a function of TR spacing) in the virgin zone of about 101 usec/ft.

The foregoing technique is illustrated in terms of compressional waves, but can be applicable to other sonic waves, an example being shear headwaves in a fast formation.

What is claimed is:

1. A method for determining alteration of a region of an earth formation surrounding an earth borehole, comprising the steps of:

providing a logging device that is moveable through the borehole;

transmitting sonic energy into the formation and receiving, at a plurality of transmitter-to-receiver spacings on said logging device, sonic energy that has traveled through the formation, and producing signals representative of the received sonic energy for said plurality of transmitter-to-receiver spacings;

determining, from said signals, sonic transit times and differential transit times for the respective transmitter-to-receiver spacings;

deriving a test statistic from said differential transit times; and

determining the presence of alteration of a region of the formations from said test statistic.

2. The method as defined by claim 1, wherein said determined sonic transit times and differential transit times are sonic compressional transit times and sonic compressional differential transit times.

3. The method as defined by claim 1, wherein said step of determining the presence of alteration of a region of the formations from said test statistic comprises comparing said test statistic to a threshold.

4. The method as defined by claim 2, wherein said step of determining the presence of alteration of a region of the formations from said test statistic comprises comparing said test statistic to a threshold.

5. The method as defined by claim 1, wherein said test statistic includes a component that depends on the degree to which the differential transit times decrease monotonically as a function of transmitter-to-receiver spacing.

6. The method as defined by claim 2, wherein said test statistic includes a component that depends on the degree to which the differential transit times decrease monotonically as a function of transmitter-to-receiver spacing.

7. The method as defined by claim 2, wherein said test statistic includes a component that depends on the degree to which the differential transit times, as a function of transmitter-to-receiver spacing, corresponds to a line of negative slope.

8. The method as defined by claim 2, wherein said test statistic includes components that depend on the degree to which the differential transit times, as a function of transmitter-to-receiver spacing, corresponds to a line of negative slope followed by a line of substantially zero slope.

9. The method as defined by claim 2, further comprising determining the compressional slowness of the virgin earth formation from said test statistic.

10. The method as defined by claim 8, further comprising determining the compressional slowness of the virgin earth formation from said test statistic.

11. The method as defined by claim 1, wherein said test statistic T_1 is of the form

$$T_1 = \frac{\sum_i (DTT_i - DTT)^2}{\min_{m,c} \sum_i (DTT_i - mTR_i - c)^2}$$

where DTT_i are the individual differential transit times,

DTT is the average of the differential transit times, TR_i are the individual transmitter-to-receiver spacings, and m and c are constants.

12. The method as defined by claim 2, wherein said test statistic T_1 is of the form

$$T_1 = \frac{\sum_i (DTT_i - DTT)^2}{\min_{m,c} \sum_i (DTT_i - mTR_i - c)^2}$$

where DTT_i are the individual differential transit times.

DTT is the average of the differential transit times, TR_i are the individual transmitter-to-receiver spacings, and m and c are constants.

13. The method as defined by claim 2, wherein said test statistic T_1 is of the form

$$T_1 = \frac{\sum_i W_{ii} (DTT_i - DTT)^2}{\min_{m,c} \sum_i W_{ii} (DTT_i - mTR_i - c)^2}$$

where DTT_i are the individual differential transit times,

DTT is the average of the differential transit times, TR_i are the individual transmitter-to-receiver spacings, m and c are constants, and W_{ii} are weighing coefficients on the diagonal of the inverse of the covariance matrix.

14. The method as defined by claim 2, wherein said test statistic T_1 is of the form

$$T_1 = \frac{\sum_i (DTT_i - DTT)^2}{\min_{R_c, m, c_1, c_0} \sum_i (DTT_i - p_{R_c, m, c_0, c_1}(TR_i))^2}$$

where

$$p_{R_c, m, c_0, c_1}(x) = \begin{cases} mx + c_1, & x < R_c \\ c_0, & x \geq R_c \end{cases}$$

where DTT_i are the individual differential transit times,

DTT is the average of the differential transit times, TR_i are the individual transmitter-to-receiver spacings, and m , c_0 , c_1 , and R_c are constants.

15. Apparatus for determining alteration of a region of an earth formation surrounding an earth borehole, comprising:

a logging device that is moveable through the borehole; means on said logging device for transmitting sonic energy into the formation and receiving, at a plurality of transmitter-to-receiver spacings on said logging device, sonic energy that has traveled through the formation, and for producing signals representative of the received sonic energy for said plurality of transmitter-to-receiver spacings;

means for determining, from said signals, sonic transit times and differential transit times for the respective transmitter-to-receiver spacings;

means for deriving a test statistic from said differential transit times; and

means for determining the presence of alteration of a region of the formations from said test statistic.

16. Apparatus as defined by claim 15, wherein said means for determining the presence of alteration of a region of the formations from said test statistic comprises means for comparing said test statistic to a threshold.

17. A method for determining alteration of a region of the earth formation, for use in conjunction with a technique for sonic logging of an earth formation that includes: providing

a logging device that is moveable through the borehole; transmitting sonic energy into the formation and receiving, at a plurality of transmitter-to-receiver spacings, sonic energy that has traveled through the formation, and producing signals representative of the received sonic energy for said plurality of transmitter-to-receiver spacings, comprising the steps of:

- determining, from said signals, sonic transit times and differential transit times for the respective transmitter-to-receiver spacings,
- deriving a test statistic from said differential transit times;
- and
- determining the presence of alteration of a region of the formations from said test statistic.

18. The method as defined by claim 17, wherein said determined sonic transit times and differential transit times are sonic compressional transit times and sonic compressional differential transit times.

19. The method as defined by claim 17, wherein said step of determining the presence of alteration of a region of the formations from said test statistic comprises comparing said test statistic to a threshold.

20. The method as defined by claim 17, wherein said test statistic includes a component that depends on the degree to which the differential transit times decrease monotonically as a function of transmitter-to-receiver spacing.

21. The method as defined by claim 17, wherein said test statistic includes a component that depends on the degree to which the differential transit times, as a function of transmitter-to-receiver spacing, corresponds to a line of negative slope.

22. The method as defined by claim 17, wherein said test statistic includes components that depend on the degree to which the differential transit times, as a function of transmitter-to-receiver spacing, corresponds to a line of negative slope followed by a line of substantially zero slope.

23. The method as defined by claim 18, further comprising determining the compressional slowness of the virgin earth formation from said test statistic.

24. The method as defined by claim 17, wherein said test statistic T_2 is of the form

$$T_2 = \frac{\sum_i (DTT_i - DTT)^2}{\min_{m,c} \sum_i (DTT_i - mTR_i - c)^2}$$

where DTT_i are the individual differential transit times, DTT is the average of the differential transit times, TR_i are the individual transmitter-to-receiver spacings, and m and c are constants.

25. The method as defined by claim 17, wherein said test statistic T_3 is of the form

$$T_3 = \frac{\sum_i W_{ii}(DTT_i - DTT)^2}{\min_{m,c} \sum_i W_{ii}(DTT_i - mTR_i - c)^2}$$

where DTT_i are the individual differential transit times, DTT is the average of the differential transit times, TR_i are the individual transmitter-to-receiver spacings, m and c are constants, and W_{ii} are weighing coefficients on the diagonal of the inverse of the covariance matrix.

26. The method as defined by claim 17, wherein said test statistic T_4 is of the form

$$T_4 = \frac{\sum_i (DTT_i - DTT)^2}{\min_{R_e, c_0, c_1} \sum_i (DTT_i - p_{R_e, mC_0, C_1}(TR_i))^2}$$

where

$$p_{R_e, mC_0, C_1}(x) = \begin{cases} mx + c_1, & x < R_e \\ c_0, & x \geq R_e \end{cases}$$

where DTT_i are the individual differential transit times, DTT is the average of the differential transit times, TR_i are the individual transmitter-to-receiver spacings, and m , c_0 , c_1 , and R_e are constants.

27. A method for determining whether a region of an earth formation surrounding an earth borehole is homogeneous, comprising the steps of:

- providing a logging device that is moveable through the borehole;

transmitting sonic energy into the formation and receiving, at a plurality of transmitter-to-receiver spacings on said logging device, sonic energy that has traveled through the formation, and producing signals representative of the received sonic energy for said plurality of transmitter-to-receiver spacings;

determining, from said signals, sonic transit times and differential transit times for the respective transmitter-to-receiver spacings;

deriving a test statistic from said differential transit times; and

determining, from said test statistic, whether said region of the formation is homogeneous.

28. The method as defined by claim 27, wherein said determined sonic transit times and differential transit times are sonic compressional transit times and sonic compressional differential transit times.

29. The method as defined by claim 27, wherein said step of determining, from said test statistic, whether said region of the formation is homogeneous, comprises comparing said test statistic to a threshold.

30. The method as defined by claim 27, wherein said test statistic includes a component that depends on the degree to which the differential transit times decrease monotonically as a function of transmitter-to-receiver spacing.

31. The method as defined by claim 27, wherein said test statistic includes a component that depends on the degree to which the differential transit times, as a function of transmitter-to-receiver spacing, corresponds to a line of negative slope followed by a line of substantially zero slope.

32. The method as defined by claim 27, wherein said test statistic includes components that depend on the degree to which the differential transit times, as a function of transmitter-to-receiver spacing, corresponds to a line of negative slope followed by a line of substantially zero slope.

33. The method as defined by claim 27, wherein said test statistic T_1 is of the form

$$T_1 = \frac{\sum_i (DTT_i - DTT)^2}{\min_{m,c} \sum_i (DTT_i - mTR_i - c)^2}$$

where DTT_i are the individual differential transit times, DTT is the average of the differential transit times, TR_i are the individual transmitter-to-receiver spacings, and m and c are constants.

34. The method as defined by claim 27, wherein said test statistic T_3 is of the form

$$T_3 = \frac{\sum_i W_{ii} (DTT_i - \bar{DTT})^2}{\min_{m \in \mathbb{Z}} \sum_i W_{ii} (DTT_i - mTR_i - c)^2} \quad 5$$

where DTT_i are the individual differential transit times, \bar{DTT} is the average of the differential transit times, TR_i are the individual transmitter-to-receiver spacings, m and c are constants, and W_{ii} are weighing coefficients on the diagonal of the inverse of the covariance matrix. ₁₀

35. The method as defined by claim 27, wherein said test statistic T_1 is of the form

$$T_1 = \frac{\sum_i (DTT_i - \bar{DTT})^2}{\min_{R_c, c_1, m \in \mathbb{Z}, 0 < mR_c < mR_c + c_1} \sum_i (DTT_i - p_{R_c, mC_0, c_1}(TR_i))^2}$$

where

$$p_{R_c, mC_0, c_1}(x) = \begin{cases} mx + c_1, & x < R_c \\ c_0, & x \geq R_c \end{cases}$$

where DTT_i are the individual differential transit times, \bar{DTT} is the average of the differential transit times, TR_i are the individual transmitter-to-receiver spacings, and m , c_0 , c_1 , and R_c are constants. ₁₅

* * * *